Spectral measurements of runaway electrons in the TEXTOR tokamak

Inaugural-Dissertation

zur

Erlangung des Doktorgrades der

Mathematisch-Naturwissenschaftlichen Fakultät

der Heinrich-Heine-Universität Düsseldorf

vorgelegt von

Timur Kudyakov

aus Bischkek (Kg)

Mai 2009

Aus dem Institut für Laser- und Plasmaphysik
der Heinrich-Heine-Universität Düsseldorf

Gedruckt mit Genehmigung der
Mathematisch-Naturwissenschaftlichen Fakultät der
Heinrich-Heine-Universitt Düsseldorf.

Referent: Prof. Dr. O. Willi
Koreferent: Prof. Dr. U. Samm

Tag der mündlichen Prüfung: 22. 07. 2009

Zusammenfassung

Während der Plasmadisruption innerhalb eines Tokamaks werden hochenergetische Elektronen im Bereich von mehreren MeV, sog. "Runaways", emittiert. Für den Betrieb des zukünftigen Tokamaks ITER spielen Runaway-Elektronen eine entscheidende Rolle, da sie die Betriebsdauer wesentlich reduzieren können.

In dieser Arbeit wurden die zu Grunde liegenden physikalischen Effekte der Entstehung und dem Transport der Runaway-Elektronen am Tokamak TEXTOR des Forschungszentrums Jülich untersucht und eine Abschätzung der Folgen auf den Betrieb von ITER gemacht. Eine hierfür speziell entwickelte Sonde erlaubt, die vom Plasma emittierte Anzahl an Runaway-Elektronen, ihre Energieverteilung und die hervorgerufene Energiedeposition im Material zu messen. Ihre Funktionsweise basiert auf dem Einsatz von YSO Kristallen, welche durch die Elektronen im sichtbaren Spektralbereich szintillierenden. Das Licht wird mit Hilfe von Lichtwellenleitern auf Photovervielfacher geleitet und zeitaufgelöst registriert. Eine Energieauflösung wird dadurch erreicht, dass einzelne Kristalle in Schichten aus Edelstahl unterschiedlicher Dicke eingebettet sind. Mit Hilfe von neun Kristallen konnte ein Energieintervall zwischen 4 MeV und 30 MeV aufgelöst werden. Die Sonde wurde am Elektronen-Linearbeschleuniger ELBE am Forschungszentrum Dresden-Rossendorf absolut kalibriert; die Ergebnisse stimmen gut mit numerischen Monte-Carlo Simulationen mit dem Code Geant4 überein.

Im TEXTOR-Experiment wurde der Transport der Runaway-Elektronen in Anwesenheit externer oder intrinsischer Magnetfelder studiert. Es wurde gefunden, dass der Anstieg der Runaway-Verluste bei abnehmendem Magnetfeld mit einer Erhöhung der magnetischen Fluktuationen verbunden ist. Diese Messung ist neuartig und konnte bisher nicht mit anderen Meßmethoden gefunden werden.

Beim Anlegen eines externen magnetischen Störfeldes durch den Dynamischen Ergodische Divertor (DED) an TEXTOR wurde auch hier die unterschiedliche Abhängigkeit des Transportes als Funktion der Runaway - Energie gefunden. Auch hier ist der Transport der niederenergetischen Runaways höher als derjenige der hochenergetischen. Der verstärkte Verlust der niederenergetischen Elektronen macht sich bei den hochenergetischen mit einer zeitlichen Verzögerung bemerkbar.

Es wurden erstmals Messungen mit der Sonde bei Disruptionen durchgeführt, um den Runaway-Fluss, die Energieverteilung der Runaways als Funktion der Zeit und die Wärmelast zu bestimmen. Die Sonde zeigte einen zeitlich strukturierten Runaway-Verlust. Zuerst - im sog. thermal quench - gehen Runaways verloren, die in der Startphase der Entladung entstanden sind. Danach - in der sog. current quench Phase - beobachtet man Runaway-Elektronen, die in der Phase beschleunigt werden, in denen die magnetische Energie des Tokamaks dissipiert wird. Die gewonnenen Daten erlauben eine Abschätzung der thermischen Effekte im Rahmen des ITER-Konzepts.

Abstract

The generation of multi-MeV runaway electrons is a well known effect related to the plasma disruptions in tokamaks. The runaway electrons can substantially reduce the lifetime of the future tokamak ITER.

In this thesis physical properties of runaway electrons and their possible negative effects on ITER have been studied in the TEXTOR tokamak. A new diagnostic, a scanning probe, has been developed to provide direct measurements of the absolute number of runaway electrons coming from the plasma, its energy distribution and the related energy load in the material during low density (runaway) discharges and during disruptions. The basic elements of the probe are YSO crystals which transform the energy of runaway electrons into visible light which is guided via optical fibres to photomultipliers. In order to obtain the energy distribution of runaways, the crystals are covered with layers of stainless steel (or tungsten in two earlier test versions) of different thicknesses. The final probe design has 9 crystals and can temporally and spectrally resolve electrons with energies between 4 MeV and 30 MeV. The probe is tested and absolutely calibrated at the linear electron accelerator ELBE in Rossendorf. The measurements are in good agreement with Monte Carlo simulations using the Geant4 code.

The runaway transport in the presence of the internal and externally applied magnetic perturbations has been studied. The diffusion coefficient and the value of the magnetic fluctuation for runaways were derived as a function of B_t. It was found that an increase of runaway losses from the plasma with the decreasing toroidal magnetic field is accompanied with a growth of the magnetic fluctuation in the plasma. The magnetic shielding picture could be confirmed which predicts that the runaway loss occurs predominantly for low energy runaways (few MeV) and considerably less for the high energy ones.

In the case of the externally applied magnetic perturbations by means of the dynamic ergodic divertor (DED) runaway electrons with different energies demonstrate a different sensitivity to the DED. Again, highly relativistic electrons are less sensitive to the stochastic magnetic field than the low energy ones.

Measurements of runaway electrons during the plasma disruptions have been carried out by the new probe. The probe has shown two distinct losses of runaways during the thermal quench (runaways were produced at the start up of the discharge) and during the current quench (runaways were produced due to the dissipation of the magnetic field). Important parameters, such as the runaway flux, the energy distribution, the temporal evolution and the thermal load in materials have been studied. The obtained results allow to estimate the thermal load due to runaway electrons in the ITER tokamak.

Acknowledgments

First of all, I would like to thank my advisor, Prof. Oswald Willi for giving me an opportunity to work on challenging and extremely interesting projects over the past four years. I get very valuable support and advise in all questions during the whole time of my work with him.

With a great pleasure I would like to thank my co-advisor, Dr. Karl Heinz Finken. I am very lucky that Dr. Finken has been my co-adviser. It is very hard to transfer in words that enormous amount of knowledge and experience, which he has transferred to me. I have appreciated his support any time during these four years.

I can only say that it has been a pleasure to work with and learn from such an extraordinary individuals as Prof. Willi and Dr. Finken.

A lot of thanks to Dr. Marcin Jakubowski, Dr. Yuhong Xu and Herr Albert Hiller. During the past four years they have done everything to make the work extremely interesting and very successful.

These work would not have been possible without the TEXTOR team and personal support of Prof. Ulrich Samm. I would also like to thank Prof. Samm that he agreed to referee my Ph.D thesis.

My colleagues at the institute have enriched my graduate life in many ways and deserve a special thanks, especially Mirela Cerchez, Toma Toncian, Ralph Jung, Jens Osterholz, Munib Amin, Ariane Pipahl, Thomas Königstein and Bernhard Hidding. I would like to thank Renate ter Horst, Claudia Dingle, Christiane Braun and Katherina Vogt without their efforts the organization of my work would have been impossible. My "scientific baby" would never have been born without the help of Manfred Rosemann, Werner Sigosch, Andreas Karmann, Christoph Bolten and Helmut Borrmann.

I would also like to acknowledge TEXTOR colleagues Dr. Sergey Bozhenkov, Dr. Michael Lehnen, Dr. Wolfgang Biel, Dr. Bernd Schweer who have collaborated with me on the interesting experiments and help me a lot.

A great thanks to colleagues in Forschungszentrum Dresden − Rossendorf Axel Jochmann, Karl Zeil, Dr. Stephan Kraft, Dr. Ulrich Schramm during a few days and nights we can breathe new opportunities in my probe.

A lot of ideas are based on discussions with colleagues from the theoretical groups, in particular Dr. Tünde Fülöp and Dr. Sadrilla Abdullaev.

I owe my deepest thanks to my family - my wife, my parents, my sister and all my best friends, for their support, encouragement and understanding. A lot of thanks to my small daughter, she withstands courageously that her daddy was busy all the time and did not play enough with her.:)

I would like to acknowledge financial support by the DFG programme GRK1203 and F and E contract from FZ Jülich.

It is impossible to remember all, and I apologize to those I've inadvertently left out.

Thank you!

Contents

Chapter 1

Introduction

1.1 Nuclear fusion

The fast growing energy requirement is one of the greatest problems in the world. Simulations show that the energy consumption in 2050 will be three times higher than these days and are going to reach 10^{21} J per year [99]. The existing energy sources such as coal, oil and gas are very limited on the Earth and cannot satisfy the requirements of people. Moreover the environmental pollution and irreversible influence on the climate are becoming a problem as well.

The alternative and perhaps the sole energy source are nuclear reactions. The energy can be produced due to heavy nuclear fission reactions or light nuclear fusion reactions. At present time the nuclear energy production is based only on fission reactions. The nuclear fusion is so far only the subject of research.

The small difference in spelling between "fusion" and "fission" hides by itself the energy future for people in the world. The main and fundamental difference between the energy production by the nuclear fusion and nuclear fission is the absence of long-living radioactive waste, which is typical for nuclear fission reactions. In contrast to the fission reactor, radioactive wastes of which demand the processing and storing for a few thousands years, the preserved fusion reactors will require only 100 years. Besides low radioactivity, the fusion

power plant has enormous fuel inventory, which will be sufficient to produce energy during thousands of years.

The most promising reaction, is the one between the two hydrogen isotopes deuterium $D \equiv H_1^2$ and tritium $T \equiv H_1^3$:

$$\mathbf{D + T \rightarrow He_2^4\ (3.5\ MeV) + n\ (14.1\ MeV)}, \tag{1.1}$$

where He stands for helium and n is an energetic neutron. Tritium can be obtained using the second reaction:

$$\mathbf{Li^6 + n \rightarrow T + He^4}. \tag{1.2}$$

Lithium Li_3^6 by estimation is present commercially in sea water or can be mined. In contrast to nuclear fission reactions, the fusion reaction does not produce long-living radioactive debris of heavy nucleus. The only unstable element in these reactions is tritium. Tritium is a radioactive hydrogen isotope with a half-life of about 12.3 years. As a consequence of β-decay it turns into He^3, radiating low energy electrons. The low level of nuclear waste, plentiful supplies of radioactive fuel give the potential possibility to create a "clean" reactor. Wall materials become radioactive by the neutrons. However one has the choice to use elements with short lifetimes.

1.2 Tokamak

The main barrier for nuclear fusion is the Coulomb barrier, as the two positive charges have to overcome the Coulomb force. In the case of DT-reactions, ions should have a minimum energy 10 keV. At such high temperature any matter becomes fully ionized, 10 keV corresponds to a temperature of about 10^8 K. For intense to proceed the fusion reaction it is necessary to fulfil the following condition:

$$\mathbf{n\tau \geq 10^{14} cm^{-3} s}, \tag{1.3}$$

where n is plasma density in cm^{-3}, τ is confinement time of plasma energy in s. This is known as the Lawson criterion [61, 100]. For the most probable DT-reaction at temperature 10^8 K, the plasma density should be not less than $10^{14} cm^{-3}$. Confinement time in this case should be about 1 s.

The idea of magnetic thermo-isolation of the hot plasma to avoid a contact with the vessel wall was independently proposed by Sakharov, Tamm and Spitzer. The main idea was that the magnetic field should confine a transverse plasma spreading out from the reaction region. Due to the Lorenz force the charged particle should wind around magnetic field lines, with a Larmor radius $r \sim V_\perp/B$, where $V_\perp$ - is the transverse particle velocity and B is the magnetic field. Along the magnetic field lines particles cannot be confined. Therefore the magnetic flux tube is formed to a torus. The toroidal magnetic field is non-uniform, and in a non-uniform magnetic field charged particles undergo a systematic drift, as a result toroidal magnetic field alone cannot provide full and long thermal insulation. There were two solutions to solve this problem one was proposed by Spitzer. Toroidal drift of particles is compensated by external helical magnetic fields. This principle was realised in a stellarator. Another idea was proposed by Sakharov and Tamm. They suggested to close particles drift by generating an additional current along the plasma ring. This idea was realized in tokamak systems (derived from the Russian 'toroidalnaya kamera i magnitnaya katushka', which means toroidal chamber with magnetic coils). In 1969 in Dubna (USSR) the superiority of the tokamak system on stellarator was demonstrated. The tokamak scheme is shown in Fig. 1.1. In a tokamak the plasma is confined by helical magnetic fields in a toroidal chamber. The main toroidal magnetic field B_t, containing a hot plasma, is induced by external coils. The poloidal field B_p is produced by a plasma current, which runs along the toroidal plasma cord. The current is kept up by circuital electric field, produced by the primary winding of induction coils. Furthermore, in order to maintain the plasma equilibrium, the poloidal windings are used. The electromagnetic forces, produced by currents running in the poloidal windings, affect the plasma current and can change the plasma position in the chamber and the shape of the plasma cord cross section. The main parameters, which define the tokamak system, are:

- **Gyration frequency and Larmor radius**. Charged particles, which have the transverse component of the particle velocity. These particles are affected by the Lorentz force, which is directed in the $\mathbf{v} \times \mathbf{B}$ direction, so the particle can move freely along the magnetic field. For the transverse direction moving particles, the Lorentz force leads to a gyration

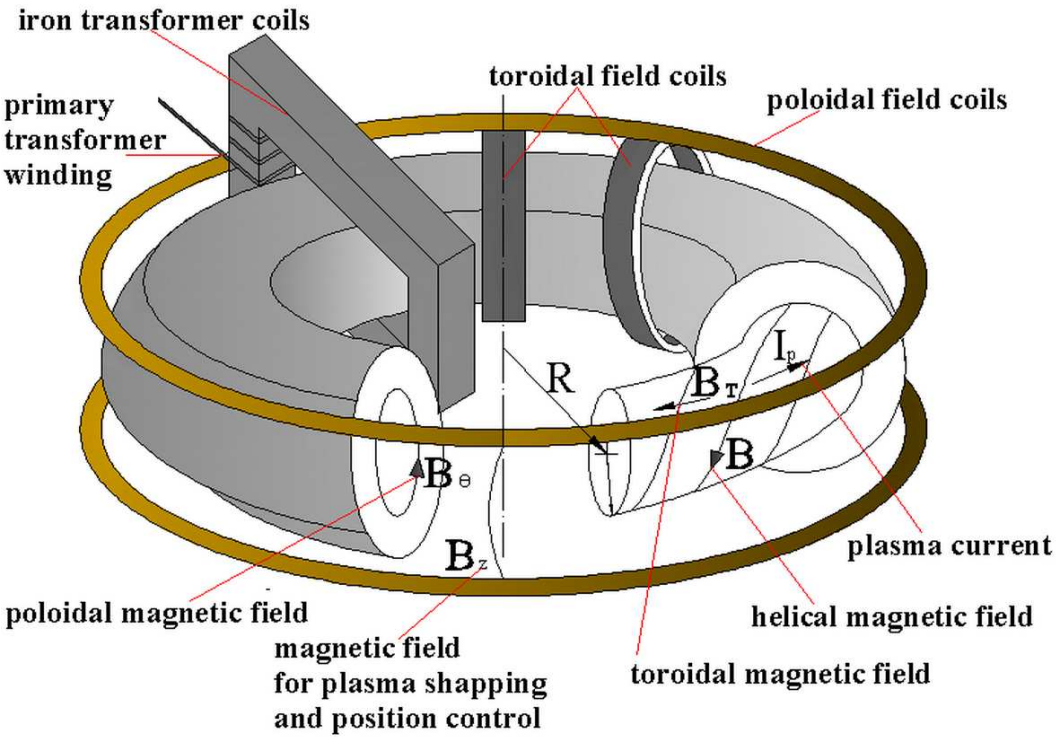

Figure 1.1: Schematic diagram of a tokamak.

motion with a frequency ω_c and a Larmor radius ρ_L:

$$\omega_c = \frac{ZeB}{m}; \qquad \rho_L = \frac{mV_\perp}{ZeB}, \tag{1.4}$$

where e is the electron charge, Z is the charge number of the particle, m its mass and $V_\perp$ the velocity perpendicular to the magnetic field B.

- **β-parameter**. A strong magnetic field is a very convenient tool for confining high-temperature plasmas. From economical points of view, a very important dimensionless value is the ratio of plasma pressure to the magnetic field pressure:

$$\beta = \frac{8\pi p}{B^2}. \tag{1.5}$$

- **Safety factor q**. In order to describe the tokamak's magnetic field, the helicity of the magnetic field, the safety factor parameter is usually used. The safety factor is defined as the number of toroidal turns a field line

must make to complete a full poloidal turn:

$$\mathbf{q_{cyl}} = \frac{\mathbf{rB_T}}{\mathbf{RB_\theta}}, \tag{1.6}$$

where B_T is the toroidal magnetic field, B_p is the poloidal magnetic field, r is the distance to the plasma centre and R is the toroidal radius vector. The equality Eq. (1.6) is valid only for a large aspect ratio, i.e. $r/R \ll 1$, in the simple, cylindrical approximation. The q value can be introduced using another definition which is more convenient in the case of D-shape plasma columns.
The increment of the toroidal magnetic flux for an increase dr in r is $d\Phi = 2\pi r B_T dr$, and for the poloidal magnetic flux is $d\Psi = 2\pi R B_\theta dr$, thus the safety factor can be represented, as:

$$\mathbf{q} = \frac{\mathbf{d\Phi}}{\mathbf{d\Psi}}. \tag{1.7}$$

- **Magnetic surfaces**. The tokamak plasma reaches an equilibrium when the pressure gradient is balanced by the ampere force:

$$\nabla \mathbf{p} = \frac{\mathbf{J} \times \mathbf{B}}{\mathbf{c}} \tag{1.8}$$

or

$$\mathbf{B} \cdot \nabla \mathbf{p} = \mathbf{0} \qquad \mathbf{J} \cdot \nabla \mathbf{p} = \mathbf{0} \tag{1.9}$$

These relations may be considered as a statement that the pressure is constant along the magnetic field and current lines. Field lines with the same helicity lie on closed nested surfaces p = constant, called magnetic or flux surfaces.

- **Shafranov shift**. The toroidal geometry of the tokamak causes the outward shift of the flux surfaces. This radial displacement of magnetic surfaces is called the Shafranov shift.

1.3 Runaway electrons

Electric fields in plasmas can accelerate electrons up to relativistic energies. These electrons are effectively collision-less and the drag force by collisions is smaller than the acceleration by the field. Therefore the group of electrons which fulfils the condition of non-collisionality "runs away" from the thermal part of the distribution function and are called "runaway electrons".

Runaway electrons are observed in astrophysics [49], in lightning [48], and in fusion plasmas which have imposed electric fields [17, 54]. The fusion device with the best confinement properties and which is most investigated is the tokamak, a toroidal device which is characterized by a strong toroidal magnetic field and an axial current. Here runaway electrons have been described already in very early devices; however, runaway discharges never attracted the interest of the mainstream of investigators because the discharges require a low density and show therefore little favourable energy confinement properties. Nevertheless, runaways create damages at plasma facing components such as on metallic limiters. On Tore Supra (Cadarache, France), runaways have even penetrated the graphite shielding of an actively cooled limiter which led to a fracture of the cooling tube such that the cooling water flooded the vessel.

The first publication about runaway electrons was written by Giovanelli in 1949. The existing theories, which can describe the runaway phenomenon and the non-linear effect of the runaway electrons on the plasma behavior, are quite successful.

Runaway electrons, due to high velocities, are effectively collisionless and they can be used as an effective probe to study the non- collisional, turbulent transport in tokamaks [20]. A topic of investigation has been the analysis of the orbits of the runaways which proved to be a slim helix along the magnetic field lines with a pitch angle of about 100 mrad. Other topics were the analysis diffusion coefficient of the runaways and the underlying magnetic turbulence for a specific case. It will be part of this thesis to extend those investigations. In other investigations it was shown that large magnetic islands can be filled with runaway electrons and the island structure can be made visible by the synchrotron radiation of the runaways. For about 20 years, the TEXTOR team has performed investigations on runaways and gained much experience.

The runaway probe described in this thesis is a continuation and supplement of these efforts.

Recently, the study of runaway electrons attracted increased interest because the escape of the energetic electrons can damage severely the vessel structures. The damage increases with the size of the device. A sudden loss of energy confinement, a so-called disruption, can also cause the generation of runaway electrons. Investigations of generation and loss processes of runaway electrons are an important issue for the future International Thermonuclear Experimental Reactor (ITER) [54, 87].

1.4 Textor

TEXTOR (Torus Experiment for Technology Oriented Research) is a medium size limiter tokamak [98]. The tokamak is intended to study plasma-wall interaction. For this purpose, TEXTOR has several ports which are fully equipped with various kinds of plasma edge diagnostics (spectroscopy, IR camera, thermocouple etc.). In order to prevent the plasma wall interaction ALT-II (Advanced Limiter Test) a limiter is installed to define the plasma boundary. ALT-II is also used to remove the heat flux and particles running from the plasma.

In order to reduce the impurity influx at TEXTOR the deposition of a protective amorphous film on the vessel wall is also used. Following the carbonization, boronization or siliconization process, depending on the used film, the effective ion charge Zeff is 1.1.

During several upgrades TEXTOR was equipped with, see Fig. 1.2 [98]:

- auxiliary heating systems (neutral beam injection, radio frequency heating, microwave heating),
- a toroidal pumped limiter,
- an upgraded magnetization coil,
- the Dynamic Ergodic Divertor (DED).

TEXTOR has an excellent access for diagnostics to domains near to the wall. It is equipped with following devices:

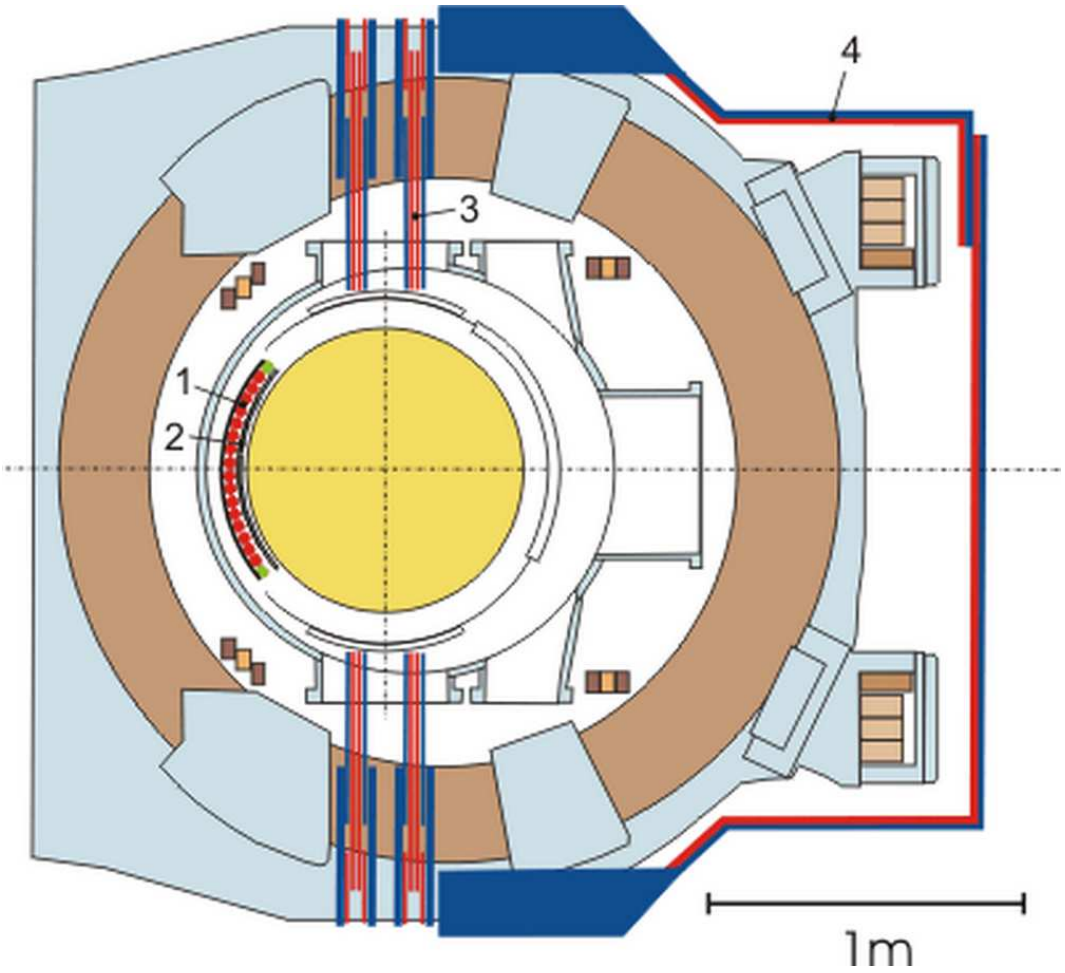

Figure 1.2: TEXTOR cross-section; 1 DED coils, 2 Divertor tiles, 3 DED current feedthrough, 4 DED bus bar.

- Tangentially neutral beam injectors,

- Two pairs of ICRH antennas,

- Pellet injector,

- Powerful set of the diagnostic tools.

1.5 This Thesis

Highly relativistic (runaway) electrons produced during disruptions can play a crucial role for present big tokamaks like JET, JT-60 and particularly for the future International Thermonuclear Experimental Reactor (ITER) [54, 87]. Runaway electrons due to their high energies can easily penetrate through the plasma facing material and destroy it. Additionally, strong x-ray radiation is produced. Possible damages and the flux of the radiation depend strongly on the energy distribution of runaways and on their density coming to the facing wall of the tokamak. The most important information, which is necessary to know about runaway electrons is their absolute number, density of the runaway flux incident on the plasma facing material and their energy distribution.

At the present time, different methods (neutron, x-ray, synchrotron radiation measurements and etc.) are used to study the runaway electron production and only few of them like synchrotron radiation measurements [29] can provide an absolute number of runaways with energies above 20 MeV produced inside the plasma. Recently a new technique to study the electron spectrum by means of a scanning probe was reported in several publications [65, 66]. The probe consists of a set of YSO ($Y2SiO5 : Ce$) crystals [107] which were shielded by different thicknesses of tungsten or stainless steel filters. The spectral analysis from the measured signals is performed using the Monte-Carlo Geant4 simulation code [42].

Measurements of runaway electrons with the newly developed diagnostic have been performed in the TEXTOR tokamak. The combination of the new probe with synchrotron radiation [29] and neutron detectors [56] allows to study runaway electrons in the interior and exterior regions of the plasma. In the thesis the following issues are considered:

* A new diagnostic to measure a spectrum of runaway electrons and their absolute number is described in Chap. 3.

* Runaway electron production at different plasma densities during the low density plasma discharge is discussed in Chap. 4.

* In the scanning mode the probe provides information about spatial distribution of runaway electrons at the plasma edge. In Chap. 4, it is shown that 2 cm outside of the last closed flux surfaces the population of runaways degrades.

* Runaway electrons are strongly affected by the magnetic field fluctuations. In the Chap. 5-7 measurements of the electron transport are performed by means of the new probe. It was investigated how runaway electrons behaves in the presence of internal magnetic turbulences, which increase with decreasing magnetic fields (Chap. 5-6) or in the externally applied fluctuations by the dynamic ergodic divertor (DED) [33].

* In Chap. 8 measurements of runaway electrons produced during the plasma disruptions are carried out. Such important parameters like temporal evolution of runaway electrons, their absolute number and energy distribution are studied during the thermal and current quenches. Using two thermocouples, the thermal load in the tungsten due to the incident runaway electrons is measured. Additionally, during a few discharges strong MHD activities appeared, that lead to the sudden loss of runaway electrons produced at the start up of the discharge and a subsequent plasma disruption.

Chapter 2

Runaway electrons

2.1 Electron runaway

The toroidal electric field E in a tokamak is the reason of the phenomenon of electron runaways [17]. Electrons experience an accelerating force $F_e = eE$ and a drag force resulting from Coulomb interaction with plasma particles.

For relativistic electrons a derivation of the drag force [40], including electron-ion and electron-electron collisions, gives:

$$\mathbf{F_d} = -\frac{e^4 n_e \ln\Lambda}{4\pi\epsilon_0^2 m_e v^2}\left(1 + \frac{Z_{eff}+1}{\gamma}\right). \tag{2.1}$$

Here e and m_e are the electron charge and rest mass, n_e is the electron density, $\ln\Lambda$ is the Coulomb logarithm, v is the electron velocity, $Z_{eff} \equiv \sum_i n_i Z_i^2/n_e$ is the effective charge number of the ions, ϵ_0 is the vacuum permittivity and $\gamma \equiv (1-(v/c)^2)^{-1/2}$ is the relativistic factor, c is the speed of light. In the expression Eq. (2.1), the first term is responsible for the energy exchange due to electron-electron collisions, the second one for the pitch angle scattering which disappears for the high energies.

In the case of non-relativistic electrons, $\gamma \to 1$, the drag force is written as:

$$\mathbf{F_d} = -\frac{e^4 n_e \ln\Lambda\,(2+Z_{eff})}{4\pi\epsilon_0^2 m_e v^2}. \tag{2.2}$$

The collision frequency in a Maxwellian distributed plasma, in the presence of

the electric field is approximated by:

$$\nu_{\mathbf{ee}} = \frac{|dp/dt|}{p} = \frac{|eE + F_d|}{\gamma m_e v}. \tag{2.3}$$

In the case of the tokamak plasma, the values E, n_e, T_e and Z_{eff} meet usually the conditions, that $eE \ll F_d$, so that the collision frequency is $\nu_{e,eff} \approx |F_d|/\gamma m_e v$. The distinction between relativistic and non-relativistic cases is defined by the critical velocity of the electron. Electrons with velocity exceeding the critical one are affected by the drag force described in the expression Eq. (2.2). For the electron with critical velocity, the drag force balances the electric force; in this case the critical velocity is given by:

$$v_{crit} = \sqrt{\frac{e^3 n_e \ln\Lambda\,(2 + Z_{eff})}{4\pi\epsilon_0^2 m_e E}}. \tag{2.4}$$

Electrons with velocities $v > v_{crit}$ are called runaway electrons. The electric force exceeds the drag force; as a consequence runaway electrons will be accelerated effectively. Therefore the kinetic energy of the electron should be at least W_{crit} in order to become a runaway electron, where:

$$\mathbf{W_{crit}} = \frac{1}{2} m_e v_{crit}^2 = \frac{e^3 n_e \ln\Lambda\,(2 + Z_{eff})}{8\pi\epsilon_0^2 E}. \tag{2.5}$$

The electric field for which a thermal electron ($v_{th} = \sqrt{2T_e/m_e}$) becomes a runaway electron is called the critical electric field, E_{crit} is given by:

$$\mathbf{E_{crit}} = \frac{e^3 n_e \ln\Lambda\,(2 + Z_{eff})}{8\pi\epsilon_0^2 T_e}. \tag{2.6}$$

Neglecting the electron-electron collisions and assuming that $Z_{eff} = 1$, $E_{crit} = E_D$, where $E_D = \frac{e^3 n_e \ln\Lambda}{4\pi\epsilon_0^2 T_e}$ is the Dreicer field [17].
In the case that the electric field E applied to the plasma is much less than this critical electric field ($\epsilon \equiv E/E_{crit} \ll 1$), the distribution function stays close to a Maxwellian and only an exponential small fraction of the electrons will runaway. For typical TEXTOR parameters ($n_e = 10^{19}\ m^{-3}$, $\ln\Lambda = 16$, $Z_{eff} = 2$, $T_e = 1.5$ keV and $E = 0.1$ V/m), the critical velocity $v_{crit} \approx 0.6c$ and critical energy $W_{crit} \approx 100$ keV [20]. Hence, $\epsilon \approx 0.02$ and the electron

distribution function stays close to Maxwellian.

2.2 Runaway electron generation

The study of generation processes of runaway electrons in the tokamak plasma was firstly proposed by Dreicer [17]. If a sufficiently strong electric field is applied in the plasma, some electrons experience unlimited acceleration. The process is called the primary generation process. In more recent time, the other possible mechanism, so called secondary generation process, responsible for the runaway generation, was first pointed out by Sokolov [95]. Particular in large tokamaks, the acceleration rate can increase significantly due to the "short-range" collisions of the fast and thermal electrons, where the already existing runaway electron can create a new one, while still remaining above that runaway energy threshold itself. Further, both processes are going to be reviewed.

2.2.1 Primary generation

An electric field applied to the plasma can cause unlimited acceleration of some electrons, 'runaway' electrons. In Sec. 2.1. it was shown that the friction field is a non-monotonic function of the electron velocity, $F(v) \sim v^{-2}$. Therefore, for electrons with large enough velocities the electric field will exceed the friction force and electrons can be accelerated to very high energies. If the electric field is high enough to exceed the Dreicer field,

$$\mathbf{E_D} = \frac{e^3 n_e \ln \Lambda}{4\pi\epsilon_0^2 T_e}, \tag{2.7}$$

then the electric force, accelerates an electron, exceeds the maximum friction force $F(v_{th}) \sim m_e \hat{\nu}_{ee} v_{th}$ ($\hat{\nu}_{ee} = \nu_{ee}(v/v_{T_e})^3$ and $Z_{eff} = 1$), and even the thermal part of the electron distribution can experience unlimited acceleration and the plasma cannot be in steady state. For a week electric field, $E_\parallel \ll E_D$, applied to a homogeneous, Maxwellian distributed plasma, the production rate of runaway electrons is defined by the diffusion of particles into the runaway region. Several authors [17, 47, 64, 67] have considered the problem of determining the production rate of runaways in a non-relativistic approximation.

The Fokker-Planck equation for a fully ionized, infinite plasma in a homogenous and constant electric field E, $E \ll E_D$ was solved.

$$-\frac{\mathbf{eE}}{\mathbf{m_e}} \cdot \frac{\partial \mathbf{f}}{\partial \mathbf{v}} = \mathbf{C(f)}, \tag{2.8}$$

where C(f) is the Fokker-Planck collision operator for fast electrons colliding with Maxwellian bulk ions and electrons, i.e. [51],

$$-\frac{eE_\parallel}{m_e}\left(\frac{\partial f}{\partial v} + \frac{1-\xi^2}{v}\frac{\partial f}{\partial \xi}\right) = \\ = \hat{\nu}_{ee} v_{th}^3 \left[\frac{1+Z_{eff}}{2v^3}\frac{\partial}{\partial \xi}(1-\xi^2)\frac{\partial f}{\partial \xi} + \frac{1}{v^2}\frac{\partial}{\partial v}(f + \frac{T_e}{m_e v}\frac{\partial f}{\partial v})\right], \tag{2.9}$$

where $\xi = v_\parallel / v$ is the cosine of the pitch angle and Z_{eff} the effective ion charge. The runaway electrons are generated at the rate:

$$\frac{\mathbf{dn_r^{pr}}}{\mathbf{dt}} = \nu_{\mathbf{ee}} \mathbf{n_e} \lambda_{\mathbf{r}}, \tag{2.10}$$

where the birth rate is given by:

$$\lambda_{\mathbf{r}} = \mathbf{K(Z_{eff})} \epsilon^{-\mathbf{3(1+Z_{eff})/16}} \exp\left(-\frac{\mathbf{1}}{\mathbf{4}\epsilon} - \sqrt{\frac{\mathbf{1+Z_{eff}}}{\epsilon}}\right), \tag{2.11}$$

where $K(Z_{eff})$ is a weak function of Z_{eff} (from [45] K(1)=0.32, K(2)=0.43) and $\epsilon = |E_\parallel|/E_D \ll 1$. In [46] the relativistic effects are taken into account, for the relativistic electrons the drag force does not fall to zero and remains finite at the speed of light. Hence no runaway electron generation can occur if the electric field is less than the critical electric field defined in [46]:

$$\mathbf{E_c} = \frac{\mathbf{n_e e^3 \ln \Lambda}}{\mathbf{4\pi \epsilon_0^2 m_e c^2}} = \frac{\mathbf{T_e E_D}}{\mathbf{m_e c^2}}. \tag{2.12}$$

The condition, when the relativistic effect becomes important, is defined by $E_\parallel / E_D \lesssim T_e / m_e c^2$. The relativistic birth rate is given by:

$$\lambda_{r,rel} = \lambda_r \exp\left(-\frac{T_e}{m_e c^2}\left(\frac{\epsilon^2}{8} + \frac{2\epsilon^{3/2}}{3}\sqrt{1+Z_{eff}}\right)\right). \tag{2.13}$$

For the TEXTOR tokamak, during steady state operation $E \approx 0.1$ V/m, no runaway production occurs if $n_e \geq 4\pi\epsilon_0^2 m_e c^2 E/e^3 \ln\Lambda \approx 1.2 \cdot 10^{20} m^{-3}$, which exceeds the Ohmic density limit. Therefore the relativistic effect does not stop the runaway production in the Ohmic discharge, but nevertheless, the effect can play an important role, as a reduction of the birth rate, at the lower density plasma.

2.2.2 Secondary generation

For many years, the primary generation mechanism of the runaway electrons was considered the main mechanism responsible for the production of runaway electrons. In [12, 60, 90, 95] it was pointed out, that there is another mechanism, which can be more effective for the production of runaway electrons than the primary generation. In the Fokker-Planck equation Eq. (2.9) the Landau collision operator is used, where only distant collisions are taken into account and small deflections of the momentum vector occur. The close collisions were not taken in attention in the plasma with $\ln\Lambda >> 1$. Nevertheless, if the runaway electrons are already present in the plasma, such electrons can kick the thermal electrons into the runaway regime. As a consequence of such close collision processes, the exponential growth of the runaway population occurs. Since this process needs already primary generated runaway electrons, this mechanism is called secondary runaway generation. The most complete mathematical treatment of the secondary generation process using the gyrokinetic relativistic Fokker-Planck equation averaged over a particle bounce period was done in [90]:

$$-\frac{eE_\parallel \xi}{m_e c}\left(\frac{\partial f}{\partial p} - \frac{2\lambda}{p}\frac{\partial f}{\partial \lambda}\right) = C(f) + S, \tag{2.14}$$

where the normalized relativistic momentum $p = \gamma v/c$, $\gamma = \left(1 - \frac{v^2}{c^2}\right)^{-1/2}$, $\lambda = (1 - \xi^2)/B$ is the magnetic moment variable, B is the magnetic field strength and C(f) is the relativistic Fokker-Planck collision operator. The generation of the secondary runaway electrons, produced by the close collisions of primary relativistic electrons with thermal ones, is described by the avalanche source of runaway electrons, S, in Eq. (2.14).

The gyro-kinetic relativistic Fokker-Planck equation Eq. (2.14) was solved analytically in several limits in [90]. The interpolation formula was found for the runaway production rate:

$$\frac{\mathbf{dn_r^{sec}}}{\mathbf{dt}} \simeq \frac{(\mathbf{E}-\mathbf{1})\mathbf{n_r}}{\tau \ln \mathbf{\Lambda}} \sqrt{\frac{\pi\varphi}{\mathbf{3(Z_{eff}+5)}}} \times \\ \times \left(\mathbf{1} - \frac{\mathbf{1}}{\mathbf{E}} + \frac{\mathbf{4\pi(Z_{eff}+1)^2}}{\mathbf{3\varphi(Z_{eff}+5)(E^2+4/\varphi^2-1)}}\right)^{\mathbf{-1/2}}, \quad (2.15)$$

where $E = E_{\|}/E_c$ is the normalized electric field, $\tau = (c/v_{th})^3 \hat{\nu}_{ee}^{-1}$ is the collision time for relativistic electrons and $\varphi \approx (1 + 1.46(r/R)^{1/2} + 1.72r/R)^{-1}$ describes the effect of finite aspect ratio R/r [90].
In the approximation of $E \gg 1$, $Z_{eff} = 1$ and $r/R \to 0$, the growth rate is approximated, as:

$$\frac{\mathbf{dn_r^{sec}}}{\mathbf{dt}} \simeq \sqrt{\frac{\pi}{\mathbf{2}}} \frac{(\mathbf{E}-\mathbf{1})\mathbf{n_r}}{\mathbf{3}\tau \ln \mathbf{\Lambda}}. \quad (2.16)$$

2.3 Runaway orbits

In a magnetized plasma, the charged particles follow in a first approximation the magnetic field lines. Due to the toroidal geometry of the tokamak, the magnetic field is nonuniform: it has gradients and curvatures. Therefore, particles do not follow the magnetic field lines exactly, but drift across the magnetic field. Basic expressions for electron orbits will be present in this section.
In the tokamak plasma the electron orbit is defined by three motions:

- The electron gyrates around the magnetic field lines with cyclotron frequency ω_{ce}:

$$\omega_{ce} = \frac{eB}{\gamma m_e}, \quad (2.17)$$

and Larmor radius ρ_{Le}:

$$\rho_{Le} = \frac{\gamma m_e v_\perp}{eB}, \quad (2.18)$$

where B is the magnetic field, $v_\perp$ is the perpendicular electron velocity with respect to the magnetic field direction and $\gamma = 1/\sqrt{1 - v^2/c^2}$ is the relativistic factor.

- The guiding center follows the helicity of magnetic field lines, where the guiding center is the center of mass of the electron averaged over the gyration motion, along the field lines:

$$v_{\parallel} = v_{\phi}\hat{e}_{\phi} + \frac{v_{\phi}B_{\theta}}{B_{\phi}}\hat{e}_{\theta} - \frac{v_{\phi}B_{z}}{B_{\phi}}\hat{e}_{z}, \tag{2.19}$$

  where $\hat{e}_{\phi}$, $\hat{e}_{\theta}$ and $\hat{e}_{z}$ are the unit vectors in the toroidal, poloidal and vertical direction respectively [58].

- The electron orbit is displaced from the magnetic field surface as a result of the curvature and the gradient of the magnetic field. Under normal tokamak conditions, the $\mathbf{E} \times \mathbf{B}$ drift is many orders of magnitude smaller than the Grad-B drift ($\mathbf{B} \times \nabla\mathbf{B}$) and the curvature drift ($\mathbf{R} \times \mathbf{B}$) and can be neglected. The drift velocity is given by:

$$v_{d} = \frac{1}{R\omega_{ce}}(v_{\parallel}^{2} + \frac{1}{2}v_{\perp}^{2})\hat{e}_{z}. \tag{2.20}$$

For runaway electrons, the drift velocity results in the displacement, Δ_{e}, of the runaway orbit away from the magnetic flux surface. This displacement is given in the first order approximation by:

$$\Delta_{e} \approx \frac{qW_{r}}{ecB}, \tag{2.21}$$

where q is the safety factor, W_{r} is the electron energy and B is the magnetic field. A more exact treatment of the runaway drift orbits was given by a Hamiltonian description in [74, 75].

2.4 Energy limits

A runaway electron can be effectively accelerated by the electric field. However the enormous increase of the runaway energy can be limited by:

* synchrotron radiation limit [5, 76]
* orbit shift limit [20, 58, 63]
* time limit [63]

* magnetic field ripple [68, 70, 77]
* bremsstrahlung [8, 9, 10, 28, 104]
* instabilities [35, 36, 37, 72, 103]
* magnetic turbulence [35, 36, 37, 103]

Synchrotron radiation limit

Relativistic electrons, moving along the curved magnetic field lines, emit electromagnetic radiation called synchrotron radiation. The total power lost by an electron due to the synchrotron radiation can be approximated by:

$$P_{syn} \approx \frac{2m_e c^3 r_e \gamma^4}{3R_c^2}, \tag{2.22}$$

where $r_e = e^2/4\pi\epsilon_0 m_e c^2$ is the classical Thomson electron radius and R_c is given in [91]:

$$\frac{1}{R_c} \approx \frac{1-\theta^2}{R} + \frac{eB\theta}{\gamma m_e c}. \tag{2.23}$$

In Eq. (2.23) $\theta = v_\perp/v_\parallel$ is the runaway pitch angle and R is the tokamak major radius. The energy gain of runaway electrons due to the motion in the toroidal electric field is $P_E = ecV_{loop}/2\pi R$.
The maximum energy, that an electron can reach in the presence of the synchrotron losses, is defined by the equilibrium $P_E - P_{syn} = 0$. In the TEXTOR tokamak, the experimentally defined pitch angle is $\theta = 0.1$ [58], $B = 2.2$ T (1.6 T$\leq B \leq$2.7 T), $V_{loop} = 1$ V and $R = 1.75$ m. The maximum energy, limited by synchrotron radiation, equals about 30 MeV.

Orbit shift limit

In the tokamak plasma an electron experiences the orbit drift outward of the plasma. As long as the orbit shift and drift orbit radius of the electron is smaller than the minor radius a, the electron is confined within the tokamak. In the TEXTOR tokamak from the analysis made in [20, 58] the orbit shift limit was found of about 80 MeV. In the analysis it was assumed that the orbit shift in Eq. (2.21) should be less than the minor radius of the tokamak ($a = 46$ cm).

Time limit

If the radiation losses are neglected, the energy gain of the runaway electron is mainly defined by the acceleration time. The maximum energy gain can be estimated, as:

$$W_{max}(t) = \int_0^t \frac{dW}{dt'} dt' = \frac{ec}{2\pi R} \int_0^t V_{loop}(t') dt' = \frac{ec}{2\pi R} \Phi(t) = 27\Phi(t)\ MeV, \tag{2.24}$$

where $\Phi(t)$ is the flux swing applied to the plasma. At about $t = 1$ s, $\Phi(t) > 1.1$ and increases further in time, i.e. at $t \geq 1$ s the energy limit due to the synchrotron radiation dominates on the time limit.

Magnetic field ripple

The discrete number of coils (N), which are responsible for the toroidal field production, leads to the slight modulation of this field at frequencies $\omega_{ripple} = nNc/R$. Due to the resonance between the electron gyromotion and the harmonics of the toroidal field ripple ($\omega_{ripple} = \omega_{ce}$ in Eq. (2.17)), an increase of the energy perpendicular to the magnetic field and therefore the power radiated by the electron occur. As a result an additional limit on the maximum runaway energy appears [58, 68, 70]. In the TEXTOR tokamak $N = 16$, and depending on the harmonic resonance and the amplitude of the field ripple an energy constraint of the runaways would occur for:

$$\gamma_{res} = \frac{eBR}{nNm_e c}, \tag{2.25}$$

which corresponds to an energy $W_{max}^{ripple} = 70/n$ MeV. According to [70], the strength of the resonance decreases with increasing harmonic number and for the ripple at TEXTOR tokamak it is expected that only the second harmonic resonance can limit the electron energy [58].

Bremsstrahlung

A new mechanism to limit runaway energies in disruption discharges was described in recent papers [8, 9, 10, 28, 104]. In controlling runaway energies in disruption-mitigation experiments: the enhancement of the emission

of the bremsstrahlung radiation by the runaway electrons via the injection of large amounts of high-Z impurities for a fast plasma shutdown by means of a radiative collapse [8, 104].

Instabilities

The runaway beam is directed in the forward direction with a pitch angle of about $\theta \approx 100\ mrad$ and has therefore a strongly anisotropic velocity distribution function and may excite various kinetic instabilities. A number of such possible instabilities were analyzed in previous works [19, 20, 39, 58, 83, 84, 86]. The anomalous Doppler resonance is responsible for an unstable interaction between accelerating runaways exceeding some critical energy W_{beam} and plasma waves. For the thermal electrons, the excited waves are simultaneously damped at the Cherenkov resonance. When the degree of anisotropy exceeds a critical level (i.e. the damping saturates), unstable waves are excited at the anomalous Doppler resonance, and the interaction with these waves leads to pitch-angle scattering of resonant electrons. The instability threshold is mainly determined by the considered runaway distribution function and the damping mechanisms. In [19] a distribution function relevant to primary (Dreicer) generation of runaways is considered. A distribution function which is relevant for runaway electrons produced by the secondary generation process was analyzed in [39, 86]. It was shown that a destabilization of magnetosonic-whistler waves can occur due to the secondary produced runaways at the Doppler-shifted harmonics of the cyclotron frequency.
In [20, 58] a fast pitch angle scattering (FPAS) was measured by the synchrotron radiation for electrons with energies of about 25 MeV during the current decay phase. The pitch angle increases with a factor of about 1.5 (from about 0.1 to a value of 0.17), which will decrease the radiation limit to 20 MeV. It is interesting to note that runaway production in those experiments was mainly determined by the secondary generation process.

Magnetic turbulence

Recently described in [35, 36, 37, 103] experiments were performed in the presence of externally applied magnetic turbulences (by means of the dynamic ergodic divertor (DED)). An increase of the runaway transport was measured.

From the synchrotron and electron cyclotron emission (ECE) measurements, it was shown that during the DED phase an enhanced loss of low energy runaway electrons reduces their confinement time and prevents them from further acceleration. As a result the reduction of the maximum runaway energy occurs.
Similar results will be presented in this thesis in Chap. 7, where the spectrum of runaway electrons is measured by a new probe during the DED phase. Additionally, the reduction of the maximum runaway energy is observed in the presence of the increased internal magnetic fluctuations at the low magnetic field of about 1.6 T. This will be discussed in Chap. 6.

2.5 Runaway transport

Neoclassical theory allows the calculation of transport coefficients in a quiet plasma with nested toroidal magnetic surfaces [41]. In the analysis only Coulomb collisions between the charged particles are taken into account. The experimentally measured energy transport via electrons is two orders of magnitude larger than it is predicted by the neoclassical theory. The high degree of anomaly in the diffusion coefficient is mainly ascribed to the turbulent processes in the plasma with various types of instabilities of either electrostatic or magnetic origin. Runaway electrons due to their high momentum are mainly affected by magnetic turbulence [13]. Therefore they can be used as a possible probe to study magnetic fluctuations in the plasma [21, 79, 80].
Sensitivity of runaway electrons to the main transport mechanisms is considered in this section.

Collisions

In a uniform magnetic field the diffusion coefficient of the electron is determined very simply

$$D \simeq < \Delta x >^2 \nu_e = \rho_e^2 \nu_e, \tag{2.26}$$

where ρ_e is the electron Larmor radius and ν_e is the collision frequency. In the TEXTOR tokamak $\rho_{e,rel} = 0.5$ cm for electrons with energies of about 25 MeV [58] and $\nu_{e,rel} \approx 10$ s, which is obtained from Eq. (2.3) in the case of $eE \ll F_d$ and $\gamma = 60$. Hence, the diffusion coefficient is about $10^{-6}\ m^2 s^{-1}$.

In the case of the neoclassical approximation the runaway electrons experience an outward orbit shift (Δ_e) due to the toroidal geometry of the tokamak. In this case the Larmor radius is about one order of magnitude less than the orbit shift, which is approximated in Eq. (2.21). If the orbit shift is used instead of the Larmor radius as a measure of the typical neoclassical scale step length, the diffusion coefficient can be estimated as $D_{neo} \simeq \Delta_e^2 \nu_e \sim 10^{-4}\ m^2 s^{-1}$.

Electrostatic fluctuations

The presence of the electrostatic fluctuation results in the $\mathbf{E} \times \mathbf{B}$ drift. The normal component of the fluctuating electric field $\tilde{E}_\perp$ to the magnetic field, gives rise to a drift velocity $\tilde{v} \sim \tilde{E}_\perp / B$. This leads to the diffusion coefficient

$$D \simeq \frac{< \Delta x >^2}{\tau_{trans}} \approx \frac{\pi q R}{v_\parallel} \left(\frac{\tilde{E}_\perp}{B} \right)^2, \tag{2.27}$$

where the transit time is approximated, as: $\tau_{trans} = \pi q R / v_\parallel$. In the TEXTOR tokamak for thermal electrons $\chi_e \approx 1\ m^2 s^{-1}$, $c/v_{th} \approx 30$. Therefore, $D_{rel} \approx 0.03\ m^2 s^{-1}$.

Magnetic fluctuations

Fluctuations in the magnetic field may destroy the magnetic surfaces. If the electron follows the magnetic field lines, i.e. collisions and the drift motion due to the magnetic field gradient and curvature are neglected, runaways diffuse radially out of the plasma with the diffusion coefficient of the order

$$D_{RR} = \pi q v_\parallel R \left(\frac{\delta B}{B} \right)^2, \tag{2.28}$$

which was firstly derived by Rechester and Rosenbluth [88]. However it was later shown in [78] that the finite Larmor radius and magnetic drift velocity of the runaways can substantially reduce the diffusion coefficient.
In the model by Myra and Catto [80], the effect of the orbit shift was taken into account. It was shown that depending on the poloidal structure of the magnetic turbulence the diffusion coefficient can vary slowly (algebraically) or rapidly (exponentially) with Δ_e / Δ_m (Δ_m is the mode width). The diffusion

coefficient is written as $D_{MC} = \Upsilon D_{RR}$, where Υ is the energy dependent drift parameter.

In [22] measurements of the diffusion coefficient was performed for electrons with energies of about 25 MeV and $D \approx 0.01\ m^2 s^{-1}$. This value is of the same order as was predicted for a diffusion coefficient in the presence of the electrostatic fluctuation. However. it was also discussed in the same paper that for electrons with energies of about 1 MeV ($v_{\|} = c$) the diffusion level is at leat one order of magnitude higher than it is predicted for electrons with energies of 25 MeV at the same magnetic fluctuation level. In the model by Myra and Catto [80], this effect can be explained by the dependence of the shielding factor Υ on the electron energy. Thus, it is expected that the radial transport of runaway electrons is much stronger affected by the magnetic turbulence than by the electrostatic fluctuations.

In Chap. 5 and Chap. 6 the diffusion coefficients and corresponding magnetic fluctuation level are analyzed from synchrotron and probe measurements using the model by Myra and Catto [80].

Chapter 3

Diagnostics

3.1 Introduction

The study of relativistic electrons produced in tokamak plasmas (runaway electrons) [54, 87] or laser produced plasmas [27, 53] requires well developed and absolutely calibrated diagnostic systems. Extra additional constraints like strong magnetic fields, extremely high energy heat flux coming from the plasma in the case of the tokamak machines apply additional requests to such kinds of diagnostics.

Highly relativistic (runaway) electrons produced during disruptions can play a crucial role for present big tokamaks like JET, JT-60 and particularly for the future International Thermonuclear Experimental Reactor (ITER) [54, 87]. Runaway electrons can easily penetrate through the plasma facing material due to their high energies and destroy it. Additionally, strong x-ray radiation is produced. Possible damages and the flux of the radiation depend strongly on the energy distribution of runaways and on their density coming to the facing wall of the tokamak. It is important to know of runaway electrons, their absolute number, the density of the runaway flux incident on the plasma facing material and their energy distribution.

At the present time, different methods (neutron, x-ray, synchrotron radiation measurements, etc.) are used to study runaway electron production and only few of them like synchrotron radiation measurements [29] can provide an absolute number of runaways with energies above 20 MeV produced inside the plasma. Recently a new technique to study the electron spectrum by means of

a scanning probe was developed [65, 66]. The probe consists of a set of YSO ($Y_2SiO_5 : Ce$) crystals [107] which were shielded by different thicknesses of tungsten filters. The spectral analysis from the measured signals is performed using the Monte-Carlo Geant4 simulation code [42].

Additionally, the probe was used to make local measurements of relativistic electrons produced by a femto-second laser in the experiments related with the 100 TW laser system.

The diagnostic fills a gap by measuring the runaways directly at the plasma edge. In addition, the runaway electrons are studied in the plasma by synchrotron emission and at the wall by neutron detection. In combination with the scanning probe the runaway electrons were studied in the interior and exterior region of the plasma. The experimental set-up which has been used to measure runaway electrons is shown in Fig. 3.1.

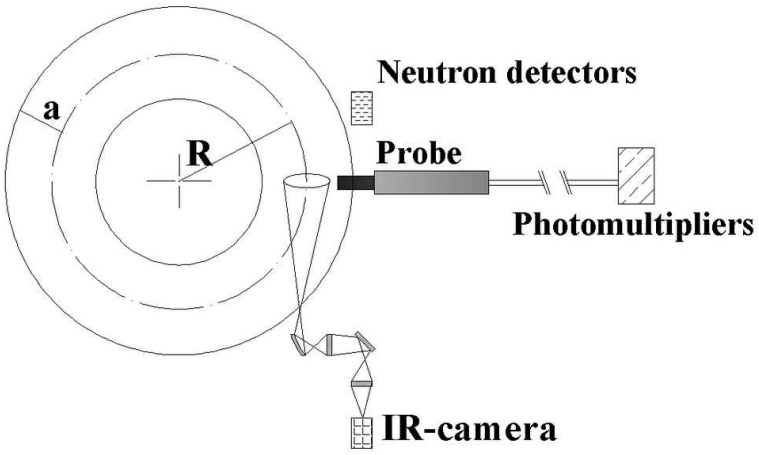

Figure 3.1: *The experimental set-up. Synchrotron radiation can register runaways with energies higher than 25 MeV in the plasma center. The probe measures electrons at the plasma edge and detectors register neutrons produced due to photonuclear reactions by electrons, which escaped the plasma confinement.*

3.2 Scanning probes

3.2.1 Design of probes

First probe

Three generations of probes were developed to provide information about the spectrum of runaway electrons. The first one is a rather simple design which shows the principle idea, see Fig. 3.2. A scintillator is located behind a 5 mm thick graphite housing. The second scintillator is separated by a piece of 8 mm tungsten. The graphite housing shields the detectors from the ambient light and low energy particles. Only runaway electrons with energies exceeding 3 MeV can pass through the graphite see e.g. [42] App. A. The tungsten separates runaways in the electron approach direction from those in the ion approach direction (positrons or background signal). However, it turned out that the runaways are scattered on the top plate of the graphite such that the remote scintillator also sees runaways. The signal of the remote scintillator was used because the first one became strongly saturated during typical runaway discharges.

The crystals have the following characteristics: light output of 30 000

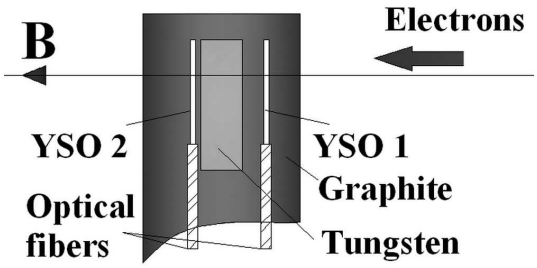

Figure 3.2: *The first probe design, the presented part of the probe demonstrates the position of the YSO crystals inside the graphite housing. The second crystal is shielded by 8 mm tungsten, which allows to measure only scattered runaway electrons in the graphite housing with a spatial resolution of 2 cm.*

photons/MeV [107], melting point of 2470 degree Celsius, length 20 mm, cross section of 1 mm^2, decay time and peak emission of 42 ns and 420 nm respectively. The main characteristic of the crystals is that the light output does not change considerably (10 %) for γ-rays with energies higher than 100 keV [7], a similar result can be expected for electrons in the same energy range. The

crystal length was chosen in order to have enough signal. For the present purpose, the probe is inserted relatively slowly to the plasma edge with a velocity of 0.5-0.7 m/s.

Light, produced by the incident electrons in the crystals is transferred by optical fibres to a Hamamatsu R928 photomultiplier tubes. An application of optical fibres allows to avoid a negative influence of the magnetic field on the electronic components of the diagnostic.

Second probe

The positive results of the first probe encouraged the development of a second probe type which is shown in Fig. 3.3). The aim is to resolve runaway electrons with energies between 4 and 30 MeV with an energy resolution of about 3-4 MeV. The same type of YSO crystals as in the first probe was used, but their length was reduced to 2 mm; as this length provides sufficient signal and a good radial resolution. The probe consists of 10 crystals [107, 7], which are shielded by different thicknesses of tungsten filters (between 0 and 6 mm) placed in the runaway electrons' direction. It is significant to note that from the other directions the crystals are properly shielded by more than 6 mm tungsten. The outside of the probe is covered by a 5 mm graphite housing. With this set-up a spatial resolution of 2 mm is obtained.

The analysis of the measured energy range by the probe was carried out

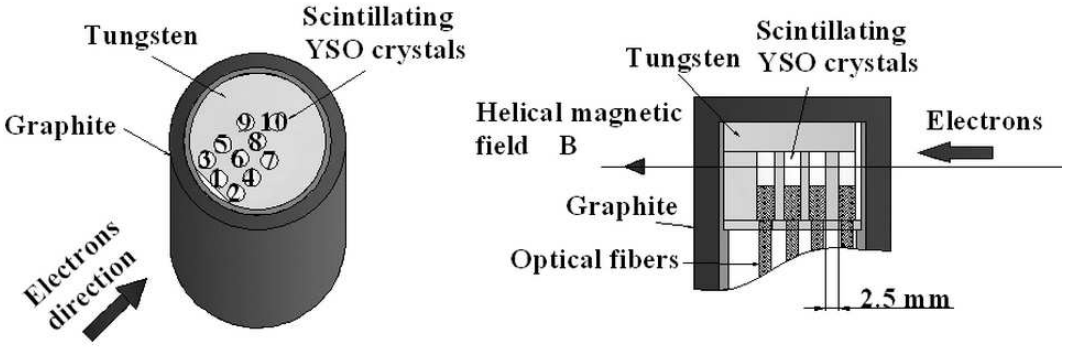

Figure 3.3: *The design of the second probe. The probe consists of ten YSO crystals and has 2 mm spatial resolution. The light produced in the crystals is transferred to photomultipliers by optical fibers.*

using the Monte-Carlo Geant4 simulation code [42]. In the simulations a real

3D geometry of the probe and a mono-energetic electron beam source were applied. Simulations were carried out for electron beams with different energies. For each simulation, the number and energy of the electrons were kept constant. The absorbed energy in the crystal per one electron (gamma) passing through the crystal is a slowly varying function of the electron (gamma) energy between 1 MeV and 40 MeV. The deposited energy in the crystal is about 700 keV (15 keV) per one electron (gamma). Since the absorbed energy does not depend strongly on the electron (gamma) energy, the signal produced by an electron in the crystal is two orders of magnitude higher than by a gamma with the same energy.

The total absorbed energy in 3D Geant4 simulations by each crystal, see Fig. 3.4 a), reduces proportionally with increasing thickness of the tungsten filters. The minimum electron energy registered by each crystal is defined from the approximation that the total absorbed energy in the appropriate crystal reduces ten times from its maximum value. In Fig. 3.4 b), the minimum measured electron energy by each crystal is shown. Therefore the probe can resolve electrons with energies between 4 MeV and 40 MeV.

The spectral analysis of the measured relativistic electron beam was implemented under certain conditions: i) every crystal can register electrons with energies higher than the corresponding minimum energy, see Fig. 3.4 b); ii) all electrons registered by the crystal produce the same light output. The second condition is fulfilled by the characteristics of the crystal [7] and due to the fact that electrons with energies in the measured energy range lost almost the same amount of energy in the crystal. The minimum detected energy was defined under the assumption that the absorbed energy reduces by a factor of ten. In this case the measured spectrum will not be substantially modified by the probe itself due to the absorption of part of the transported electrons in the tungsten filters. At the same time the influence of less energetic electrons on the produced signal leads to an error in the spectral measurements of about 20 %.

In the TEXTOR tokamak electrons can be accelerated up to a maximum energy of 30 MeV. This maximum is defined by synchrotron radiation losses, [29, 58]. In order to get information about the runaway electrons' spectrum in the energy range between 4 MeV and 30 MeV, signals from the first seven crystals were used. Light intensities produced in each crystal can be written

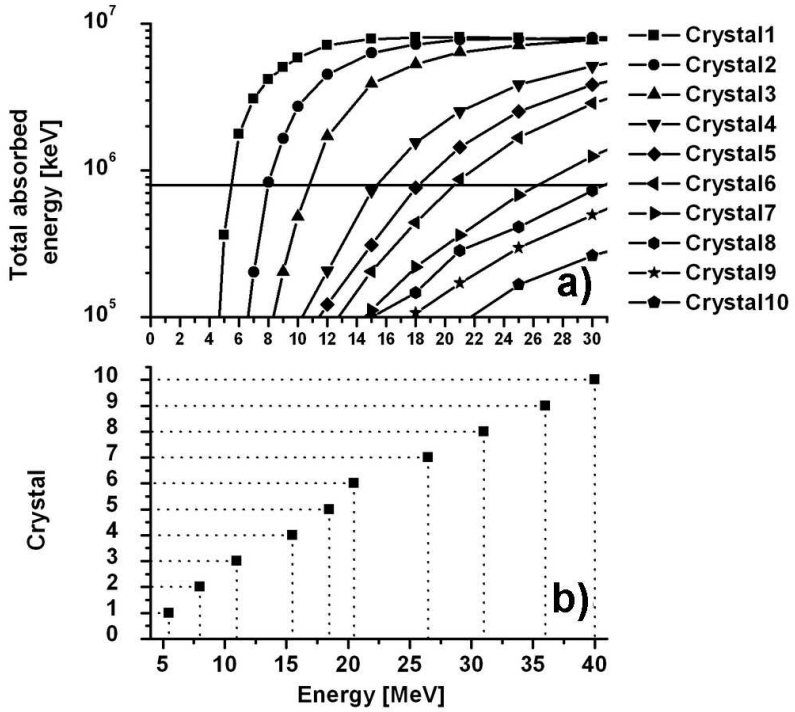

Figure 3.4: *a) 3D Monte-Carlo* Geant4 *code simulations of the total absorbed energy by each crystal in the probe. b) Electron energy range measured by the probe.*

as:

$$\begin{cases} I_1 = \alpha n_1 + \alpha n_2 + \ldots \quad + \alpha n_7 \\ \qquad \ldots \\ I_i = \alpha n_i + \ldots \quad + \alpha n_7 \\ \qquad \ldots \\ I_7 = \alpha n_7, \end{cases} \tag{3.1}$$

where I_i is the light intensity produced in the i-th crystal, α is the light intensity produced by one electron and n_i is the number of electrons with energies between two minimum energies defined for the i-th and (i+1)-th crystals (for example: n_1 is the number of electrons with energies between 4 MeV and 8 MeV). Hence the total number of electrons, N_e, with energies between 4 MeV and 30 MeV is $N_e = \sum_{i=1}^{7} n_i$. Consequently, the distribution of electrons in the defined energy range can be found from the ratio of the light intensities in the crystals.

Measurements of the runaway electron spectrum were performed with

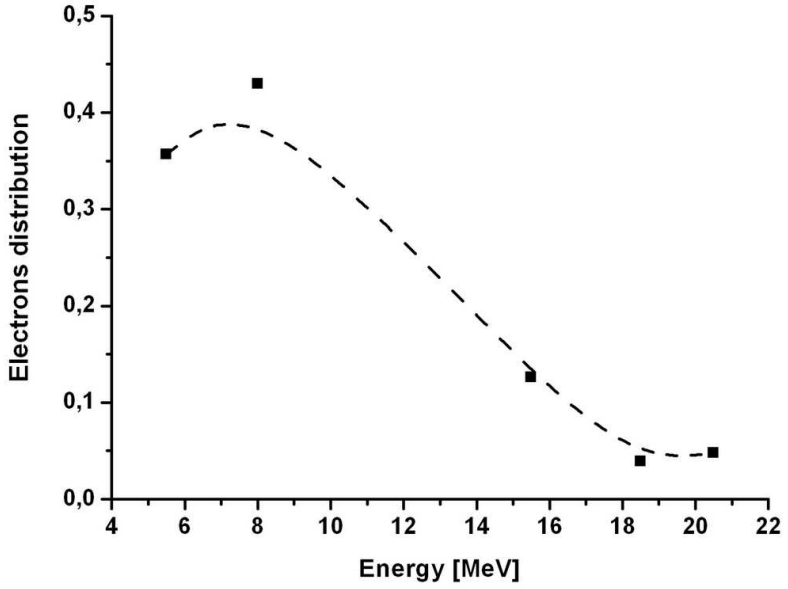

Figure 3.5: *Runaway electron spectrum measured during a low density plasma discharge. The probe was inserted to the Last Closed Field Surface at 1.15 s into the discharge.*

the following plasma parameters: plasma density $n_e = 0.9 \cdot 10^{19}\ m^{-3}$; plasma current $I_p = 300$ kA and magnetic field $B_t = 2.25\ T$. The probe was inserted to the LCFS at 1.15 s during the discharge. The measured runaway electron spectrum is shown in Fig. 3.5.

The probe can measure electrons with temporal resolution of about 0.05 ms, which was mostly limited by the data logger memory. The high temporal resolution of the probe allows to study runaway electrons produced during a plasma disruptions. In Fig. 3.6 the first measurements of runaway electrons during plasma disruptions by the scanning probe are shown. Fig. 3.6 a) shows the time trace of the plasma current during the disruption. The disruption is typically initiated by a negative voltage spike and a transient increase of the plasma current due to the lowering of the plasma inductance during the energy quench [72]. The current quench shows a small plateau during which runaway electrons are created.

Fig. 3.6 b) shows the probe signal. Here one can see two peaks, a larger one during the energy quench and a smaller one after the plateau phase of the

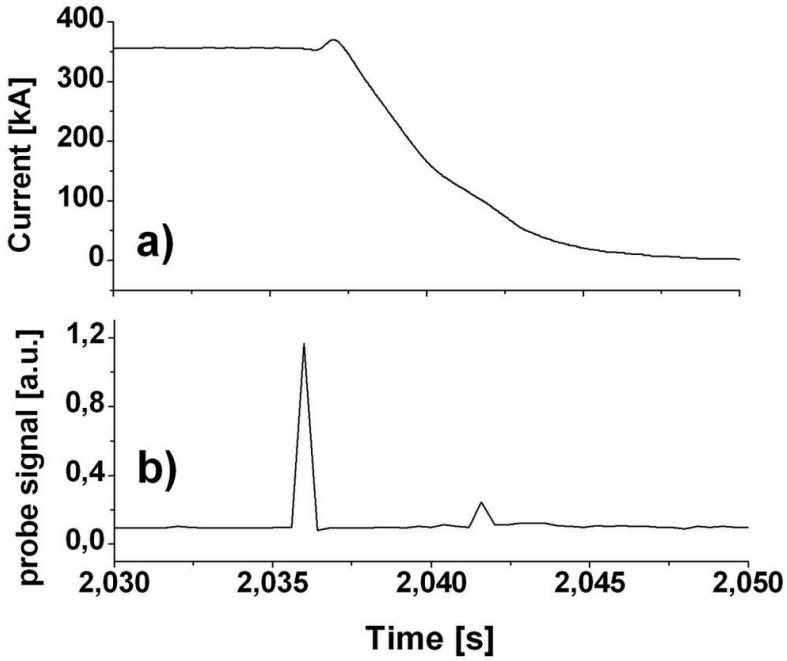

Figure 3.6: *a) Plasma current, plateau formation at 2.04 s; b) The probe measurements of runaway electrons with electron energies higher than 8 MeV. The probe was placed at the minor radial position of 47 cm.*

current quench. An origin of the first peak is the loss of runaways which were created during the start-up phase of the discharge [40, 68] and the second peak generated during the current quench phase [72].

Third probe

The experience gained from the operation of the first and especially of the second probe enables to create the third generation of probes. Improvements are related to the photomultipliers set-up, where a holder to control an incoming signal by means of the neutral density filters is added. Additionally the probe is equipped by two thermocouples in order to measure deposited energy due to the transport of runaway electrons through the probe, see Fig. 3.7.

In the third generation of the probe the YSO crystals are shielded by stainless steel walls instead of tungsten as in the second one. An application of the stainless steel instead of tungsten is defined by the stopping processes in the materials. During the transport of the electron through the material, it loses the energy due to the collisions with other particles and radiation. A critical

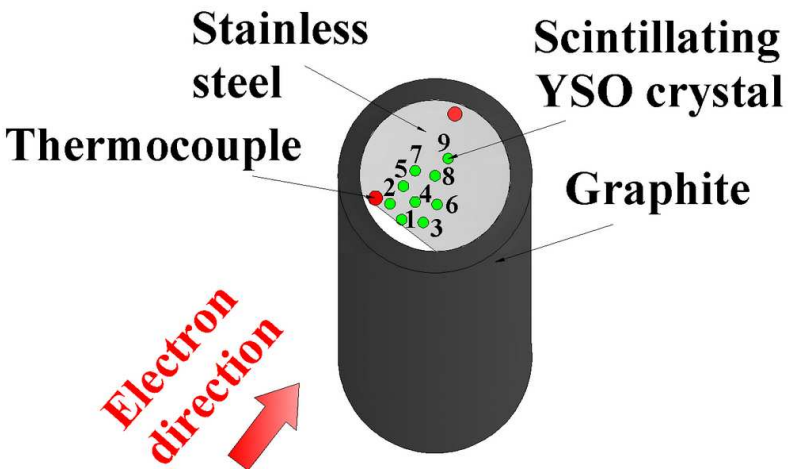

Figure 3.7: *The design of the third probe. The probe consists of nine YSO crystals and has 2 mm spatial resolution. The light produced in the crystals is transferred to photomultipliers by optical fibers. Additionally, the probe equipped by two thermocouples. The probe has 5 mm graphite mantel and depending on the crystal number the following thickness of stainless still is used from the incidence direction of electrons: crystal 1 - 0 mm; 2 - 1 mm; 3 - 2 mm; 4 - 2.5 mm; 5 - 3.5 mm; 6 - 4.6 mm; 7 - 5.5 mm; 8 - 7 mm and 9 - 9.5 mm. The tungsten filter is used to block electrons coming from the top.*

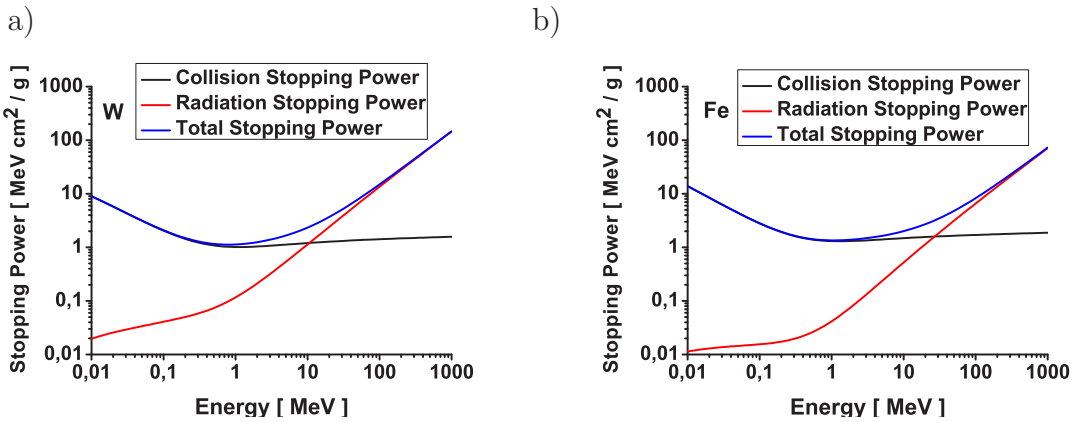

Figure 3.8: *a) Stopping powers for an electron in tungsten (W); b) Stopping powers for an electron in iron (Fe).*

energy of the electron above which the electron loses its energy mostly due to the radiation can be estimated approximately, as: $E_c\ [MeV] = 800\ [MeV]/Z$, where Z is the atomic number of the material. More precise calculations of the stoping power and the critical energy can be found for example in [24] and results of estimations of the stopping power of electrons for tungsten and iron are shown in Fig. 3.8. In Fig. 3.8 it can be seen, that electrons with energies more than 10.5 MeV for tungsten and more than 27 MeV for iron lose their energy mainly due to radiation. As the YSO crystal is also sensitive to gamma radiation, the reduction of the bremsstrahlung due to the electron transport will improve the precision in the spectrum definition. In the TEXTOR tokamak the maximum energy of runaway electrons is about 30 MeV [58], which makes stainless steel the more reliable material for the probe application. Additionally, stainless steel is much easier to machine than tungsten.

3.2.2 Absolute calibration

An improved analysis of the measured energy range using 3D Geant4 code for the third probe was performed. Additionally, an absolute calibration was carried out at the radiation source ELBE (Electron Linac for beams with high Brilliance and low Emittance, Forschungszentrum Dresden Rossendorf). A mono-energetic electron bunch with energies between 15 and 30 MeV was used for the calibration.

The set-up for the absolute calibration of the probe is shown in Fig. 3.9. A Faraday cup and an Integrated Current Transformer (ICT, Rogowski coil) are used to measure the charge of the electron bunch. The profile of the electron beam and its divergence are measured by two Lanex screens (scintillating screen Konica, the light from the screen was recorded by a CCD-camera). A distance between the first Lanex screen and the vacuum tube is 37.5 cm. The second Lanex screen was placed at 12 cm in front of the probe. The distance between the probe and the output of the electron bunch from the vacuum tube is 129 cm. A typical picture obtained from the Lanex screen placed in front of the probe is shown in Fig. 3.10 a) and the corresponding density distribution of the electron bunch, in Fig. 3.10 b). The density difference due to the 2D arrangement of the crystals inside the probe, see Fig. 3.7, does not exceed more

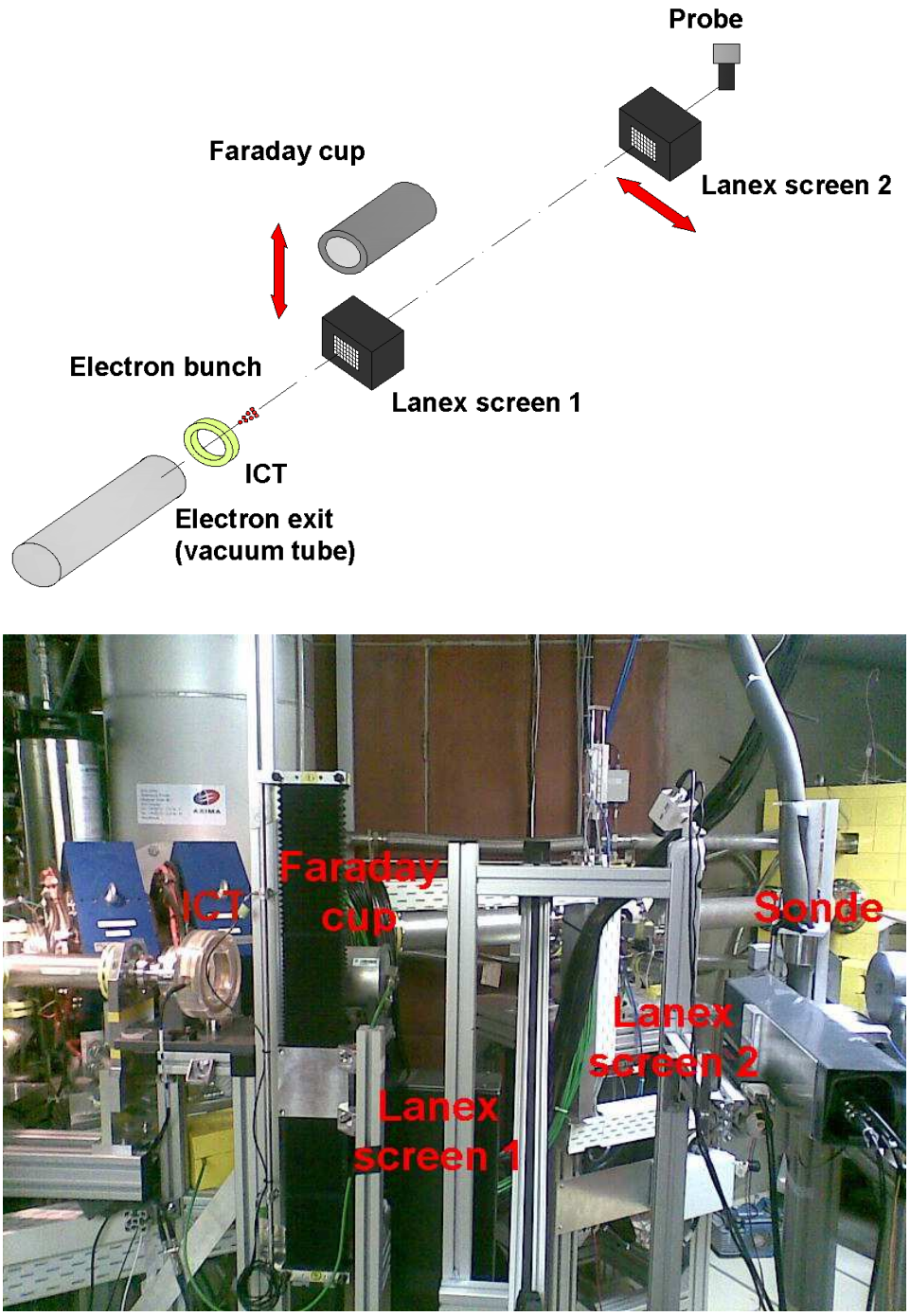

Figure 3.9: *ELBE set-up. Lanex screens and a Faraday cup were installed on the beam line to measure the beam parameters.*

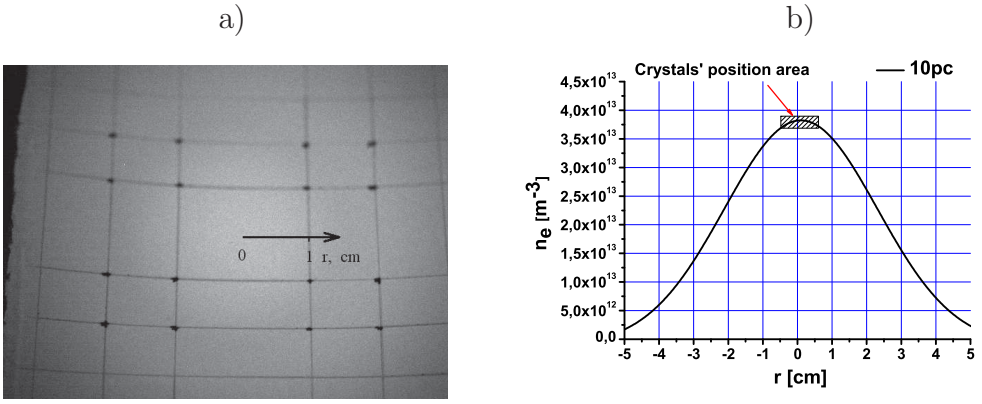

Figure 3.10: *a) Electron beam profile measured by the Lanex screen in front of the probe; b) Radial distribution of the electron density, electron beam has a charge of 10 pC. Positions of crystals are shown by the rectangle.*

than 3%. A divergence of the beam for electrons with energies of 20 MeV was about 0.03 rad. The calibration was carried out in the following steps: 1) cross calibrations of ICT and Faraday cup; 2) the beam profile measurements; and 3) electron probe measurements. ICT was used to control the charge of the beam during each shot.

The absolute number or the density of electrons incident on the probe was measured by the first crystal, which has only 5 mm graphite shielding. A possible error due to deflection or absorption of electrons passing through the graphite with energies higher than 4 MeV can be neglected. Measurements of the mono-energetic electron beam with an electron energy of 20 MeV were carried out for the first crystal calibration. The signal is shown in Fig. 3.11, for the total charge of the beam of 10 pC. As the time duration, τ, of the electron bunch is about 2 ps, all electrons came to the crystal simultaneously and the detected signal decay is determined by the system resolution. The temporal resolution is defined as the time interval of the e-times decay of the maximum of the signal and equals about 0.13 ms. This time is given by the output resistance at the cable end (1 MOhm) and the length of the BNC RG58 cable (1 m). The number of electrons passing through the crystal equals $N_{e,cr} = n_{e,p} c S_{cr} \tau$, where $S_{cr} = 2 \cdot 10^{-6}\ m^2$ is the crystal front surface, c is the speed of light and $n_{e,p}$ is the electron density in front of the probe. The electron density in front of the probe is estimated, from $Q = c\tau e \cdot \int\limits_{S_{beam}} 2\pi n_{e,o} i(r) r dr$, where Q is the

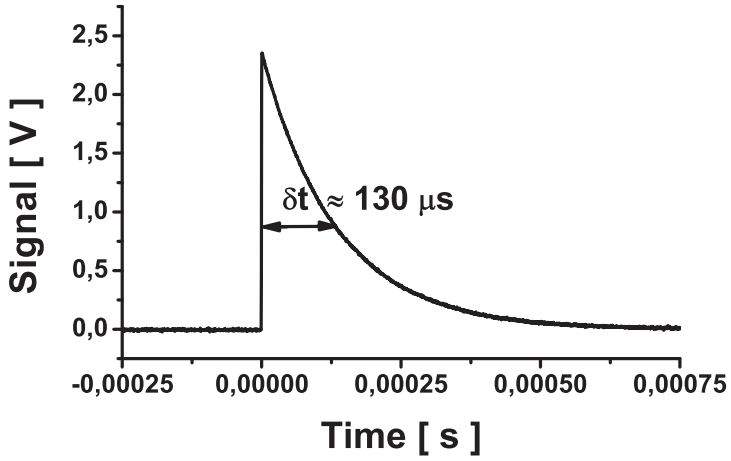

Figure 3.11: *A signal from the first crystal. A mono-energetic electron bunch with an electron energy of 20 MeV and a total charge Q of 10 pC. The temporal resolution is defined as the time interval of the e-times decay of the maximum of the signal.*

total beam charge, e is the electron charge, S_{beam} is the beam cross section, $i(r)$ density profile measured in front of the probe by means of the Lanex screen and $n_{e,o}$ is the maximum electron density in the center of the beam. Since the probe was placed in the center of the beam, then $n_{e,p} = n_{e,o}$. The signal from the first crystal of 2.35 V corresponds to about 46000 electrons. The gain of the photomultipliers is about 10^5.

A proportionality of the light yield of the crystal to the number of incident electrons was studied for electrons with energies of 20 MeV, where the charge of the electron bunch was varied between 1 and 50 pC from shot to shot. An analysis of the beam profile for different charges of the electron bunch shows a linear dependence of the output signal on the charge of the electron beam and on the number of electrons coming to the crystals, as shown in Fig. 3.12. The linear dependence of the light output to the number of incident electrons is an important characteristic of the crystal in order to measure the absolute number of electrons and their spectrum in the tokamak.

Another important characteristic of the YSO crystal, which simplifies substantially the further analysis of the measured number of electrons and their spectrum is the independence of the light output of the crystal on the energy of the passing electron in the measured energy range of the probe between 4 and 30 MeV [42]. A result of the measurements of the electron bunch with different

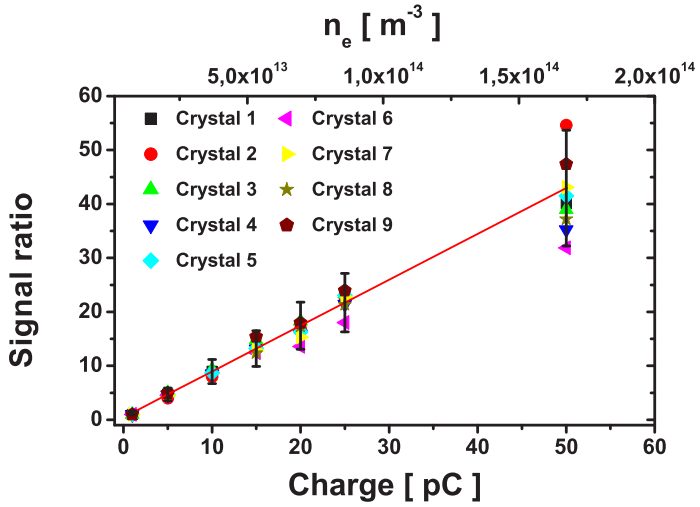

Figure 3.12: *Normalized signals change proportional to the charge of the electron beam and on the incident electrons' density for all crystals of the probe. Electron density as well as electron beam charge are proportional to the number of electrons hitting each crystal.*

energies but with the same number of incident electrons on the probe is shown in Fig. 3.13 a). The signal remains constant at different energies. During the calibration the electrons' energies were verified between 15 and 30 MeV. The energy range was defined by technical restrictions of the ELBE-accelerator. A similar analysis was performed by means of 3D Geant4 code simulation, where the absorbed energy per one passing electron with energies between 0.1 and 30 MeV has been simulated, as shown in Fig. 3.13 b). The absorbed energy increases from 100 up to 900 keV per one passing electron for electrons with energies between 0.1 and 1 MeV and becomes constant (about 700 keV) in the energy range between 3 and 30 MeV. The same trend was observed for γ-rays with energies between 0.1 and 30 MeV, with an absorbed energy of the order of 15 keV/per one gamma.

The 3D Geant4 code allows to make an analysis of the spectrum of the electron beam incident on the probe. Simulations with similar beam parameters as in the ELBE experiments were performed, where 10^6 mono-energetic electrons were incident on the probe and as an outcome the total absorbed energy by each crystal was provided. The absorbed energy is proportional to the measured light intensity from the crystal. Comparisons of the result

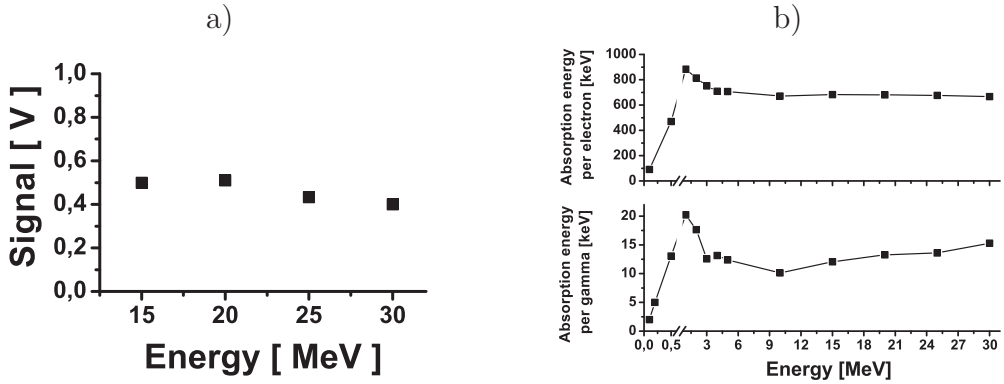

Figure 3.13: *a) Signal from the first crystal for different energies of electrons but the same incident electron numbers, electron density $n_e = 3.4 \cdot 10^{13}\ m^{-3}$, ELBE measurements; b) The absorbed energy in the crystal per one electron (gamma) passing through the crystal is a slowly varying function of the electron (gamma) energies between 3 MeV and 30 MeV, Geant4 simulations.*

obtained by the Geant4 simulations and ELBE experiments are made. Normalized signals to the signal from the first crystal for mono-energetic electron beams with energies between 15 and 30 MeV are shown in Fig. 3.14. Results obtained during the experiment are in good agreement with simulated ones. A discrepancy between experimentally obtained signal ratios and numerically ones does not exceed more than 50%. This uncertainty defines the energy resolution of the probe, which is discussed later in this section.

The main purpose of the probe is to provide information about the number of incident electrons and their distribution in the energy range between 4 and 30 MeV (4 MeV is the minimum energy of electrons which can be detected by the probe). It is of particular interest to measure the maximum energy of the main part of detected electrons. In the present analysis electron distributions with maxima at four different energy ranges are considered. The main interest is to predict what happens with the signal ratios if most of electrons are concentrated in one of the defined energy ranges, as shown in Fig. 3.15. Simulations of the absorbed energy by each crystal are performed by means of Geant4 code and corresponding ratios to the first crystal are shown in Fig. 3.15 e). Information about the electron spectrum can be obtained from the comparison of the measured signal ratios with the simulated ones. In Fig. 3.15 e) a clear difference in the simulated trends of the signal ratios can be seen for all considered

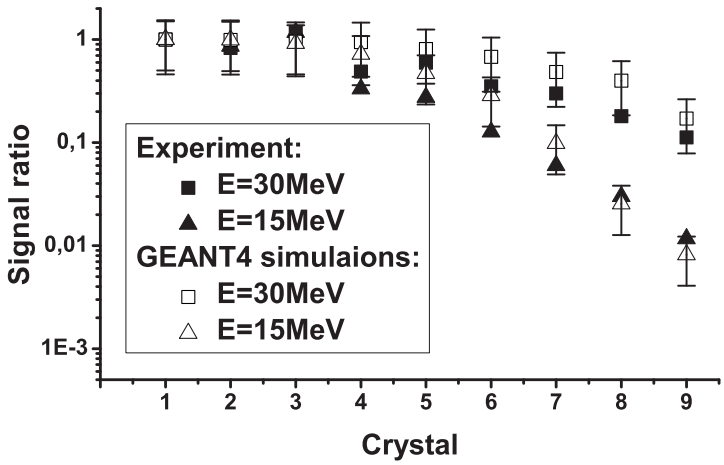

Figure 3.14: *Normalized signals are shown for electrons with energies between 15 and 30 MeV. Comparisons of the experimental results with simulations made using 3D Geant4 code are in good agreement.*

electron distributions in Fig. 3.15 a)-c). In the case of the predominance of the high energetic electrons, with energies higher than 20 MeV, the ratio of the signals from the last crystal to the first one is not lower than 10^{-1}, in contrast to the case with the dominance of the low energetic electrons where this ratio is already $7 \cdot 10^{-4}$. Moreover, the trend of the signal ratios from other crystals also changes for the distribution functions with the maximum at high and low electron energies. In Fig. 3.15 a); d) two distributions: exponentially growing and mono-energetic ones are considered. In both cases a substantial number of electrons with energies higher than 20 MeV is presented. An influence of electrons with energies lower than 20 MeV, for the electron distribution in Fig. 3.15 d) can be resolved only by means of the last crystal. Additionally, as shown in the method of the spectral analysis of Fig. 3.15, the information about the electron spectrum is taken from the signal ratios from each crystal; this gives a nice possibility to define the upper energy level of the main part of the detected electrons. Depending on the measured runaway electron spectra, both their production mechanism and the following transport of the superthermal electrons in the plasma facing materials can be obtained.

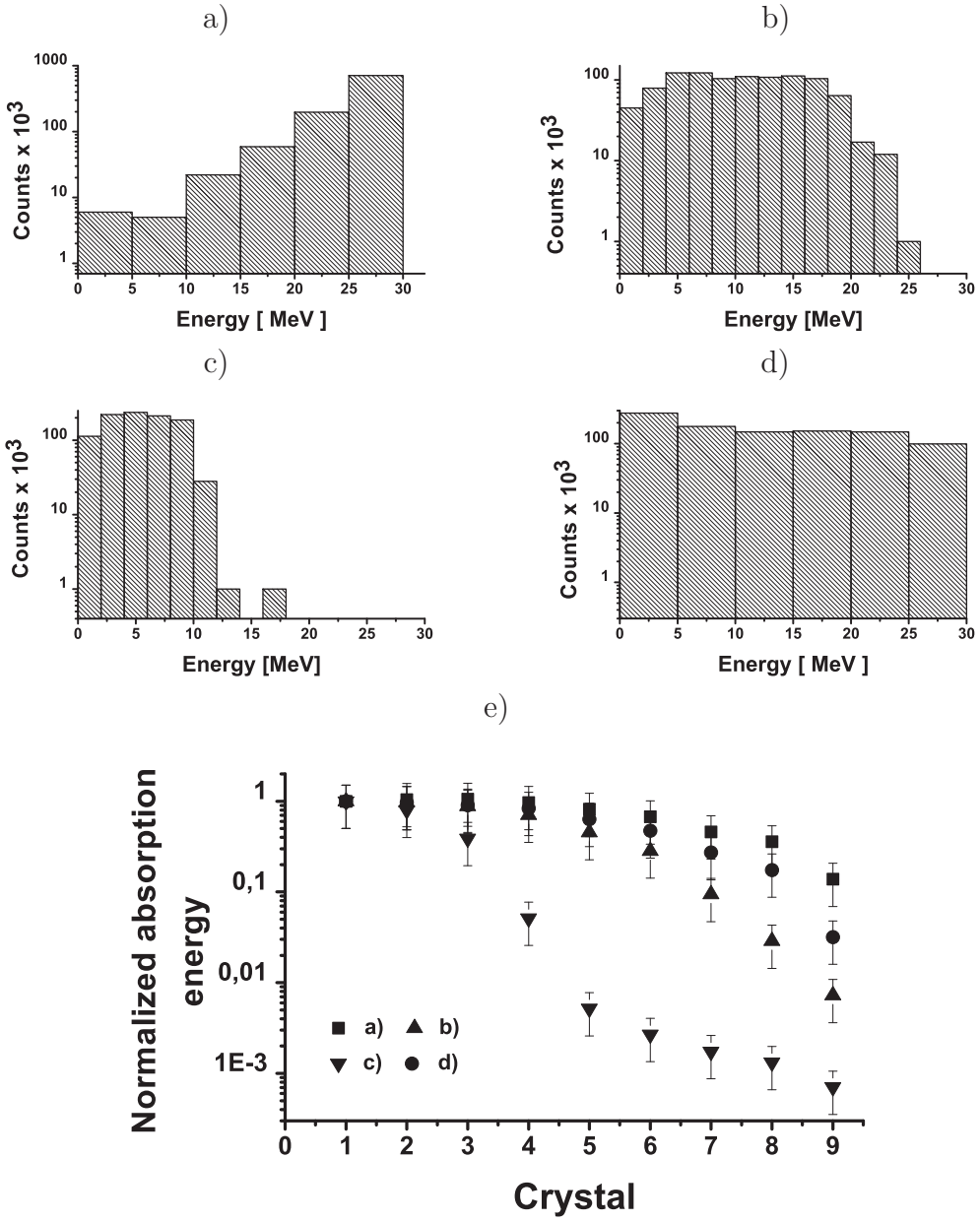

Figure 3.15: *Geant4 simulations of the absorbed energies by each crystal of the probe for different electron distributions. The absorbed energies are normalized to the energy absorbed in the first crystal. Total number of electrons incident on the probe is* 10^6 *(App. A). Maximum electron numbers: a) between 20 and 30 MeV; b) between 0 and 20 MeV; c) between 0 and 10 MeV; d) between 0 and 30 MeV; e) the normalized absorbed energy (equivalent to the signal ratios of the probe) for three different energy ranges with the maximum electron densities.*

3.2.3 Bremsstrahlung, neutron flux

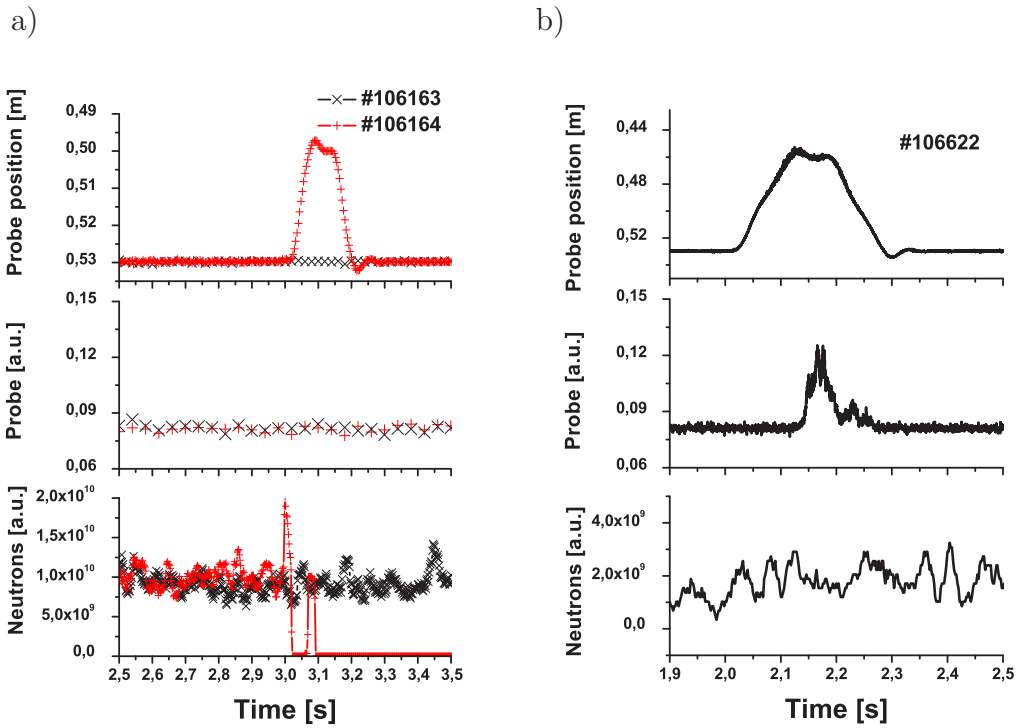

Figure 3.16: *Test of the crystal sensitivity to the neutron flux coming from the plasma. a) No runaway discharges with neutron beam injections (NBI), a high flux of neutrons are produced. The probe was placed at 50 and 53 cm minor radial positions; b) Runaway discharge, the probe was inserted to 46 cm.*

Special investigations were performed whether the runaway signal is disturbed by bremsstrahlung or neutrons ((γ, n) photo-nuclear reactions) created by the impact of the runaway electrons with the walls. Since this radiation is diffuse inside TEXTOR, it should contribute to the signal independent of its position. At a minor radius of 49 cm the probe does not show any increase of the signal. This indicates that this background can be neglected. In addition, discharges were performed with neutron beam injections (NBI) where a big flux of neutrons impinged on the probe, see Fig. 3.16 a). It was found that the YSO crystals are not sensitive to these neutrons. Signals registered by the neutron detectors were one order of magnitude higher for the NBI discharges than for the runaway ones, see Fig. 3.16 b). There are no signal changes from the noise level in the probe measurements during NBI discharges, while during a runaway discharge with lower neutron flux the probe can detect electron

which causes considerable increase of the probe signal.

3.2.4 Heat limit

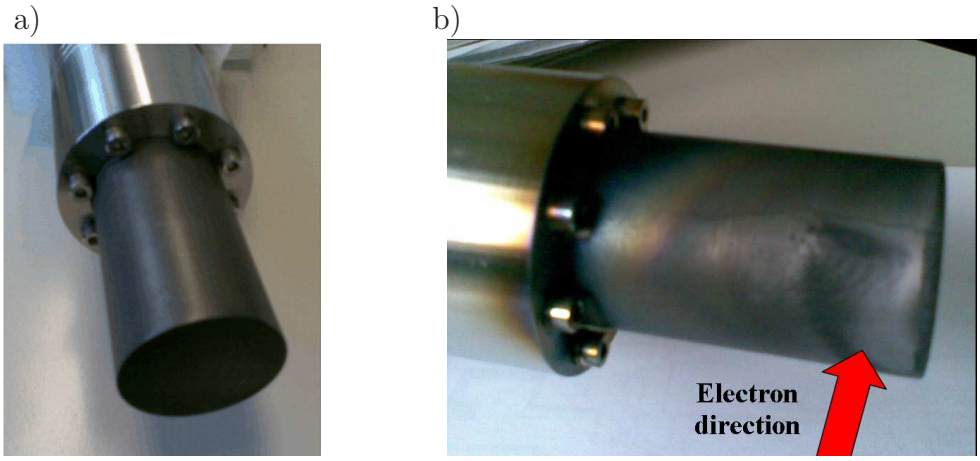

Figure 3.17: *a) The second probe before insertion into the plasma; b) The probe after experiments, the probe was inserted 2 cm into the plasma with an insertion time of about 50 ms.*

The new diagnostic has the advantage that - beside the direct measurement of the runaway electrons - the local interaction of runaways with materials can be investigated. The time interval of the measurement and the radial penetration depth of the probe into the plasma are limited by the heat flux of the thermal and of the runaway electrons. The destruction limit of the probe is 2 cm inside the last closed field surface (LCFS) at 50 ms exposure time. Simple simulations of the energy loaded on the graphite part of the probe can be made under certain conditions: an active cross section of the probe $S = 6 \cdot 10^{-4}\ m^2$, thickness $d = 0.005$ m. Electrons with energies of 3-30 MeV lost about $E_{abs} \approx 2.5$ MeV in the graphite part. The number of runaway electrons at the plasma edge $n_r = 10^{14}(1 - 0.45/0.46)^{1.5} \approx 3 \cdot 10^{11}\ m^{-3}$ in the TEXTOR tokamak [58], thus the energy deposited on the graphite part during $\triangle t = 50$ ms can be estimated as, $E_{dep} = n_r Sc \triangle t E_{abs} \approx 1$ kJ, which already can cause some damages to the graphite housing. The energy load on the graphite housing for the same plasma conditions ($n_e = 0.7 \cdot 10^{19}\ m^{-3}$), due to the ion and thermal electron transport, is about one order of magnitude less than due to the runaway electron transport. On the other hand, 1 cm outside of the

LCFS the probe can be used during the whole discharge, without damage. In Fig. 3.17 the probe before and after the measurements is shown. The probe was inserted 2 cm into the plasma with an insertion time of about 50 ms.

3.2.5 Limiter effect

For all probes inserted into the plasma edge it has to be investigated whether they disturb the plasma substantially or not. A "substantial disturber" would act as a limiter. The probe has a poloidal width of 3 cm which is about 1/100 of the poloidal circumference. Therefore the free path L_r of the guiding center of the runaway electrons between two intersections with the probe amounts to $L_r = 100 \cdot 2\pi R \approx 1000$.

The radial displacement of the runaways by the diffusion into a scrape-off layer assuming a connection length of $L = L_r$ is given by $\lambda_r^2 = D_r \cdot L_r/c \leq 10^{-2} \cdot 1000/3 \cdot 10^8 \approx 3.3 \cdot 10^{-8}$ m [100], where $D_r = 0.01\ m^2 s^{-1}$ [20]. Therefore $\lambda_r \leq 0.2$ mm. This estimate shows that the diffusion cannot fill the channel in which the guiding center of the runaways flow to the probe target, or with other words, the probe is a strong distributer and acts as a limiter. Considering the small number of λ_r one wonders at a first glance that the probe can detect runaway electrons at all. The reason for this is the relative large Larmor radius of the runaways which amounts to about $\rho_l = \gamma m_e v_\perp / eB_t \approx 5$ mm. Here $\gamma = 50$ is the relativistic factor, magnetic field B_t is chosen to be 2 T , $v_\perp = c \cdot \theta$ and $\theta = 0.1$ is the pitch angle of runaways electrons, which was previously measured in [29, 58]. Therefore, it is expected that runaways propagate radially up to 1 cm beyond the tip of the probe.

3.3 Synchrotron radiation

In 1990 a new technique to study runaway electrons inside the plasma was described in [29] by Finken. Detailed descriptions of the synchrotron method and experimental results are given in [20, 29, 58, 59].

Measurements of the synchrotron radiation emitted in the tangential direction to the magnetic field curvature with a divergence angle $\theta = (8-9) \cdot 10^{-2}$ and detected by an IR-camera were carried out in the TEXTOR tokamak. The IR-camera allows to detect the synchrotron radiation with wavelengths

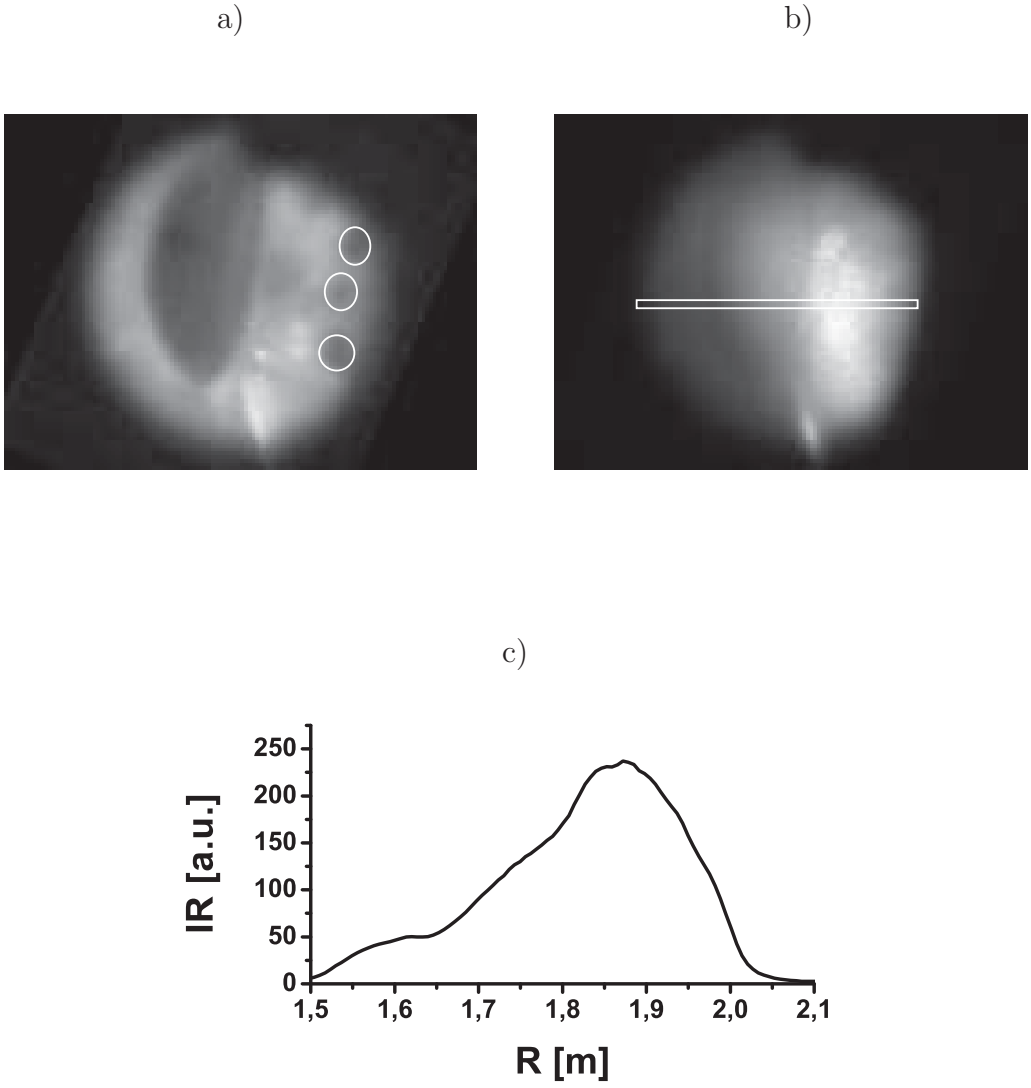

Figure 3.18: *IR-camera view in the TEXTOR tokamak. a) The measured frame made at the beginning of the discharge before runaways with energies of about 25 MeV are appearing. Three holes in the liner from the low field side indicated by white circles are used for calibrations; b) The picture made at the end of the discharge with the synchrotron radiation from runaways. A narrow slit box is defined for the radiation profile analysis; c) The radial profile obtained from the narrow slit box.*

between 3 μm and 5 μm, which correspond to the energy of electrons of about 25 MeV. The IR-camera, recording the synchrotron radiation, yields spatially and temporally (1 kHz) resolved measurements of runaway electrons between 1.5 m and 2.1 m of the major radius inside the plasma. In Fig. 3.18 a) a picture made before the synchrotron radiation can be detected from runaway electrons. Three holes in the liner (circles) can be observed clearly. Position of holes in the liner are used to calibrate the IR pictures of the synchrotron radiation projections. The synchrotron radiation including a thermal background from the limiter, liner or RF antennas detected by the camera are shown in Fig. 3.18 b). An application of the narrow slit box provides an information about synchrotron radiation profiles. The resulting radiation profile obtained from the defined box in Fig. 3.18 b) is shown in Fig. 3.18 c).

The measured intensity of the radiation depends on the number of runaway electrons and their energy distribution. In [58] an analysis of the measured intensity was done under the assumption of a mono-energetic distribution, which is justified within an error of 15%. In the case of a mono-energetic distribution, the measured intensity is proportional to the total runaway density n_r.

The number of runaways N_r, detected from the observed synchrotron radiation is calculated from [29, 58]:

$$\mathbf{N_r} \int \frac{\mathbf{dP}}{\mathbf{d}\lambda} \mathbf{T}(\lambda) \mathbf{d}\lambda = \mathbf{A\Omega} \int \mathbf{L}_\lambda^\mathbf{s} \mathbf{T}(\lambda) \mathbf{d}\lambda, \tag{3.2}$$

where A is the cross-sectional area of the ring filled with runaways, $\Omega = 2\pi \cdot 2\Theta$ is the solid angle into which the synchrotron radiation is emitted, Θ is the pitch angle of the runaways, L_λ^s is the measured spectral radiance, and $T(\lambda)$ is the transmission function of the optical system. $P_\lambda = N_r^{-1} \int P_\lambda^e f(E) dE$, where P_λ^e is the synchrotron radiation emitted by one electron, and f(E) is the energy distribution function. Due to the uncertainty in the exact energy distribution, the absolute number of runaway electrons can be estimated within an order of magnitude. The estimated absolute number of runaways from the measured synchrotron radiation, in [58], was about of $2 \cdot 10^{14}$.

3.4 Other runaway diagnostics

In the TEXTOR tokamak besides of the two described above powerful diagnostics (the scanning probe and the IR-camera) other diagnostics can provide some information about runaways.

- *X-ray (γ) measurements.* As soon as runaway electrons are lost from the plasma and hit the carbon limiter or the vessel structures, they produce x-ray (γ) radiation. Part of this radiation can cause neutron productions due to the photo-nuclear reaction $(\gamma; n)$ [25, 26].

- *Neutron detectors.* Four neutron detectors are used with different sensitivities. Neutrons produced in $(\gamma; n)$ photo-nuclear reactions due to interactions of runaway electrons with the plasma facing materials. The minimum required energy of runaway electrons is about 10 MeV, which is defined by the threshold of the $(\gamma; n)$ reaction.

- *Electron cyclotron emission (ECE).* ECE is used on many tokamaks for the electron temperature measurements. In the presence of the runaway electrons an enhancement of the ECE signal was observed in [36]. However, ECE measurements of runaway electrons are less qualitative than other discussed above diagnostics, because of the competition between the superthermal electron emission and the reabsorption in the optically thick plasma.

Chapter 4

Spectrally, temporally and spatially resolved measurements of runaway electrons

4.1 Spatially and temporally resolved measurements of runaway electrons at the plasma edge

4.1.1 Radial profile of runaways at the plasma edge

The first and the second probe were used for the determination of the radial decay of the runaway density at the edge and in the scrape-off layer of the plasma. In the scanning mode the insertion of the first probe starts 3.4 s after the beginning of the discharge with an insertion time of 0.5 s. The probe remains at the innermost position for 0.1 s and then it is withdrawn within 0.5 s. A signal from the first probe as a function of the crystal position is shown in Fig. 4.1. The crystal is placed at 45.5 cm minor radial position. The Last Closed Flux Surface (LCFS) is defined by a carbon limiter and amounts to 46 cm; hence the measurements are carried out up to 0.5 cm inside the plasma. Similar measurements of runaway electrons by using the second probe were performed. The probe is inserted at 3.1 s after the beginning of the discharge with a velocity of 0.7 s into the plasma with the crystal positions at

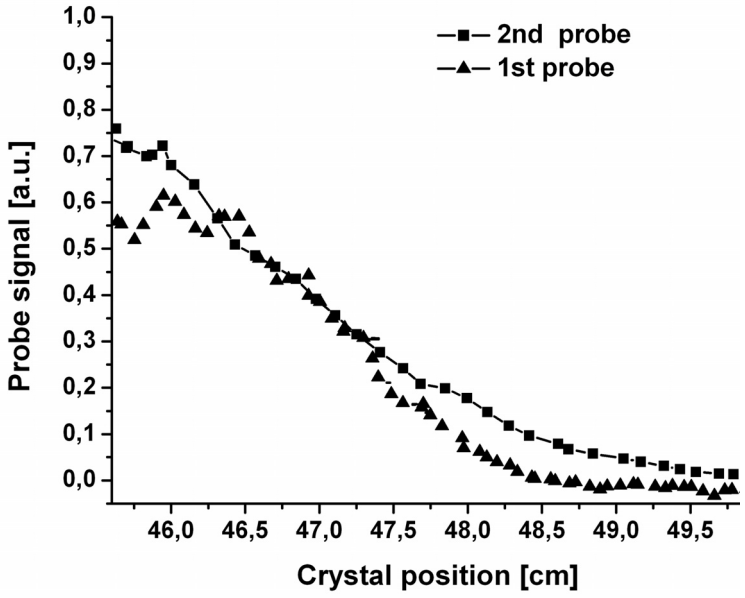

Figure 4.1: *Measurements of runaway electrons between 53 cm and 45 cm of the minor radius by the both scanning probe. Electrons with energies $E > 2.5$ MeV were registered by the first probe. In the second probe signals from the first crystal are presented, electrons with energies, $E > 5$ MeV, were registered.*

45.5 cm. The signals in Fig. 4.1 from the first crystal show the electrons with energies higher than 5 MeV. The steep rise of the signal demonstrates a rapid increase of the runaway electron population starting at the 48.5 cm minor radial position. In spite of different sensitivities and spatial resolutions of the probes, a good correlation between both measurements can be observed.

Open field lines at minor radial positions higher than 46 cm can be responsible for the strong runaways loss that causes the exponential decay of the runaway electron populations between 46 cm and 48.5 cm.

4.1.2 Temporal evolution of runaways at the plasma edge

A temporal profile of runaway electrons was measured by means of the third probe. The probe was placed at 47 cm radial position at 1.2 s for 1 s, as shown in Fig. 4.2 a). All channels of the probe demonstrate the same trend: the rapid growth of the signal in time. In Fig. 4.2 b) raw signals for crystals 1; 5 and 9 are shown. In the low density plasma discharge, electrons are produced

during the start up of the discharge due to the Dreicer mechanism and after 1 s the production of runaways is mainly defined by the avalanche processes [58]. Therefore the number of runaways grows rapidly in time after 1 s.

A more detailed look, in Fig. 4.3, to the measured signal demonstrates oscillations of the signal for each channel. The probe signals oscillate in the same phase and frequency as the horizontal plasma position imposed by the TEXTOR position feedback system. An inward motion of the plasma corresponds to reduction of the probe signal and vice versa. This result is in good agreement with the measured radial profile of the runaway beam at the plasma edge, Fig. 4.1, where the rapid growth of the signal to the LCFS was measured.

An analysis of runaway spectra at different phases of the signal oscillation demonstrates that the electron spectrum does not change on the plasma position as soon as electrons leave the closed field lines. In Fig. 4.4 signal ratios and the corresponding spectrum are shown for different phase of the signal oscillation.

The indifference of the runaway electron spectrum on the radial profile and the substantial reduction of the probe signal with the radial position (for $r > a$) indicates the strong non-collisional scattering of the runaway flux coming from the plasma.

The conservation of the runaway spectrum on the radial profile at the plasma edge provides a possibility to judge the energy distribution of runaway electrons coming to the limiter surface or plasma facing materials independently on the exact position of the probe close to $r = a$ surface.

4.2 Production of runaways at different densities

It is well known that the production of runaways according to the Dreicer model depends strongly on the electron density. Therefore a set of discharges was performed in which the electron density was systematically increased from discharge to discharge; within the discharge, the density was kept constant. The runaway density was measured at 2.1 s after the beginning of the discharge by using synchrotron radiation and probe measurements of runaways. In this series probe #2 was used which allows a discrimination of the runaway energy.

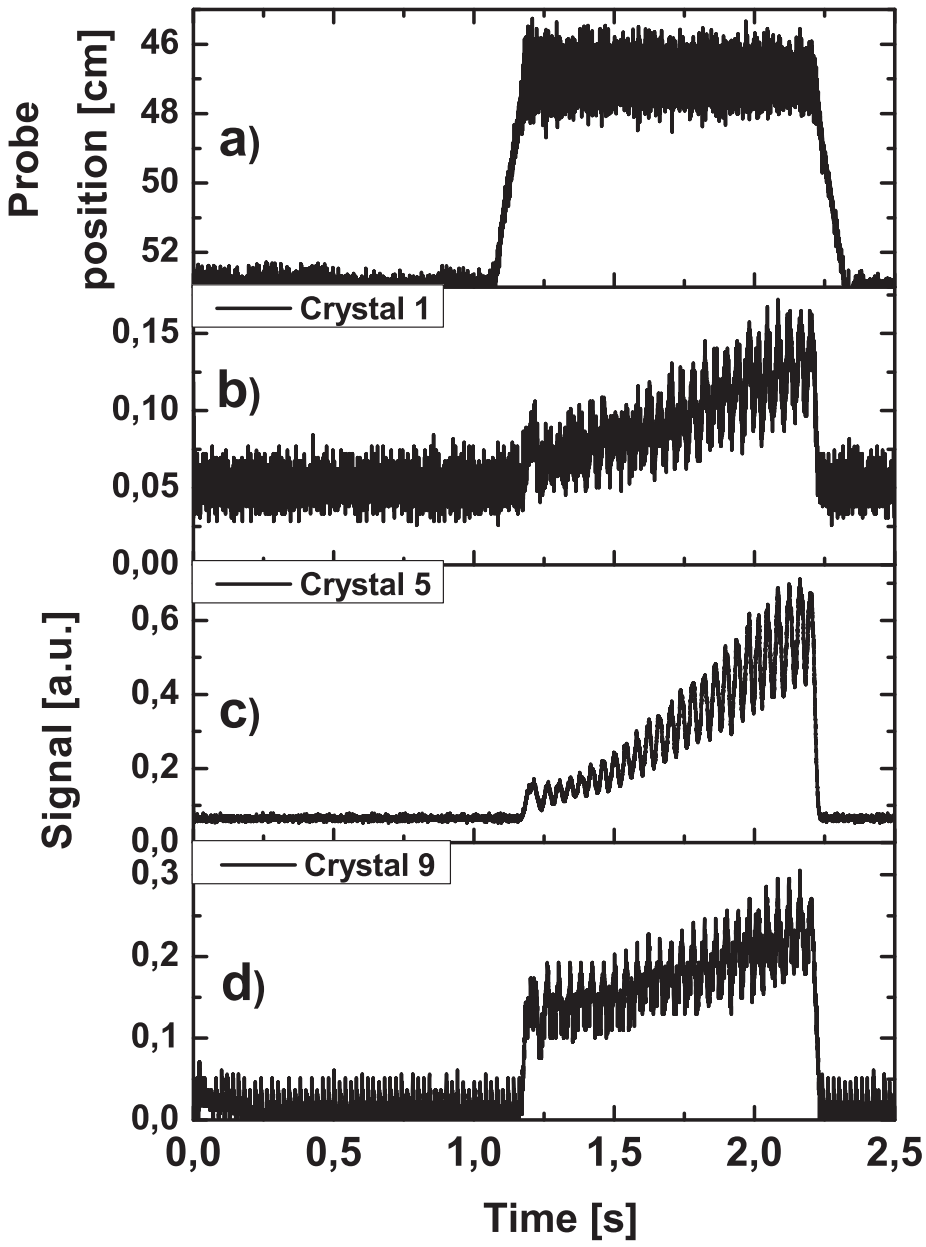

Figure 4.2: *Measurements of runaway electrons between 1.2 and 2.2 s by the third scanning probe. a) Probe position. Probe signals. b) The 1st crystal; c) The 5th crystal; d) The 9th crystal.*

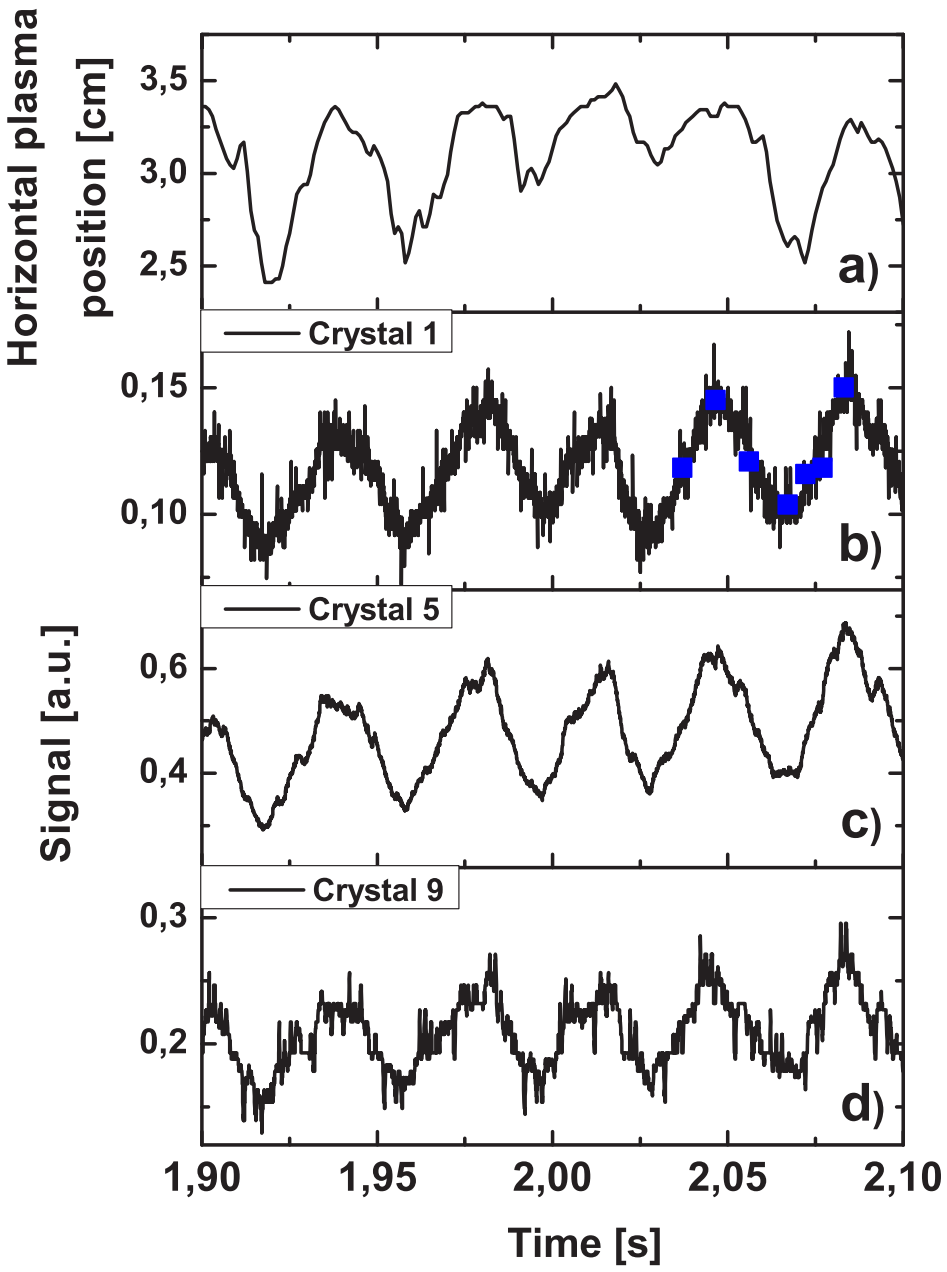

Figure 4.3: *a) Horizontal plasma position. Oscillations of the probe signals. b) For the 1st crystal; c) 5th crystal; and d) 9th crystal. Blue points (the second figure from the top) show the oscillation phase, where the runaway spectrum is analyzed.*

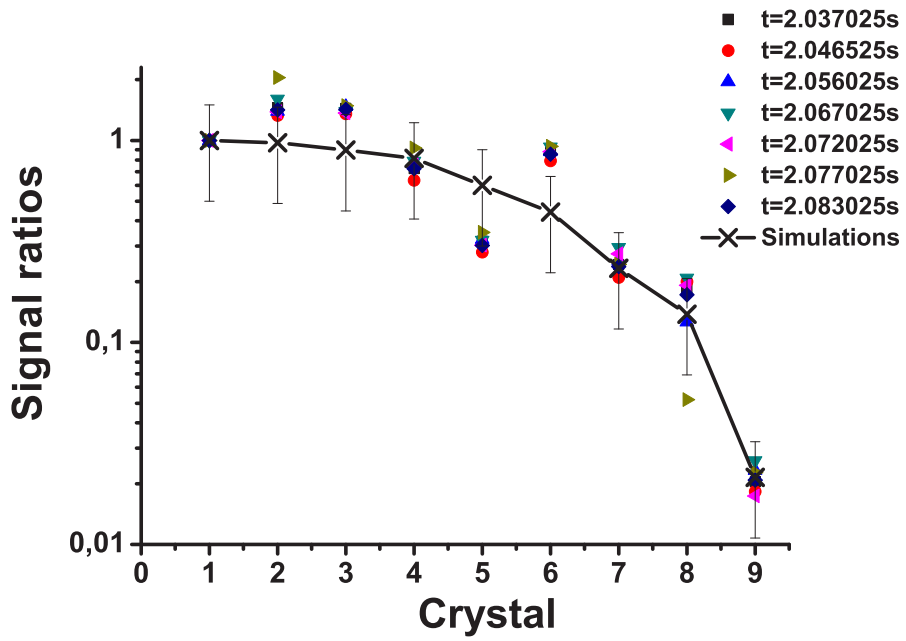

a)

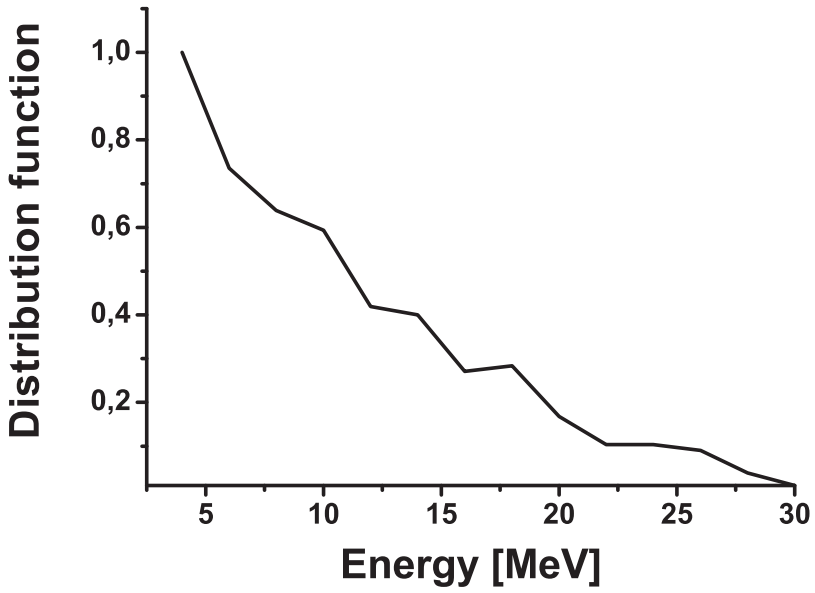

b)

Figure 4.4: *a) Signal ratios measured at different phases of the oscillation. The oscillation phase corresponds to the proper time during the discharge. The signal is normalized to the signal from the first crystal. The spectrum corresponding to the measured signal ratios is simulated by means of Geant4 code. The normalized absorption energy by each crystal to the first one is shown for the simulated spectrum. b) The spectrum of the detected runaway electrons.*

Fig. 4.5a) and b) show the synchrotron data together with time traces of the probe channels for energies higher than 8; 16 and 25 MeV. The number of runaways reduces by one order of magnitude when the density grows by a factor of two. The synchrotron radiation is in good agreement with the probe signals; perhaps it falls slightly stronger than for the probe channel measured in the same energy range of electrons.

The reduction of the number of runaways with increasing densities can be

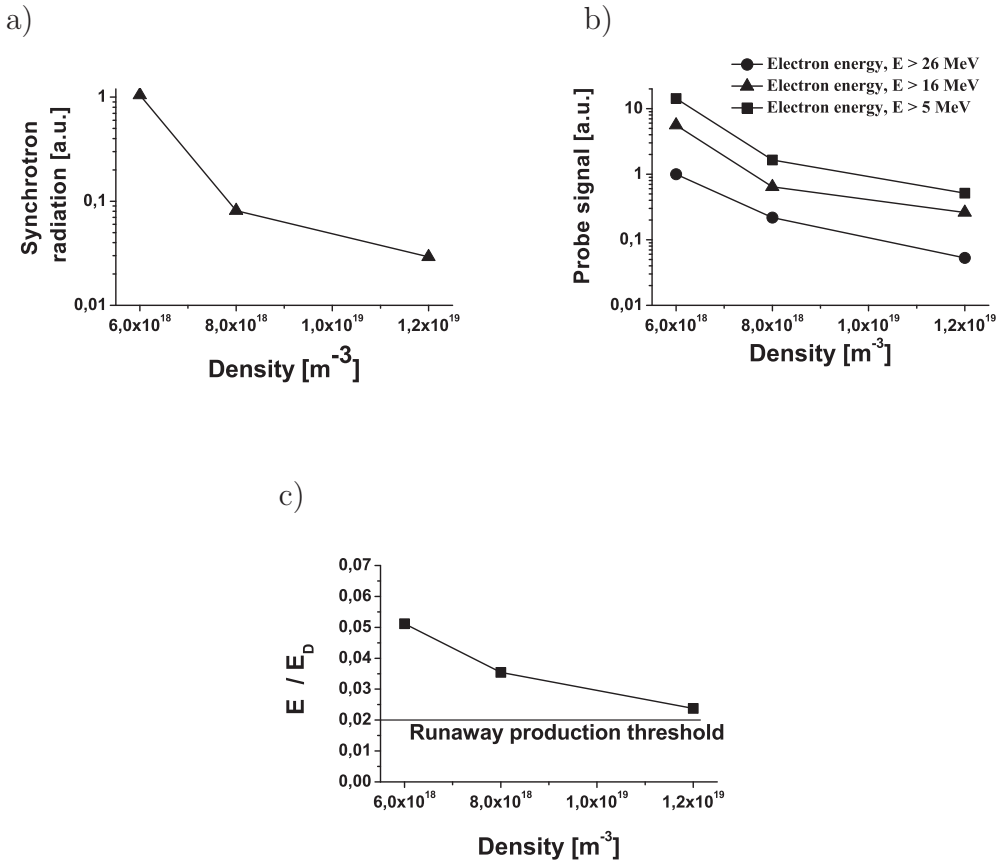

Figure 4.5: *a) Synchrotron radiation and probe measurements of runaway electrons with energies higher than 25 MeV at 2.15 s into the discharge; b) The probe measurements of runaway electrons with electron energies higher than 5 MeV and 16 MeV. The probe was placed at the last closed flux surface (LCFS) at 2.15 s during the discharge. c) Ratio of the electric field to the Dreicer field.*

explained by the suppression of primary generated electrons. The production rate of primary generated electrons is an exponential function on $E_{\parallel}/E_c$ [45,

46, 47, 64] and is given as:

$$\dot{n}_r^{pr} = \frac{n_e}{\tau}\left(\frac{m_e c^2}{2T_e}\right)^{3/2}\left(\frac{E_c}{E_\parallel}\right)^{3/8}\exp\left(-\frac{E_c}{4E_\parallel}-\sqrt{\frac{2E_c}{E_\parallel}}\right), \tag{4.1}$$

where $\tau = 4\pi\epsilon_0^2 m_e^2 c^3/n_e e^4 \ln\Lambda$ is the relativistic electron collision time, $E_\parallel$ is the parallel electric field and $E_c = n_e e^3 \ln\Lambda/4\pi\epsilon_0^2 m_e c^2$ the critical electric field. Hence the increasing density causes the increase of E_c and as a consequence the reduction of $\dot{n}_r^{pr}$. Although the production rate of secondary generated electrons does not depend explicitly on the plasma density [51, 90], nevertheless the reduction of $\dot{n}_r^{pr}$ leads to a decrease of n_r and the whole suppression of the runaway electron production, as seen in:

$$\dot{n}_r^{sec} \simeq n_r\left(\frac{\pi}{2}\right)^{1/2}\frac{E_\parallel/E_c - 1}{3\tau\ln\Lambda}. \tag{4.2}$$

Estimates of the ratio of the electric field to the Dreicer field, $E_D = m_e c^2 E_c/T_e$, for corresponding densities, with the following other parameters: $\ln\Lambda = 16$, $T_e = 1.5\ keV$ [57], are shown in Fig. 4.2 c). At $n_e = 1.2\cdot 10^{19}\ m^{-3}$ the value $E_\parallel/E_D = 0.25$ which corresponds to the threshold of the runaway electron production [51] below which almost no runaway production occurs. At this value the number of runaways registered by both diagnostics was close to zero and one order of magnitude smaller than at $n_e = 0.7\cdot 10^{19}\ m^{-3}$.

Chapter 5

Measurements of the diffusion coefficient at different magnetic fields

5.1 Introduction

In the present tokamaks the production of runaway electrons depends strongly on the density [64], the electric field [64, 90], the effective charge of ions (Z_{eff}) [82] and the magnetic field [44, 71, 89, 105]. Here the dependence on the magnetic field is of primary interest. It has been found that only few runaways are observed below a magnetic field of 2 T. An interesting observation is reported by Yoshino [105] namely that increasing magnetic perturbations can reduce the number of runaway electrons. Therefore, magnetic perturbations are considered to be a mechanism, for runaway electron suppression during disruptions [50, 72, 106].

Runaway electrons can be regarded as effectively collisionless and are not very sensitive to electrostatic fluctuations; this makes them a suitable probe to study magnetic turbulence [20, 22]. The diffusion due to the electrostatic turbulence scales with v^{-1}, v is the electron velocity, while the diffusion defined by the magnetic turbulence scales as v. For a particular experimental condition, measurements of magnetic fluctuations by means of the runaway probe was previously performed in the TEXTOR tokamak, making use of the synchrotron emission [20, 22]. In this method, synchrotron emission produced

by runaway electrons with energies above 25 MeV was used to diagnose the magnetic perturbation level at $B_t = 2.25\ T$ during low density plasma discharges [22].

The present chapter investigates the following issues: first, whether the dependence of the disruption generated runaway electrons on the B_t holds in a similar way as for runaways created under better controlled conditions in quasi stationary, low density discharges, the relation of the number of runaways to the radial transport coefficient and in addition, the dependencies of the radial transport coefficient and the magnetic perturbation level δB on B_t and I_p. In particular for the transport based on turbulent magnetic fields almost no information is available. In our opinion, the investigation of the magnetic fluctuations as a function of B_t is a generic property and not only limited to low density discharges. During the measurements, B_t was varied between $1.9\ T \leq B_t \leq 2.7\ T$ and two different plasma currents $I_p = 300\ kA$ and $I_p = 400\ kA$ were used.

5.2 Measurements

Measurements of runaway electrons were performed in the TEXTOR tokamak. The tokamak has the following parameters: major radius $R = 1.75\ m$ and minor radius $a = 0.46\ m$. The discharge is an ohmic low density discharge (typically $n_e < 10^{19}\ m^{-3}$) in which runaway electrons are generated during the whole discharge. The number of runaway electrons in such a low density discharge depends on the generation (primary and secondary generation [17, 47, 64, 95, 90]) and on their loss mainly due to magnetic perturbation. The primary generation of the runaways depends strongly on the ratio of the electric field E to a critical electric field E_c (Dreicer field) E/E_{crit}, where $E_{crit} = e^3 n_e \ln\Lambda/(4\pi\epsilon_0^2 T_e)$ [64], i.e. it varies critically on the chosen electron density as the external parameter. During the start-up phase of the discharge, i.e. for $t < 1\ s$, the loop voltage is rather high and the primary generation dominates while in the flat top part of the discharge the secondary generation is more important. The electron density is not a free parameter as in normal discharges because the density is mostly defined by the balance of gas release due to impinging energetic plasma particles on the wall and wall pumping.

Therefore, a very careful conditioning is required and the measurements were started after the reproducibility of the B_t dependence was established. After the conditioning, the variation of B_t does not cause a significant variation of the electron density. However, the change from 300 to 400 kA plasma current increases the density because the impinging plasma particles have a different energy, as also the loop voltage changes as well, the combined effects on the runaway generation nearly cancel each other.

Two different diagnostics have been used to measure runaway electrons: synchrotron radiation observed by an IR-camera [29] and neutron detectors. The IR-camera, recording the synchrotron radiation, yields spatially and temporally (1 kHz) resolved measurements of runaway electrons with energies above 25 MeV between 1.5 m and 2.1 m of the major radius inside the plasma. Neutron detectors measure runaway electrons outside the plasma. Electrons registered by the detectors have energies higher than 10 MeV, as defined by photo-nuclear (γ, n) reaction threshold.

5.3 Experimental results

Fig. 5.1 shows runaway electron measurements at different toroidal magnetic fields and for two different plasma currents by the synchrotron radiation and neutron detectors. In the analysis of the synchrotron radiation, the measured signal during the discharge with B_t of 1.9 T, where almost no runaways were detected, is taken as a thermal background level. Both diagnostics: synchrotron radiation and neutron detection showed a similar trend of the increasing amount of runaway electrons with B_t. Possibly the runaway number decreases again above the highest value of B_t of around 2.5 to 2.6 T. Even though the maximum is found in both B_t scans, we are not able to study the trend of the population of runaway electrons to higher magnetic fields further, because the magnetic field B_t of 2.7 T is the technical limit of the TEXTOR tokamak. The runaway number for $I_p = 400\ kA$ case is slightly higher than for $I_p = 300\ kA$ which may be related to the higher loop voltage. In addition, the data indicates that the peak is shifted to higher B_t for the higher plasma current. The experiments on the low density plasma discharges in TEXTOR have shown the importance of the wall conditions. A similar trend on B_t is

also seen in disruptive discharges [71, 105] where runaway production lacks of course on the wall conditioning, as shown by the large number of analyzed disruptions on different machines.

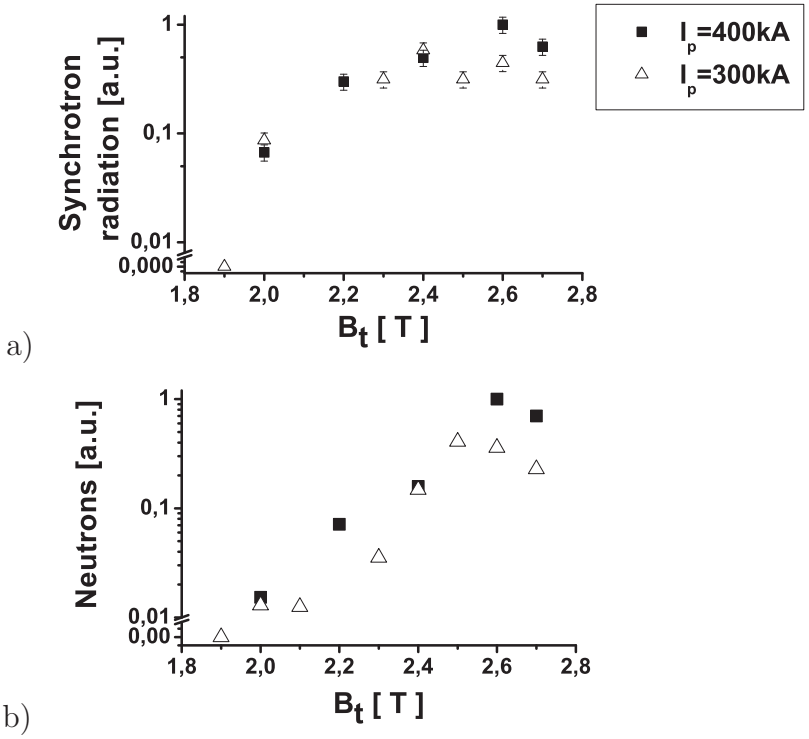

Figure 5.1: *The dependence of the number of runaway electrons on the toroidal magnetic field for plasma currents of 300 and 400 kA. a) Synchrotron radiation measurements. Thermal emission from the vessel components was removed from the synchrotron emission by subtracting a snapshot of the vessel taken during the discharge with B_t of 1.9 T with no runaway electrons (with energies above 25 MeV). b) Neutron measurements, signal averaged between 3.3 s and 4 s. Signal at 1.9 T is taken as a zero level.*

5.4 Radial transport

Detailed studies of runaway transport in ohmic plasmas were made in [20, 22]. The same method, as in [22], was used to estimate the level of the radial diffusion at different magnetic fields between 2 and 2.7 T during low density plasma discharges. More in detail the method is described in App. B. Additionally, it was taken into account that the radial profile is shifted from

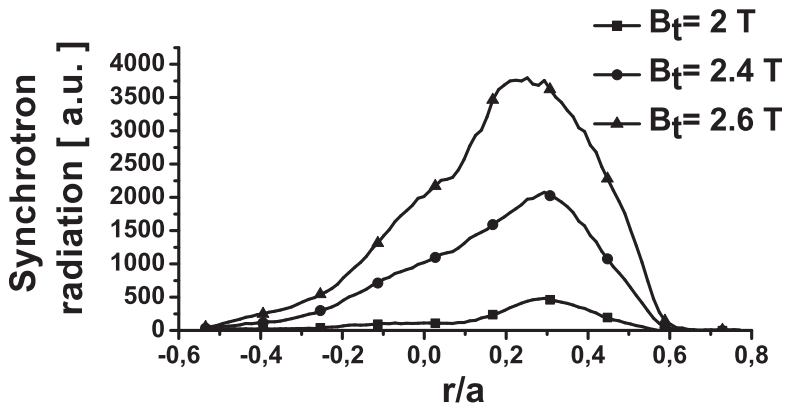

Figure 5.2: *Typical radial profile of the synchrotron radiation for B_t of 2; 2.4 and 2.6 T. An estimation of the radial diffusion coefficient has been performed at r=0.4a.*

the center of the tokamak approximately by 12 cm to the low field side, as shown in Fig 5.2 for B_t of 2; 2.4 and 2.6 T. The measured intensity of the synchrotron radiation is a measure of the runaway density under approximation of the mono-energetic distribution of runaways. Diffusion coefficients have been estimated at $r = 0.4a$ minor radius, where a parabolic profile for the safety factor q is assumed, with $q_0 = 0.8$ $(r = 0)$ and $q_a = 2\pi a^2 B_t/\mu_0 IR$ $(r = a)$ [20]. Dependencies of radial diffusion coefficients on the magnetic field are shown in Fig. 5.3 for the two different plasma currents. The radial diffusion is a rapidly decreasing function on the magnetic field. This is observed for both plasma currents. In addition, the result obtained in [22] during low density plasma discharges at a magnetic field B_t of 2.25 T and plasma current I_p of 350 kA is indicated in Fig. 5.3 by the star symbol. A diffusion level of $6 \cdot 10^{-3}$ m^2/s was reported.

5.5 Discussion

The production of runaways depends strongly on the plasma density, n_e, therefore the possible effect of the slight uncertainty in the plasma densities at different B_t on the runaway production has to be analyzed. In order to estimate the number of runaway electrons produced during the discharge, two competitive processes are considered: production of runaways (primary and secondary) and their loss due to the orbital drift. The evolution of the runaway

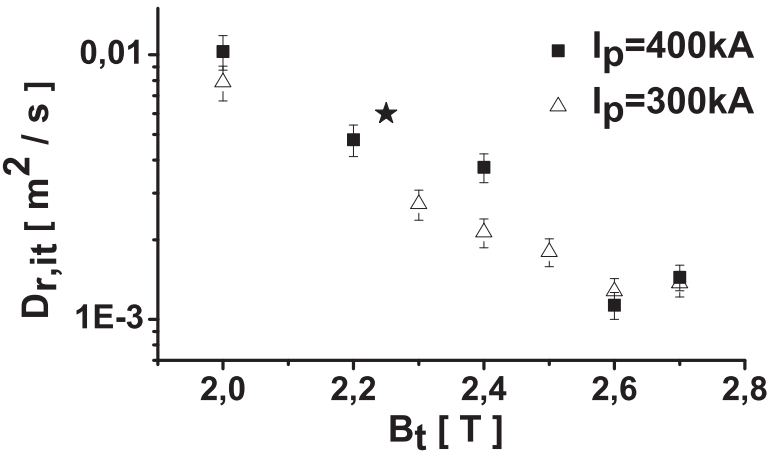

Figure 5.3: *The dependence of the diffusion coefficient on the toroidal magnetic field for plasma currents of 300 and 400 kA.* ★ *result obtained in [22, 20], with a magnetic field of* $B = 2.25$ *T and a plasma current* $I_p = 350$ *kA, at r=0.4a.*

population is given by [57]:

$$\frac{\mathbf{dn_r}}{\mathbf{dt}} = \lambda\nu_{\mathbf{e}}(\mathbf{v_{th}})\mathbf{n_e} + \frac{\mathbf{n_r}}{\mathbf{t_o}} - \frac{\mathbf{n_r}}{\tau}, \tag{5.1}$$

where λ is the production rate [64], $\nu_e(v_{th})$ is the collision frequency, n_r is runaway electron densities, $t_o = \sqrt{12}\ln\Lambda m_e c(2 + Z_{eff})/9eE$ [20], $\tau \approx a^2/5.6D_{r,it}$ [20], electric field $E = V_{loop}/L$, V_{loop} is the loop voltage, which depends slightly on B_t and I_p (typically $V_{loop} \approx 0.9$ V), $L \approx 10$ m is the length along the axis of the tokamak. Plasma density, n_e, equals $(0.8 - 0.9) \times 10^{19}$ m^{-3} for the plasma currents of 300-400 kA. The first two terms in Eq. (5.1) are responsible for the primary and secondary generation processes respectively and the third one for the loss of runaways. In Fig. 5.4 a) and 5.4 b) dependencies of the number of electrons produced due to the primary and secondary generation processes till 2.5 s after the beginning of the discharge, the number of electrons lost until the same time and the total number of electrons left in the plasma on the magnetic field are shown for both plasma currents. From previous measurements [57], a good correlation with results in Fig. 5.4 is observed, where the number of runaways was measured during a low density plasma discharge with the following plasma parameters: $B_t = 2.25$ T and $I_p = 350$ kA, also shown in Fig. 5.4 a). The reduction of runaway electrons registered by the neutron

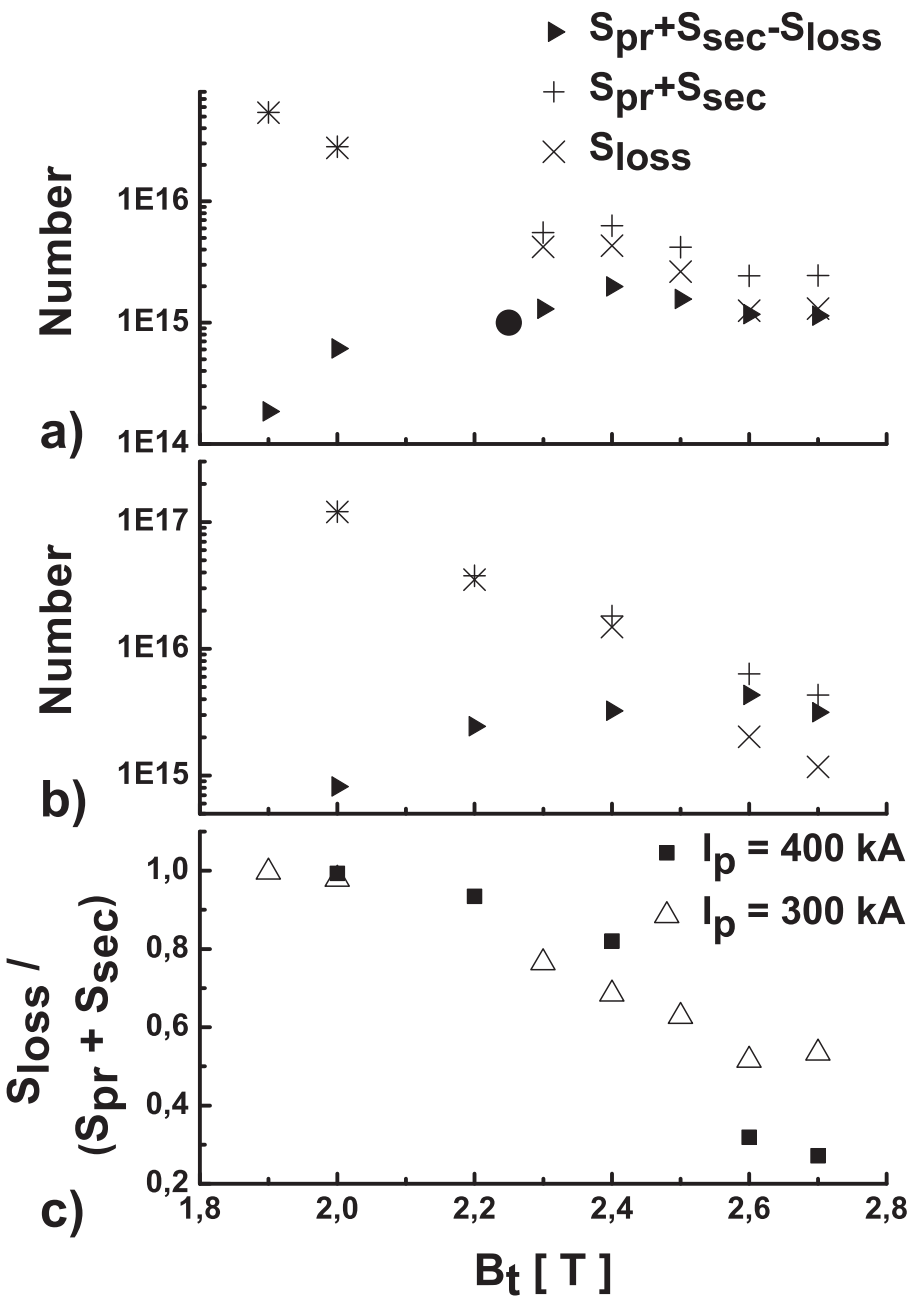

Figure 5.4: *a) Number of runaway electrons depending on the magnetic field for the plasma current of 300 kA. S_{pr} primary production, S_{sec} secondary production, S_{loss} loss of runaway electrons; b) Number of runaway electrons depending on the magnetic field for the plasma current of 400 kA. S_{pr} primary production, S_{sec} secondary production, S_{loss} loss of runaway electrons; For comparison, • number of runaway in the plasma measured in [57], with a magnetic field $B_t = 2.25$ T and a plasma current of $I_p = 350$ kA; c) Ratio of the loss of runaway electrons (S_{loss}) to the total produced runaway electrons (primary (S_{pr}) + secondary (S_{sec})).*

detector and the synchrotron radiation, in Fig. 5.1, correlates well with results obtained in Fig. 5.4 a); b), where the total number of runaways left in the plasma decreases with the magnetic field. An increase of the loss level of runaways to their production, as shown in Fig. 5.4 c), is the reason of the reduction of the total number of electrons left in the plasma with decreasing magnetic field. In Eq. (5.1) the loss rate of runaways is defined by the radial transport and is proportional to the diffusion coefficient.

In the simplest approximation, the radial diffusion is related to the mag-

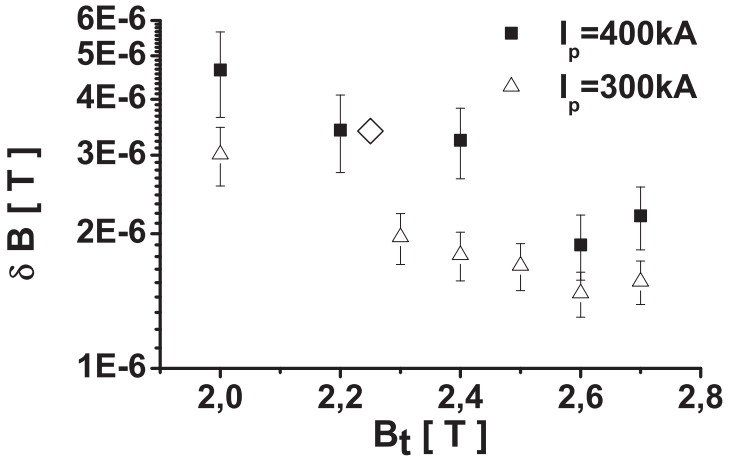

Figure 5.5: *Preliminary analysis of the dependence of the magnetic field perturbation on the toroidal magnetic field for plasma currents of 300 and 400 kA, at r=0.4a. ◇ magnetic perturbation level measured in [20, 22]. This figure will be corrected by orbit shielding effects, which are discussed in Chap. 6.*

netic perturbation level over the following expression [50, 88]:

$$\mathbf{D_{r,it}} = \pi \mathbf{q v_{\|} R} \left(\frac{\delta \mathbf{B}}{\mathbf{B_t}} \right)^{\mathbf{2}}. \tag{5.2}$$

Here δB is the magnetic fluctuation level, q is the safety factor and $v_{\|}$ is the electron velocity along the magnetic field. Results of estimations from Eq. (5.2) of the perturbation level depending on the magnetic field are shown in Fig. 5.1. A substantial growth of the magnetic fluctuations at a magnetic field of about 2 T is observed for both plasma currents. The error bars in Fig. 5.3 and 5.5, are mostly determined by the uncertainty in the definition of the radial profile, see Fig. 5.2. The quantity $\delta B/B_t$ decreases slightly steeper with B_t than δB.

A fluctuation of the magnetic level at B_t of 2.25 T was estimated from the radial diffusion measured in [20, 22] and it was about $3.4 \cdot 10^{-5}$ T, as shown in Fig. 5.5.

The analysis is incomplete; an effective shielding of the magnetic structures by orbits of the runaways will be discussed in Chap. 6. There also the revised data of the magnetic fluctuation level will be presented.

In comparison with results published in [72], where external magnetic perturbations were applied during plasma disruptions and as a consequence the suppression of the runaway current was observed. In the present chapter it has been shown that the reduction of the magnetic field leads to the natural growth of the magnetic fluctuation level in the plasma and as as consequence to the remarkable reduction of runaway electrons over their radial transport.

The rise of the magnetic perturbations could be also the reason for the reduction of runaway electron production at a magnetic field lower than 2 T during plasma disruptions [44, 71, 105].

Chapter 6

Spectrally resolved measurements of runaways at different toroidal magnetic fields

6.1 Introduction

In the previous chapter, it has been shown that the number of runaway electrons detected by the synchrotron radiation and neutron detectors decreases for low B_t. This effect has been explained by the increase of the radial transport as a result of the growth of the magnetic fluctuation level. In the present section, a detailed analysis of runaway electrons coming from the plasma due to the radial transport is investigated. For that spectrally resolved measurements of runaways were performed at the plasma edge at different toroidal magnetic fields, B_t. Experiments were carried out during low density plasma discharges.

6.2 Set-up

Two diagnostics were used to study runaway electrons in the present experimental campaign. The first one is the absolutely calibrated scanning probe, which provides direct measurements of runaway electrons and their spectrum at the plasma edge, as shown in Fig. 4.1, Chap. 3. The probe was inserted to 47 cm minor radial position (low field side) three times during the discharge at

1 s; 2 s and 3 s. The last closed flux surface (LCFS) is defined by the carbon limiter position, which is placed at r=a (a=46 cm). Electrons with energies between 4 and 30 MeV can be resolved by the probe. The second diagnostic are four neutron detectors, which measure runaway electrons outside the plasma. Electrons registered by the detectors have energies higher than 10 MeV, as defined by the photo-nuclear (γ, n) reaction threshold.

The production of runaway electrons depends strongly on the plasma

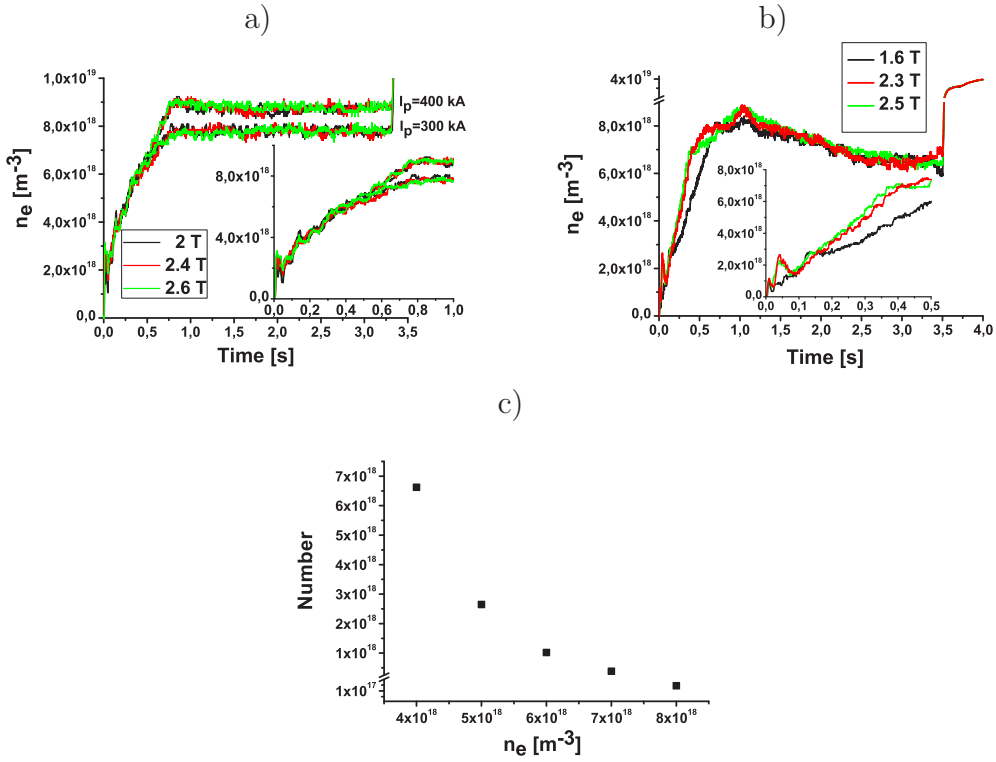

Figure 6.1: *a) Plasma density measured during the experiment campaign in Chap. 5 for plasma current of 300 and 400 kA . b) Plasma density in the present experimental campaign, plasma current of 400 kA. c) The total electron number depending on the density after one second of the discharge. The number is estimated from the approximation* ($\frac{dn_r}{dt} = \lambda\nu_e(v_{th})n_e + \frac{n_r}{t_o} - \frac{n_r}{\tau}$) *described in Chap. 5.*

parameters, like plasma density and loop voltage. Therefore very careful conditioning is required to measure the runaway number at different B_t. In the present experimental campaign, as well as in Chap. 5, the plasma density is measured by the HCN-interferometer. Nevertheless, due to technical restrictions during these experiments, the plasma position was measured by mag-

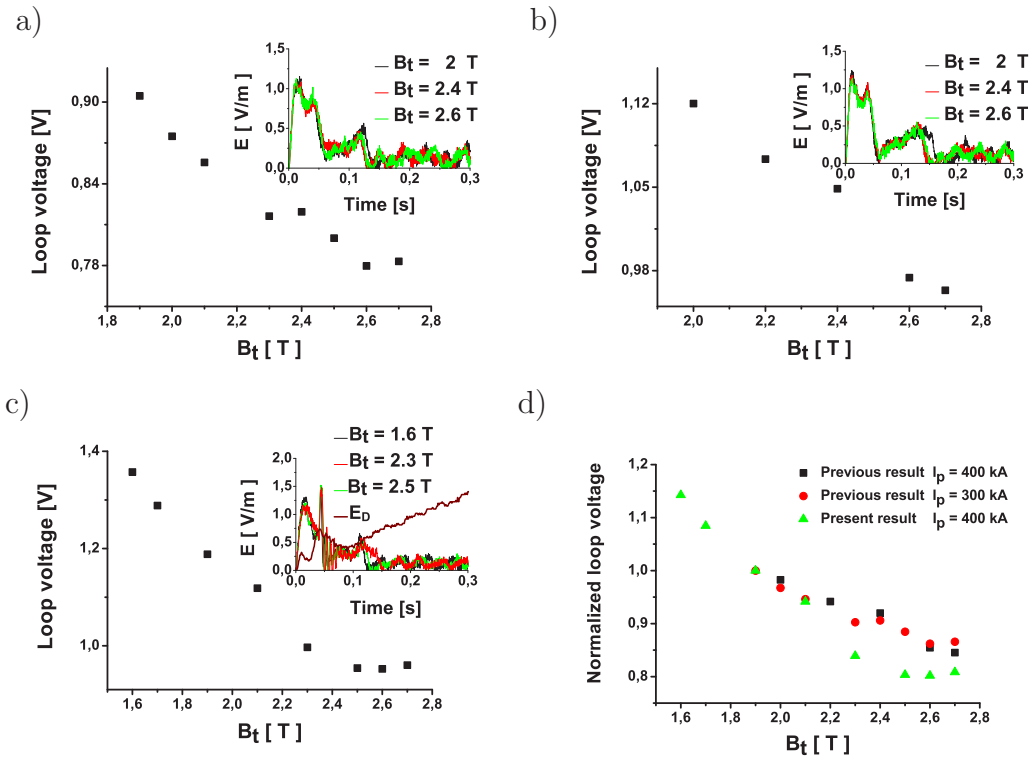

Figure 6.2: *Loop voltage was averaged between 0.5 and 3 s during the discharge. Additionally, the electric field strength at different B_t during the first 0.3 s of the discharge are shown in cases a)-c). The comparison of the electric field with the Dreicer field ($E_D = e^3 n_e \ln\Lambda/(4\pi\epsilon_0^2 T_e)$) is done in case c). a) Loop voltage measured during the experimental campaign in Chap. 5 for a plasma current of 300 kA . b) Loop voltage measured during the experimental campaign in Chap. 5 for a plasma current of 400 kA. c) Loop voltage in the present experimental campaign, a plasma current of 400 kA. d) Comparison of loop voltages for both campaigns.*

netic coils instead of the HCN-interferometer. Even though many tokamaks use magnetic positioning, the interferometric system is superior at least at TEXTOR. Therefore, in the present measurements the density is not as reproducible as it was in Chap. 5. In addition, it was not able to perform such a careful conditioning as mentioned previously in Chap. 5. Fig. 6.1 demonstrates densities measured for both experimental campaigns. As it can be seen, for the discharges treated in Chap. 5 a high reproducibility in the density from discharge to discharge (better than 1.3%) was achieved during the steady state (1 s$< t <$3 s), as well as during the first second of the discharge for both plasma currents. In contrast to Fig. 6.1 a), the density in Fig. 6.1 b) shows a not so

high reproducibility from discharge to discharge. For example, at $B_t = 1.6$ T the density is lower at 0.17 s$< t <$1 s and at $t = 0.04$ s. The difference in density is especially important at the start up of the discharge, when the runaway production is mainly defined by the primary generation process [64]. A similar analysis as performed in Chap. 5 demonstrates that a two times discrepancy in the density leads to the difference in the total produced number of runaways (primary + secondary processes) up to two orders of magnitude after the first second of the discharge, as shown in Fig. 6.1 c).

Trends of an another important parameter, the loop voltage (V_{loop}), is shown in Fig. 6.2 for the plasma conditions in Chap. 5 and in the present ones. At the start up of the discharge ($t < 0.05$ s) the electric field strength exceeds the E_D, where $E_D = e^3 n_e \ln\Lambda/(4\pi\epsilon_0^2 T_e)$ [64] is the Dreicer field and the primary generation of runaways occurs. In Fig. 6.2 a)-c), during the first milliseconds the trend of V_{loop} is rather reproducible from discharge to discharge for both experimental days. Till $t \approx 0.2$ s the loop voltage decreases and reaches some steady state. For both experimental campaigns, the average loop voltage (between 0.5 and 3 s) decreases with increasing B_t, as shown in Fig. 6.2 a)-c). Nevertheless, the comparison of the loop voltage slopes for the present plasma discharges with ones in Chap. 5, in Fig. 6.2 d) shows that V_{loop} reduces by about 7% stronger at 2.3 T$\leq B_t \leq$2.7 T for the second run as compared to the first one. Thus, it can be expected that during these experiments the stronger reduction of the loop voltage at $B_t \geq 2.3$ T leads to the relatively lower production of runaway electrons in comparison with the number of runaways produced at $B_t = 2.2$ T.

6.3 Measurements

6.3.1 Neutron measurements

In Fig 5.1 the synchrotron radiation and the averaged neutron signal during the first half second after the end of the discharge show the same dependencies on B_t. Neutron detectors detect electrons which lost the confinement. Therefore, after the end of the discharge, the average neutron signal between 3.5 s and 4 s is proportional to the number of electrons produced before the

termination of the discharge. However, an influence of the injected He-gas has to be taken into account, which is used to gently terminate the discharge. In Fig. 6.1 b) the density is rather reproducible between 3.5 s and 4 s. Thus it is possible to conclude that the influence of the helium gas injection can be neglected on the neutron measurements at different B_t.

Results of measurements of runaway electrons after the end of the dis-

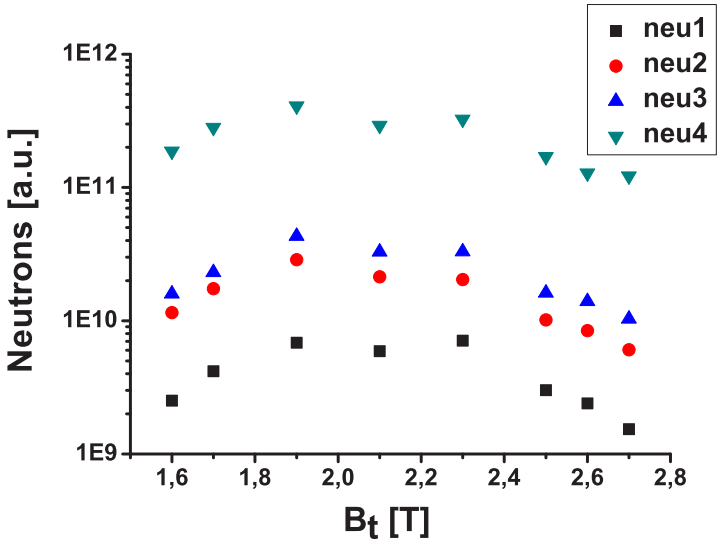

Figure 6.3: *The dependence of the number of runaway electrons on the toroidal magnetic field for the plasma current of 400 kA. Neutron measurements, signal averaged between 3.5 s and 4 s. Signals for four different neutron detectors are shown. Detectors possess different sensitivities to neutrons. Existence of maxima for all neutron signals are observed at* $B_t \approx 2.2$ *T.*

charge between 3.5 and 4 s are shown in Fig. 6.3. In Chap. 5 the neutron signal as well as synchrotron radiation increase with magnetic field. However, a maximum of runaway electron population was observed at B_t of 2.5 T. During these measurements this maximum shifts to B_t about 2.2 T.

In order to explain the maximum we consider characteristic parameters in more detail. The displacement of a maximum as well as its existence can be explained by the difference in plasma parameters, like the plasma density and the loop voltage. As it has been discussed before, the plasma density shows some variations at different magnetic fields. In particular during the start-up phase, the density increases at $B_t \geq 2.2$ T. Furthermore, apparently in Fig. 6.2 d), the loop voltage decays more rapidly at $B_t \geq 2.2$ T in the

present discharges than in previous ones. Thus, both effects, the increase of the plasma density and the decrease of the loop voltage, lead to a reduction in the runaway production at $B_t > 2.2$ T. This explains the apparent maximum in the neutron production; it means also that we do not expect an extra loss channel due to the turbulence of the runaways beyond the maximum.

6.3.2 Probe measurements

Measurements of the runaway loss from the plasma were carried out by the scanning probe. The probe was inserted three times during the discharge (1 s, 2 s and 3 s). Electrons with energies higher than 4 MeV penetrate the graphite mantle of the probe and can be detected by the first crystal.

The measured energy spectrum represents the runaways at the radial position corresponding to the tip of the probe. If the gradient of the density is known one can try to derive also the spectrum of those runaways which are further inside the plasma.

The number of electrons detected by the first crystal is shown in Fig. 6.4. An increase of the electron number to the low B_t is observed. In general, the number of detected electrons increases from the first insertion to the second one. However, it is interesting to mention that at B_t of 1.6 T the detected number of runaways coming from the plasma is higher at the beginning of the discharge. Between 2 s and 3 s, the transformer current of TEXTOR passes from positive to negative values. It has been found, that this leads to a general change of the magnetization of the iron in the transformer resulting in a slight modification of plasma parameters, such as the plasma shape (elongation). The difference of the probe signals at $t = 2$ s and $t = 3$ s is attributed to this effect. At a first glance Fig. 5.1 and Fig. 6.4 seem to show opposite trends of the runaways development with respect to B_t. However, both figures are consistent because Fig. 5.1 represents the runaways kept inside the discharge while Fig. 6.4 gives their loss: The higher loss rate at low B_t corresponds to the decreased confinement and vice versa.

In order to obtain an information about runaway electron spectra at different insertion times and magnetic fields, a method of the analysis is performed, which is described in Sec. 3.2.2. From the comparison of the measured signal

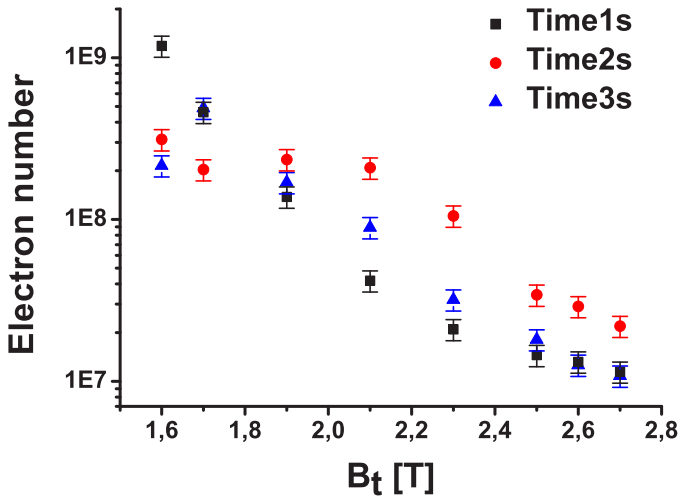

Figure 6.4: *Probe measurements of runaways at the r=47 cm minor radial position are performed at 1; 2 and 3 s during the discharge. Number of electrons detected by the first crystal of the probe are shown at different B_t. Electrons with energies higher than 4 MeV can be detected by the first crystal. The front surface of the crystal is $S = 2\ mm^2$ and the detected time interval was $\delta t = 40\ ms$.*

ratios with the simulated ones using 3D Geant4 code [42] the electron distribution in the energy range between 4 and 30 MeV can be obtained.

The method of the spectral analysis allows to understand how electrons are distributed in the energy range between 4 and 30 MeV. However, in order to get a more detail knowledge about the ratios of electron numbers with energies less than 16 MeV, another technique is used, described in Sec. 3.2.1. This method bases on the definition of the minimum energies which can be detected by each crystal. Nevertheless, with increasing electron energy (above 16 MeV for the present probe), this method is not able to be used any longer due the big uncertainties in the stopping length of electrons and the possible influence of x-rays.

Results of the spectral analysis are shown in Fig. 6.5 for different magnetic fields. The best approximation for the measured signal trends is the decreasing function up to a cut-off energy (in the logarithmic scale of the ordinate). The cut-off energy increases with time and depends on B_t. At 1 s the reduction of the relative number of high energy electrons takes place with the decreasing magnetic field. The number of electrons with different energies is mainly de-

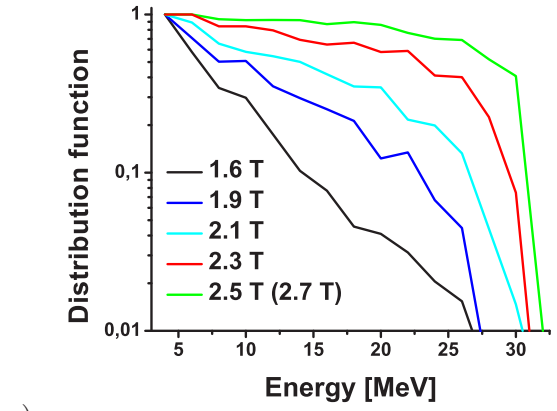

a)

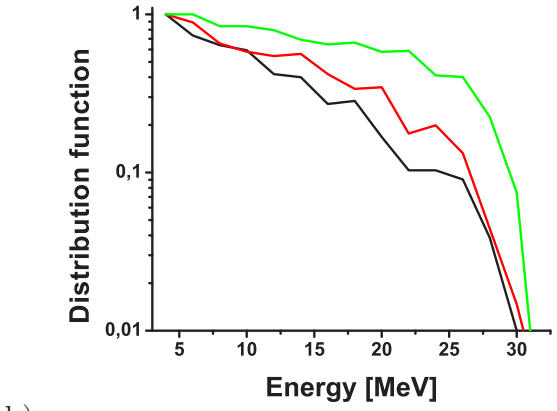

b)

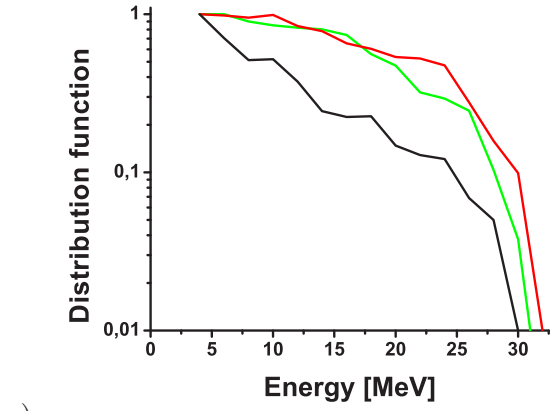

c)

Figure 6.5: *Spectral measurements by the scanning probe at 47 cm minor radial position at three times during the discharge. a) Spectra at B_t of 1.6; 1.9; 2.1; 2.3; 2.5 T and 2.7 T at 1 s. b) Spectra at B_t of 1.6; 2.3; 2.5 T and 2.7 T at 2 s. c) Spectra at B_t of 1.6; 2.3; 2.5 T and 2.7 T at 3 s.*

fined by the production and loss mechanisms. The runaway production does not depend on the magnetic field and is mainly defined by the density and the loop voltage. At B_t of 1.6 T, the density is lower and the loop voltage is higher than these parameters at B_t of 2.5 T, as shown in Fig. 6.1 b) and Fig. 6.2 c). The enhanced runaway number at low B_t measured by the crystal 1 in Fig. 6.4 is in agreement with the increased loop voltage. However the decreasing of the high energy part of the runaway spectrum and the reduced cut-off energy at low B_t is contradictory to the enhanced loop voltage. These can only be explained by the enhancement of the radial loss of runaway electrons with low energies with decreasing magnetic field. In this case, low relativistic electrons are lost from the plasma before they can be accelerated to highly relativistic energies. A similar effect has been observed during externally applied magnetic fluctuations by the dynamic ergodic divertor (DED) in [36]. During the stationary phase of the discharge ($t \geq 2$ s) the difference between distribution functions at low and high magnetic fields is substantially reduced. Hence, it would be expected that the dependence of the radial transport on B_t becomes weaker during the stationary phase.

In order to get a more detailed picture about the loss of electrons with different energies from the plasma, the technique described in Sec. 3.2.1 is used. For the present analysis, three energy ranges have been defined 4-8 MeV; 8-16 MeV and 16-30 MeV. In Fig. 6.6, the number of electrons per MeV at three energies are shown at 1 s; 2 s and 3 s during the discharge. In general, the number of runaways in the three energy groups decreases with increasing B_t. The population of runaways with lower energies is higher than that of higher energies. There is little difference between $t = 2$ s and $t = 3$ s, i.e. the runaway spectrum is in a stationary phase. This is in contrast compared to the measurements at $t = 1$ s. Here the number of the runaways in the higher energy groups is substantially reduced. The high energy part of runaways has not yet reached the stationary spectrum. The loss of electrons from the plasma depends strongly on the strength of the toroidal magnetic field and the energy of runaways. The ratio of the detected number of electrons with low energies to the higher ones is increasing with the decreasing magnetic field. The flux of electrons with energies 4-8 MeV is one order of magnitude higher at 1 s than at $t \geq 2$ s for B_t of 1.6 T.

Fig. 6.7 a) shows ratios of electron numbers detected by the probe with

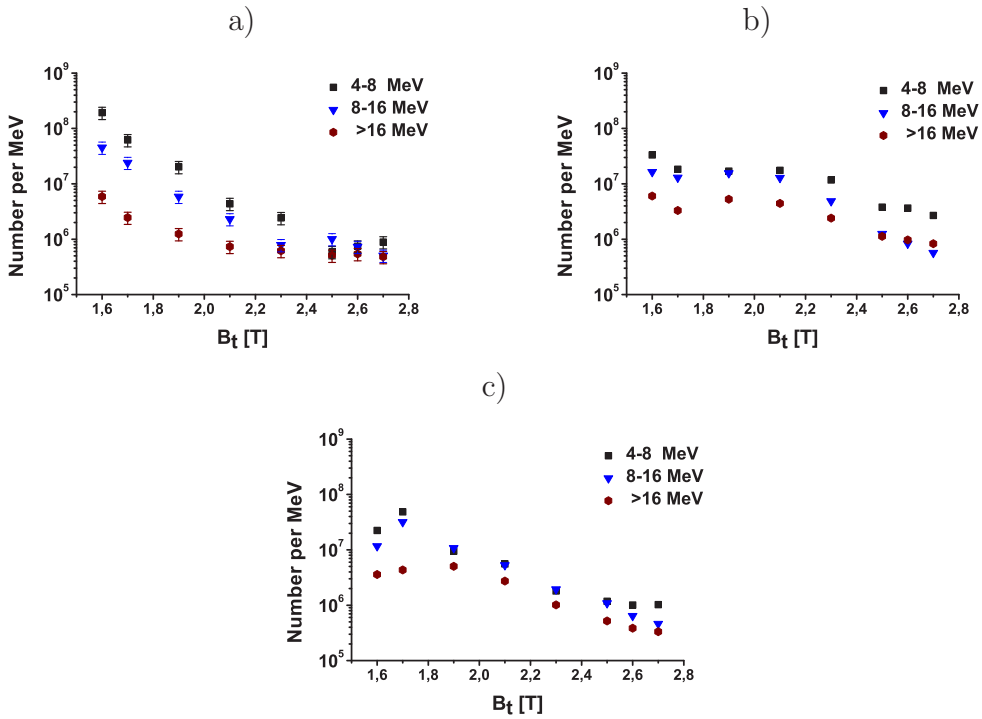

Figure 6.6: *Measurements of runaway electrons at different toroidal magnetic fields at 1 s; 2 s and 3 s during the discharge. Averaged number of electrons lost from the plasma per 1 MeV in three energy ranges are shown at time: a) 1 s; b) 2 s; c) 3 s.*

energies between 4 and 16 MeV at three times during the discharge. At the first second of the discharge the ratio depends exponentially on the magnetic field. Later in time ($t \geq 2$ s) the ratio is almost independent of B_t. For electrons with energies between 4 and 8 MeV, the ratio of their numbers does not change much with B_t and time, as shown in Fig. 6.7 b).

Comparisons of the measured trends in Fig. 6.6 and Fig. 6.7 demonstrate following important results: i) at the first second of the discharge the radial transport increases differently with the decreasing magnetic field for electrons with different energies; ii) later in time (at $t \geq 2$ s) the radial transport changes with the same proportionality with B_t for electrons with high and low energies. Further, the dependence of the radial transport on B_t and electron energies are considered.

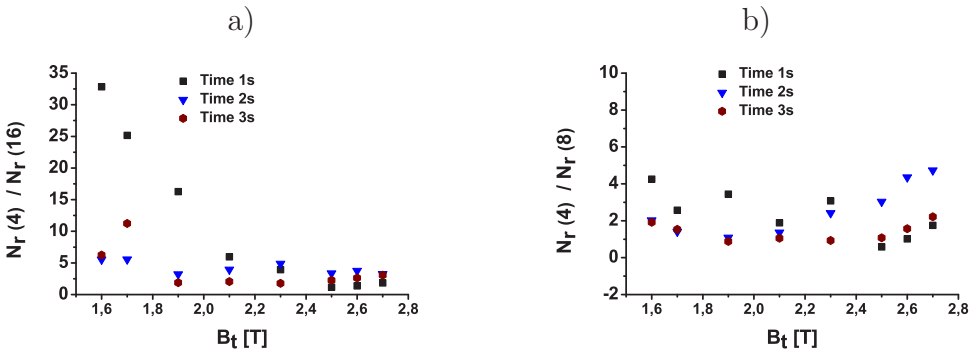

Figure 6.7: *Ratio of numbers of electrons detected by the probe with energies a) 4 and 16 MeV and b) 4 and 8 MeV at 1, 2 and 3 s during the discharge.*

6.4 Discussion

Runaway electron flux from the plasma, which is actually detected by the probe, is related to the gradient of the density by Fick's law:

$$\mathbf{\Gamma} = -\mathbf{D_r}\nabla\mathbf{n_r}, \tag{6.1}$$

where D_r is the radial diffusion coefficient and n_r is the runaway electron density. In general, the diffusion coefficient as well as ∇n_r depends on the minor radius, therefore the radial transport can vary across the plasma. Since the probe is placed at the plasma edge, the number of electrons detected by the probe is proportional to some averaged flux of runaways along the minor radius of the plasma.

6.4.1 Diffusion coefficient

Stationary phase of the discharge

In Chap. 5, in Fig. 5.3, the diffusion coefficient was measured at different magnetic fields for electrons with energies above 25 MeV during the stationary phase of the discharge. Additionally, the analysis of the magnetic fluctuation level on different toroidal magnetic fields has been performed in Fig. 5.5. The simplest approach of the diffusion coefficient ($D_{RR} = \pi qRc(\delta B/B)^2$), derived by Rechester and Rosenbluth [88], has been used.

In [78, 80] it was shown that magnetic drift effects can reduce substantially the radial diffusion of runaways, because the orbits of runaways are displaced from the magnetic structure underlying the magnetic perturbation. From the analysis by Myra and Catto in [80], the quasi-linear diffusion coefficient is estimated as $D_r = \Upsilon \pi q R c (\delta B/B)^2$, where Υ is a drift modification factor. Corresponding to [80], effects of the magnetic drift on the diffusion coefficient is very complicated and depends on details of the perturbation such as its poloidal localization and a radial correlation length [80, 81]. The drift becomes important when the orbit shift Δ_e exceeds the mode width Δ_m. The diffusion coefficient decreases slowly (algebraically) or rapidly (exponentially) with Δ_e/Δ_m depending on the poloidal structure of the perturbation. The orbit shift depends on the energy of runaway electrons [74, 75] and it is given in the first-order approximation by: $\Delta_e \approx \frac{qW_r}{ecB_t}$, where W_r is the electron energy, q is the safety factor. For electrons with energies between 4 and 30 MeV, the orbit shift can vary between 0.5 and 6.25 cm (with $q = 1$ and $B_t = 1.6 - 2.7$ T). The mode width estimated in Ohmic plasmas in [20] based on the model by Mynick and Strachan [79] is less than 0.5 cm. Thus, in the present analysis, the ratio Δ_e to Δ_m is bigger than 1.

According to [80], explicit forms for Υ were found by invoking simple drift orbits for the runaways. The form of Υ depends on whether the magnetic perturbation is localized in a poloidal angle or randomly phased and hence distributed in the poloidal angle. For the localized distribution two cases are possible: 1) the perturbation is assumed to be localized at the top or bottom of the torus ($\beta_0 = \pm\pi/2$); and 2) the inside or outside of the torus ($\beta_0 = 0, \pi$). According to [80], if the perturbation is localized at the top or bottom of the torus, Υ is approximated, as: $\Upsilon_{loc,\pm\pi/2} = [1 + 4x^2(1-2x)^2\Delta_e^2/m^2\Delta_m^4]^{-1/2}$, where x is the transformation parameter ($x = (a-r)/a$) and m is the mode number. In case of $\beta_0 = 0, \pi$, $\Upsilon_{loc,0,\pi} = exp(-2x^2\Delta_e^2/\Delta_m^2)$. In the remaining randomly phased (hence poloidally uniform) magnetic perturbation (RPA), Υ is estimated, as: $\Upsilon_{RPA} = \Delta_m/(2\pi)^{1/2}\Delta_e x$.

Fig. 6.8 shows the dependence of Υ on the orbit shift for the three discussed cases above: $\Upsilon_{loc,\pm\pi/2}$, $\Upsilon_{loc,0,\pi}$ and Υ_{RPA}. Estimations have been performed for Δ_e between 0.5 and 4 cm, which corresponds to the energies of electrons in Fig. 6.6. The following parameters are used for this analysis: $m = 2$, $\Delta_m = 0.5$, and $x = 0.6$. The shown trends in Fig. 6.8 are in good agreement with nu-

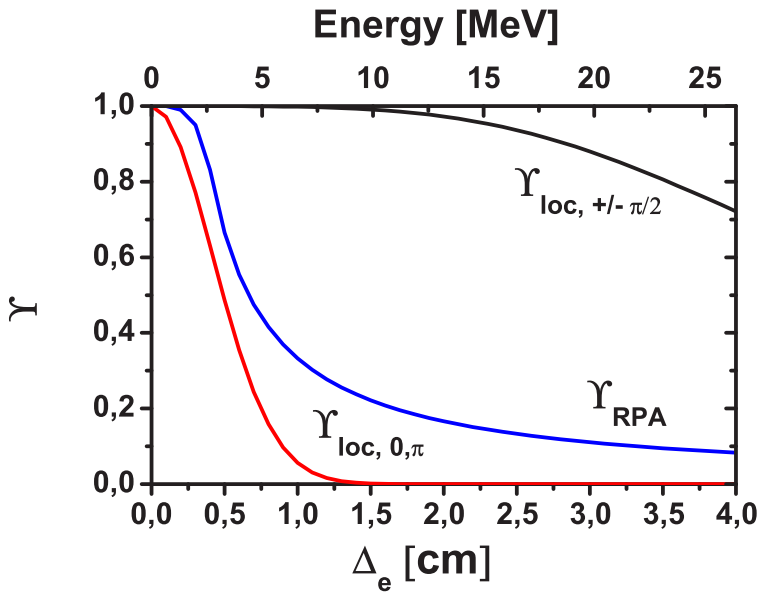

Figure 6.8: *Drift modification factors* Υ *(*$\Gamma \sim D_r \sim \Upsilon$*) for three different poloidal structures of perturbation: localized to the top/bottom (*$\beta_0 = \pm\pi/2$*), the inside/outside (*$\beta_0 = 0, \pi$*) or the random phase approximation (RPA) (with the transformation parameter* $x = 0.6$*,* $\Delta_m = 0.5$ *and m=2). The dependence of* Υ *on the orbit shift,* $\Delta_e \approx \frac{qW_r}{ecB_t}$ *and the corresponding electron energies at* $B_t = 2.2$ *T (upper scale).*

merical results in [80] ($m = 20$, $\Delta_m = 0.05$, and $x = 0.5$). For the localized perturbation to the top/bottom the drift modification is negligible. The other two cases: $\beta_0 = 0, \pi$ or RPA cause remarkable reduction of Υ for moderate values of Δ_e.

The ratio of the number of electrons with energies between 4 and 16 MeV is proportional to the ratio of the corresponding electron fluxes, $\frac{N(4)}{N(16)} \sim \frac{\Gamma(4)}{\Gamma(16)} = \frac{D_r(4)\nabla n_r(4)}{D_r(16)\nabla n_r(16)}$. As it follows from Fig. 6.7 a), at $t \geq 2$ s, $\frac{N(4)}{N(16)}$ is almost constant and mainly this value does not exceed 5. Therefore, the total possible effect on $\frac{N(4)}{N(16)}$ of $D_r \sim \Upsilon$ and ∇n_r should not exceed 5. At $t \geq 2$ s, $\frac{N(4)}{N(16)} \sim \frac{\Upsilon(4)}{\Upsilon(16)}$ does not show any exponential behavior on B_t, which follows from the $\Upsilon_{loc,0,\pi} = exp(-2x^2\Delta_e^2/\Delta_m^2)$ approximation, where $\Delta_e \sim \frac{1}{B_t}$. Additionally, it is not expected that magnetic fluctuations are localized at the top or bottom of the torus and at the inside or outside of the torus in the TEXTOR tokamak. Thus, $\Upsilon_{RPA} = \Delta_m/(2\pi)^{1/2}\Delta_e x$ can be considered as a drift modification factor in the further analysis of the present experimental results

($\frac{\Upsilon_{RPA}(4)}{\Upsilon_{RPA}(16)} = 4$ and independent on B_t).

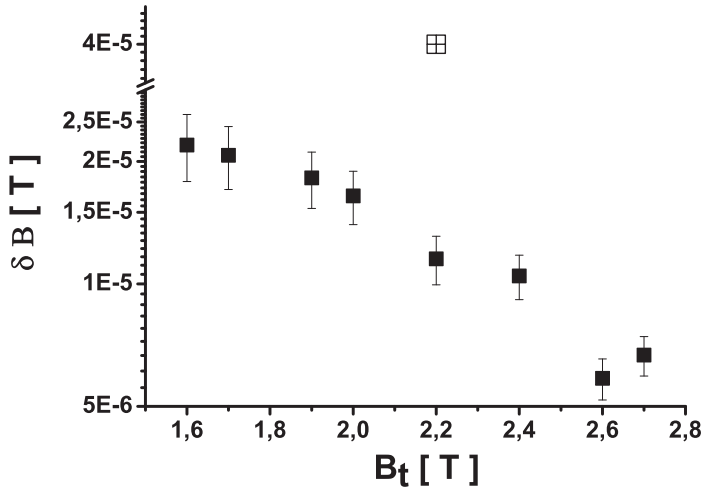

Figure 6.9: *Fluctuation level determined during the stationary phase of the discharge. The drift modification factors Υ_{RPA} is used in $D_r = \Upsilon \pi q R c (\delta B/B)^2$. ⊞ the fluctuation level estimated in [20, 21] using the model by Mynick and Strachan [79]*

6.4.2 Magnetic fluctuation

Radial transport during the stationary phase of the discharge

Applying the model by Myra and Catto [80], more exact calculations of δB can be performed in the stationary phase of the discharge, i.e. for $t \geq 2$ s. Diffusion coefficients have been derived in Chap. 5 at the end of the discharge for electrons with energies above 25 MeV at B_t between 2 and 2.7 T, and extrapolated to lower B_t values. Using the dependence of Υ_{RPA} on the electron energy, the magnetic fluctuation level at B_t of 1.6-2.7 T can be estimated.

Results of estimation of the magnetic fluctuation level are shown in Fig. 6.9. The magnetic perturbation decreases with the magnetic field and amounts to $6 \cdot 10^{-6} \leq \delta B \leq 2.2 \cdot 10^{-5}$ at 2.7 T$\geq B_t \geq$1.6 T respectively. Consequently, both models by Myra and Catto [80] and by Rechester and Rosenbluth [88] result in the same trend of the increase of the magnetic fluctuation level with decreasing B_t. However the fluctuation level itself is almost 4 times higher

in the model by Myra and Catto [80] at the same magnetic field values. In [20, 21] using the model by Mynick and Strachan [79], in Ohmic plasmas it is found that $\delta B/B \sim 2 \cdot 10^{-5}$ at $B_t = 2.2$ T.

6.4.3 ∇n_r effect

Radial transport during the transitional phase of the discharge at 1 s

Analysis of the magnetic perturbation at 1 s is rather complicated due to the following reasons: a) There is no information about the diffusion coefficient at 1 s. b) The radial transport of runaway electrons is found in the non stationary phase of the discharge and changes with the magnetic field. Further, the analysis of the diffusion coefficients and the magnetic fluctuation level are performed under a certain assumption of ∇n_r of electrons with energies of about 4 MeV. This analysis possesses a certain level of speculation, because some of important parameters are obtained at different plasma areas or under certain approximations.

Fig. 6.6 shows that the radial transport depending on the electron energies demonstrates a different behavior at the first second and during the stationary phase of the discharge. As a result, runaway spectra detected by the probe at $t = 1$ s and $t \geq 2$ s are also different. At $t \geq 2$ s slight uncertainties in the electron spectra at low and high magnetic fields are attributed to the increase of the radial transport due to the decrease of the diffusion coefficient with B_t. From the model by Myra and Catto [80] it is shown that the reduction of the diffusion coefficients with the magnetic field is accompanied by the corresponding decrease of the magnetic fluctuation level.

The appreciable difference in the energy distributions at $B_t = 1.6$ T and $B_t = 2.5$ T at 1 s has been explained by the stronger depopulation of the runaway electrons. Therefore, electrons are mainly lost before they can be accelerated up to energies higher than 16 MeV. This explanation agrees also with results in Fig. 6.6, where the number of electrons with energies of about 4 MeV is almost one order of magnitude higher at $t = 1$ s and $B_t = 1.6$ T than the value at $t \geq 2$ s and at the same magnetic field.

It is interesting to obtain information about the diffusion coefficients and the directly related magnetic fluctuation level (using the model by Myra and

Catto [80]) at 1 s of the discharge. In this case more information of the evolution of the diffusion coefficient and the magnetic perturbation can be obtained in time. Although, there are no measurements of the diffusion coefficient at $t = 1$ s, it can be obtained from the comparison of the radial flux of highly relativistic electrons at $t = 1$ s and $t = 3$ s

$$\frac{\mathbf{N(16)_{t=1s}}}{\mathbf{N(16)_{t=3s}}} = \frac{\mathbf{D_r(25)_{t=1s}\nabla n_r(25)_{t=1s}}}{\mathbf{D_r(25)_{t=3s}\nabla n_r(25)_{t=3s}}}. \tag{6.2}$$

In order to estimate the diffusion coefficient information about $\nabla n_r(25)$ is

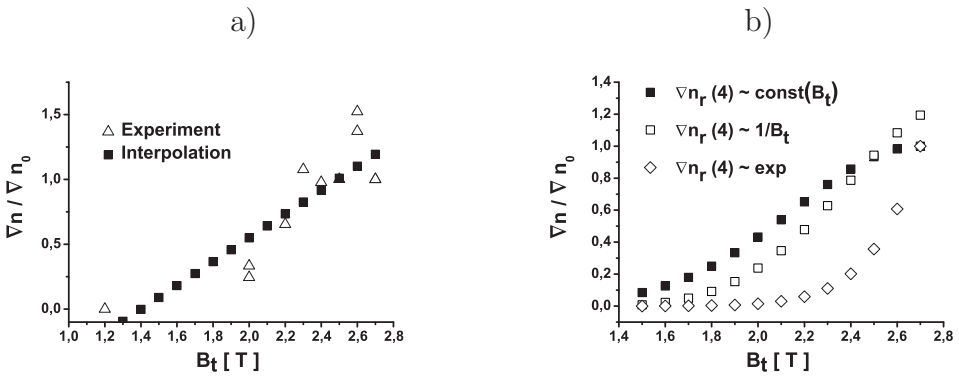

Figure 6.10: *The radial profile of* $\nabla n_r(25)$ *normalized to the corresponding value at* $B_t = 2.7$ *T* ($\nabla n_r(25)_{B_t=2.7T} = \nabla n_0$). *a) At* $t = 3$ *s the radial profile of* $\nabla n_r(25)$ *is analyzed from the radial distribution of the synchrotron radiation at the minor radius between 15 cm and 25 cm. b) At* $t = 1$ *s the profile is analyzed from the ratio of the detected numbers of electrons with energies 4-8 MeV and* ≥ 16 *MeV in Fig. 6.7 a). Three possibilities of* $\frac{\nabla n_r(4)}{\nabla n_r(4)_{B_t=2.7T}}$ *on* B_t *are considered: i)* $\frac{\nabla n_r(4)}{\nabla n_r(4)_{B_t=2.7T}}$ *is constant, ii)* $\frac{\nabla n_r(4)}{\nabla n_r(4)_{B_t=2.7T}}|_{t=1s} \sim \frac{\nabla n_r(25)}{\nabla n_r(25)_{B_t=2.7T}}|_{t=3s}$ *(linear approximation) and iii)* $\frac{\nabla n_r(4)}{\nabla n_r(4)_{B_t=2.7T}}|_{t=1s} \sim \frac{N(4)}{N(4)_{B_t=2.7T}}|_{t=1s}$ *(exponential approximation).*

required at $t = 1$ s and $t = 3$ s. At $t = 3$ s from the synchrotron measurements, the trend of $\nabla n_r(25)$ can be roughly estimated, where $\nabla n_r(25) \sim \frac{\partial I(r)}{\partial r}$ (I(r) is the radial distribution of the synchrotron radiation measured in Chap. 5). The interpolating spline of $\frac{\nabla n_r(25)}{\nabla n_r(25)_{B_t=2.7T}}$ together with the experimentally defined trend from the synchrotron measurements are shown in Fig. 6.10 a) at $t = 3$ s during the discharge. In the analysis it was also used $\nabla n_r(25)_{B_t=1.2T} = 0$ at $B_t \leq 1.2$ T. In order to get information about $\nabla n_r(25)$ at $t = 1$ s, the analysis of the synchrotron radiation is hard to apply, because the synchrotron emission is weak and the signal is strongly affected by the background thermal emission

from the plasma and the tokamak liner. Especially, the "thermal noise" exerts a relatively strong influence on the signal at low magnetic fields, where the synchrotron emission is lower.

In Fig. 6.7 a) the ratio of the detected numbers of runaways with energies between 4 and 8 MeV and $\geq$ 16 MeV is an exponential function of B_t at $t = 1$ s. From the spectral measurements it is expected that the number of runaways with energies higher than 16 MeV reduces substantially with the decreasing magnetic field. If the detected number of runaways is proportional to their flux, then $\frac{N(4)}{N(16)} = \frac{\Upsilon_{RPA} \cdot \nabla n_r(4)}{\Upsilon_{RPA} \cdot \nabla n_r(16)} \approx \frac{4 \cdot \nabla n_r(4)}{\nabla n_r(16)}$. Since $N(16)$ is the average detected number of electrons with energies higher than 16 MeV, it is expected that $\nabla n_r(16) \sim \nabla n_r(25)$.

For electrons with energies of about 4 MeV, $\nabla n_r(4)$ is expected to be

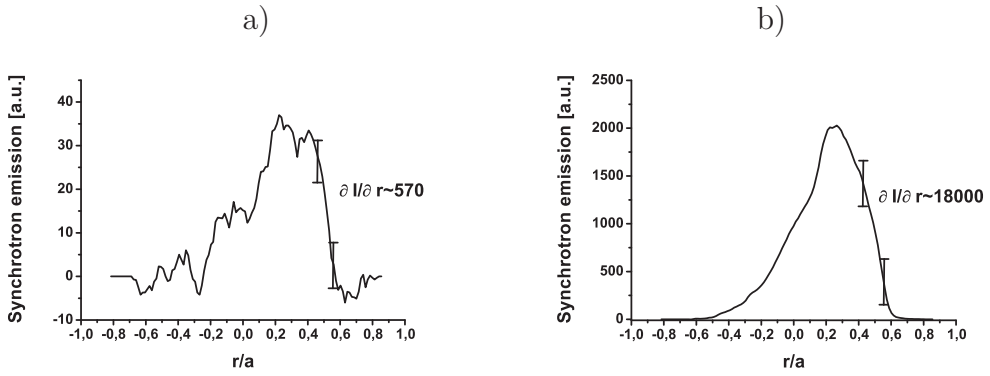

Figure 6.11: *Radial profiles of the synchrotron radiation intensity are shown at $B_t = 2.7$ T measured in Chap. 5 at times a) $t = 1$ s and b) $t = 3$ s. The analysis of $\frac{\partial I}{\partial r}$ has been done at 20 cm$\leq r \leq$25 cm (a=46 cm) and equals a) $\frac{\partial I}{\partial r} \approx 570$ and b) $\frac{\partial I}{\partial r} \approx 18000$*

constant or an increasing function with B_t. For variable $\nabla n_r(4)$ two cases are considered:

1. the extreme case $\frac{\nabla n_r(4)}{\nabla n_r(4)_{B_t=2.7T}|_{t=1s}} \sim \frac{N(4)}{N(4)_{B_t=2.7T}|_{t=1s}}$, i.e. the dependence of $N(4)_{t=1s}$ on B_t is mainly defined by $\nabla n_r(4)$ (exponential approximation).

2. $\frac{\nabla n_r(4)}{\nabla n_r(4)_{B_t=2.7T}|_{t=1s}} \sim \frac{\nabla n_r(25)}{\nabla n_r(25)_{B_t=2.7T}|_{t=3s}}$ (linear approximation).

Whether $\nabla n_r(4)$ is a variable or constant function of B_t, $\frac{\nabla n_r(25)}{\nabla n_r(25)_{B_t=2.7T}|_{t=1s}}$ depending on the magnetic field is shown in Fig. 6.10 b).

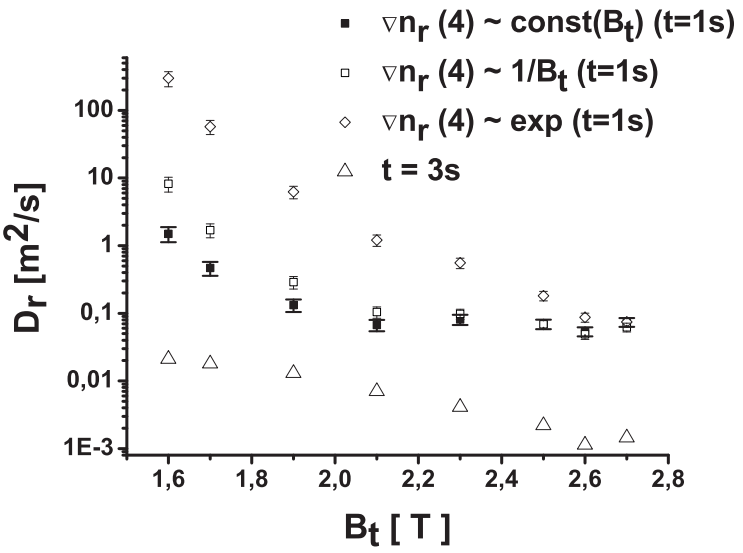

Figure 6.12: *Diffusion coefficients at 1 s and 3 s. At the end of the discharge diffusion coefficients are measured by synchrotron radiation in Chap. 5 at B_t of 2-2.7 T and extrapolated to 1.6 T. From the analysis of radial transports at 1 s and 3 s, diffusion coefficients are estimated at the beginning of the discharge. In the analysis three dependencies of $\frac{\nabla n_r(4)}{\nabla n_r(4)_{B_t=2.7T}}$ on B_t are considered: i) $\frac{\nabla n_r(4)}{\nabla n_r(4)_{B_t=2.7T}}$ is constant, ii) $\frac{\nabla n_r(4)}{\nabla n_r(4)_{B_t=2.7T}|t=1s} \sim \frac{\nabla n_r(25)}{\nabla n_r(25)_{B_t=2.7T}|t=3s}$ and iii) $\frac{\nabla n_r(4)}{\nabla n_r(4)_{B_t=2.7T}|t=1s} \sim \frac{N(4)}{N(4)_{B_t=2.7T}|t=1s}$.*

At $t = 1$ s, using profiles of $\nabla n_r(25)$ found in Fig. 6.10, diffusion coefficients can be estimated from Eq. (6.2) at 1.6 T$\leq B_t \leq$2.7 T. In order to determine, diffusion coefficients at 1 s from the measured ones in Chap. 5 during the stationary phase of the discharge, the ratio $\frac{\nabla n_r(25)_{t=1s}}{\nabla n_r(25)_{t=3s}}$ at B_t of 2.7 T is necessary to know. In Fig. 6.11 radial profiles of the synchrotron radiation are shown at B_t of 2.7 T at $t = 1$ s and $t = 3$ s. From the analysis of $\frac{\partial I}{\partial r}$ at 20 cm$\leq r \leq$25 cm (a=46 cm), it follows that $\frac{\nabla n_r(25)_{t=1s}}{\nabla n_r(25)_{t=3s}} \approx 0.03$.

Applied the found dependencies of $\nabla n_r(25)$ on the magnetic field and time, diffusion coefficients can be estimated at $t = 1$ s from the measured ones at $t = 3$ s using Eq. (6.2). Fig. 6.12 shows the result of this estimation. The diffusion level is more than one order of magnitude higher at $t = 1$ s than the corresponding one at $t = 3$ s. For the extreme case $\frac{\nabla n_r(4)}{\nabla n_r(4)_{B_t=2.7T}|t=1s} \sim \frac{N(4)}{N(4)_{B_t=2.7T}|t=1s}$ the diffusion level seems to be overestimated. Therefore, in the further analysis of the magnetic fluctuation level two approximation are considered: constant

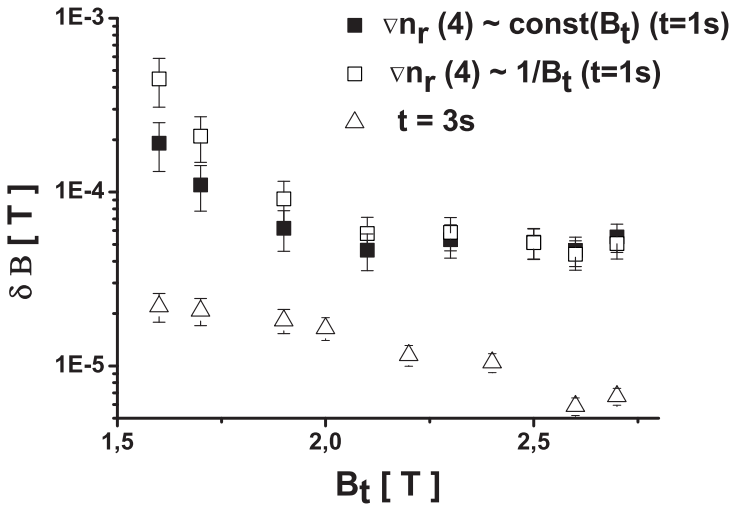

Figure 6.13: *Fluctuation levels determined at 1 and 3 s during the discharge. The drift modification factor Υ_{RPA} is used. At $t = 1$ s the fluctuation level is estimated under two approaches to $\nabla n_r(4)$: i) $\frac{\nabla n_r(4)}{\nabla n_r(4)_{B_t=2.7T}}$ is constant and ii) $\frac{\nabla n_r(4)}{\nabla n_r(4)_{B_t=2.7T}}|_{t=1s} \sim \frac{\nabla n_r(25)}{\nabla n_r(25)_{B_t=2.7T}}|_{t=3s}$.*

$\nabla n_r(4)$ and $\frac{\nabla n_r(4)}{\nabla n_r(4)_{B_t=2.7T}}|_{t=1s} \sim \frac{\nabla n_r(25)}{\nabla n_r(25)_{B_t=2.7T}}|_{t=3s}$ (linear approximation).

In the model by Myra and Catto [80] the magnetic fluctuation level can be estimated from the diffusion coefficients at $t = 1$ s. Results of the estimation of the fluctuation level at the beginning and at the end of the discharge are shown in Fig. 6.13. Almost independently on the used approach to $\frac{\nabla n_r(4)}{\nabla n_r(4)_{B_t=2.7T}}|_{t=1s}$, at $t = 1$ s the perturbation level is about 10 times higher than during the stationary phase of the discharge. Within the limits of the used model [80], the magnetic perturbation demonstrates a clear trend of the increase of δB with decreasing B_t. The transport of runaway electrons, due to their high parallel momentum, is mainly affected by the magnetic perturbation [21, 69, 79, 80]. At the same time production mechanisms are mainly defined by the plasma density, the loop voltage and Z_{eff}. Therefore it is also natural to predict an enhancement of the fluctuation level at low B_t from the probe measurements in Fig. 6.5 and Fig. 6.6. Consequently, the trend of the magnetic perturbation with B_t in Fig. 6.13 agrees well with measured results by the synchrotron radiation in Chap. 5 and by the probe in the present chapter. Furthermore, it

is reasonably to assume, that in the present measurements the growth of the magnetic fluctuation level to the low magnetic field causes an increase of the radial transport and the subsequent reduction of the runaway numbers in the plasma.

Chapter 7

Transport of runaway electrons in the presence of the dynamic ergodic divertor

7.1 Introduction

The production of runaway electrons is a rather undesirable effect due to the possible damages of plasma facing materials or an actively cooled carbon limiter in big tokamaks and especially in the future International Thermonuclear Experimental Reactor (ITER) [54, 87]. At present, there are few techniques, which can be used to start a mitigation process: massive gas injection by a special "disruption mitigation valve" [31, 32, 34, 52, 104], by killer pellets [55] or externally applied magnetic fluctuations [72, 106]. In the case of the first two techniques, pumping systems can experience heavy loads. Magnetic perturbations are a relatively little investigated method and until now experimental studies have been carried out in JT-60 [106] and in TEXTOR [35, 36, 37, 72, 103].

In the TEXTOR tokamak, external magnetic perturbations are generated by the dynamic ergodic divertor (DED) [30]. The influence of the resonant magnetic perturbation (RMP) on the radial transport of runaways has been studied in [35, 37, 103] during low density plasma discharges. It was shown that the applied external stochastic fields cause an increase of the radial transport. Synchrotron radiation measurements performed in TEXTOR tokamak

for electrons with energies above 25 MeV demonstrates the reduction of the signal in the presence of the dynamic ergodic divertor [35, 37]. However the decrease of the synchrotron signal occurs with some delay in time. This result was explained by different sensitivities of runaways to the DED depending on their energy. As a result, mainly low relativistic electrons experience a higher loss from the plasma due to the DED. Later in time the common reduction of low energy runaways causes the decrease of the total number of electrons accelerated up to energies above 25 MeV. Numerical analysis performed in [103] shows that the escape rate λ for the exponential decay number of runaways ($N(t) = N_0(N_1 + exp^{-\lambda t})$) decreases linearly with increasing kinetic energy. In $N(t) = N_0(N_1 + exp^{-\lambda t})$, N_0 is the numbers of particles before the DED and N(t) is the number of particles left in the system at time t during the DED. Additionally, it was predicted that electrons with energies more than 20 MeV are almost not affected by the dynamic ergodic divertor in the m/n=3/1. The first experimental studies, which could be considered in favor of these numerical results were described in [36, 37, 103]. Nevertheless, to measure electrons with different energies two different diagnostics were used namely synchrotron radiation [29, 59] and electron cyclotron emission (ECE), which did not provide a possibility to compare quantitatively the loss of runaways with different energies.

In the present chapter losses of runaway electrons with different energies are studied in presence of the DED for the 3/1 mode. The following issues are considered: what happens with runaway electrons during the DED; whether, the lost of runaways holds in the same dependence on the runaway energy as it was predicted in [103].

7.2 Experimental set-up

Measurements of runaway electrons affected by the dynamic ergodic divertor were carried out in the TEXTOR tokamak with the following plasma parameters: the plasma current, $I_p = 300$ kA; the plasma density, $n_e = 0.7{\cdot}10^{19}$ (low density plasma discharge) and the magnetic field, $B_t = 2.25$ T. The DED was switched on in the interval 2.5 s$< t <$3.5 s with a DED current (I_{DED})

between 0 and 1.8 kA. For $I_{DED} \geq 1.2$ kA an increase of the plasma density was observed, as shown in Fig. 7.1 a). After 3.5 s the helium injection was performed, in order to mitigate the influence of runaway electrons on plasma facing materials.

As diagnostics, neutron detectors and the scanning probe were used.

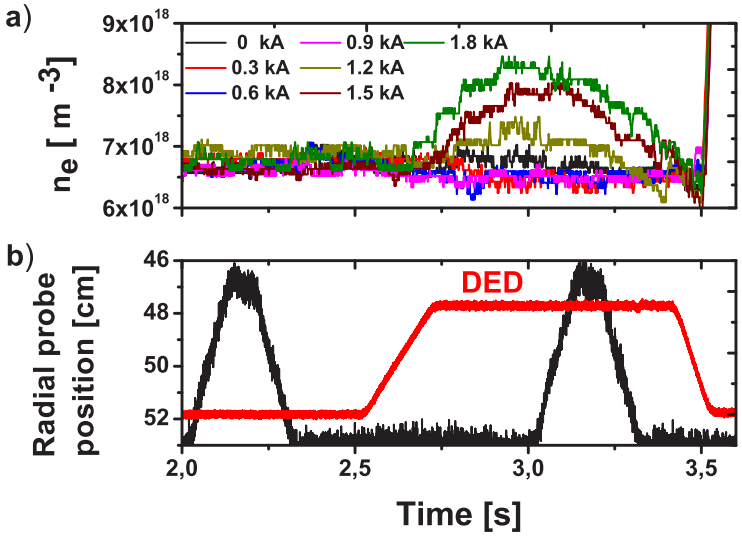

Figure 7.1: *a) Plasma densities before and during DED. b) The probe is inserted before and during DED to the plasma edge. The limiter position is at $r = 46$ cm. The time trace od the DED current is also shown.*

The neutron diagnostic can detect electrons with energies more than 10 MeV, which leave the plasma. In order to provide spectrally resolved measurements of runaways with energies between 4 and 30 MeV the new absolutely calibrated probe, see Sec. 3.2.2 was used. The probe was inserted to the plasma edge before the DED is switched on and during the DED phase. In Fig. 7.1 b) the probe position together with the DED current are shown in time. The limiter position is at $r = a$ ($a = 46$ cm).

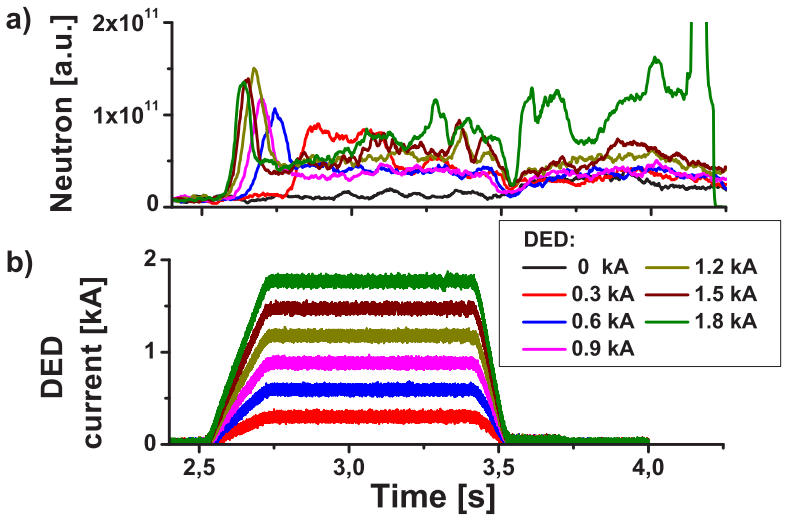

Figure 7.2: *a) Photo-neutrons generated by the runaways hitting the walls. b) The time traces of the DED current are shown for a few discharges.*

7.3 Measurements

7.3.1 Neutron measurements

Results of neutron measurements and corresponding DED currents are shown in Fig. 7.2. As soon as the DED current is switched on a complicated behavior of the neutron signal can be seen. The signal can be divided into three parts: the first one, at the moment when the DED current reaches some minimum value (about 0.3 kA) a strong mode (the 2/1 tearing mode) appears, which leads to the rapid loss of runaways. The mode amplitude saturates non-linearly to a level which is independent of the DED-current. The threshold of the mode is about $I_{DED} = 0.3$ kA, with an increase of I_{DED} the onset of the mode occurs earlier. At $I_{DED} \geq 1.2$ kA, a 3/1 tearing mode near the plasma edge is also excited. This mode causes an enhanced interaction with the wall, which explains the release of gas and the density increase mentioned above.

After the first rapid loss, despite that the I_{DED} remains constant, the runaways transport reaches a steady state, which remains constant till the end of the DED phase. The stationary phase can be explained by the balance between production and loss of runaways. In the last part, after the DED, a termination of the discharge occurs and as a result all runaway electrons which were in the

plasma, lose the confinement and can be detected by neutron detectors. As it follows from Fig. 7.2, in the presence of the DED the neutron signal is almost the same order of magnitude and may be even higher (for $I_{DED} = 1.8$ kA) as in the reference discharge without any applied external fluctuations. Similar results were observed in [37] in Fig.4. In these measurements different processes, like an increasing plasma density during the DED, a non reproducible density trend during the He-gas injection and a possible influence of the DED current strength on the magnetic field structure, can affect both the runaway production and their radial transport at the end of the discharge. Therefore, it is difficult to draw a conclusion as from the neutron measurements between 3.5 and 4 s in Fig. 7.2 follows an independence of the produced number of runaways on the presence of the DED.

7.3.2 Probe measurements

In the previous papers [36, 37, 103], it was shown that runaway electrons depending on their energy experience differently the DED. In Fig. 7.3 signals from all crystals of the probe are shown before and during the DED. At 2 s all channels demonstrate a good reproducibility. In the case of the crystal 7 the observed difference is ascribed to some artificial effects during the measurements. During the DED phase, a clear difference in the signals for the first seven crystals is observed for the discharges with the DED and without. Nevertheless, for the last 2 crystals, this difference disappears. It is important to mention that with the increasing number of the crystals, electrons with higher energies make the main contribution to the signal. For the DED current of 0.3 kA the probe was inserted in the time interval when some tearing modes just appear and cause an increase of the radial transport. Therefore, for $I_{DED} = 0.3$ kA signals from all crystals are slightly higher in comparison to other DED currents.

In order to make an energy resolved analysis of the electron transport during the DED, probe signals are analyzed using the method described in Sec. 3.2.1. The method provides information about the number of electrons with different energies hitting to the probe. In this analysis three different energy ranges: 4-8 MeV; 8-16 MeV and 16-30 MeV are considered. Since these ranges have a different energy width, the number of electrons is normalized

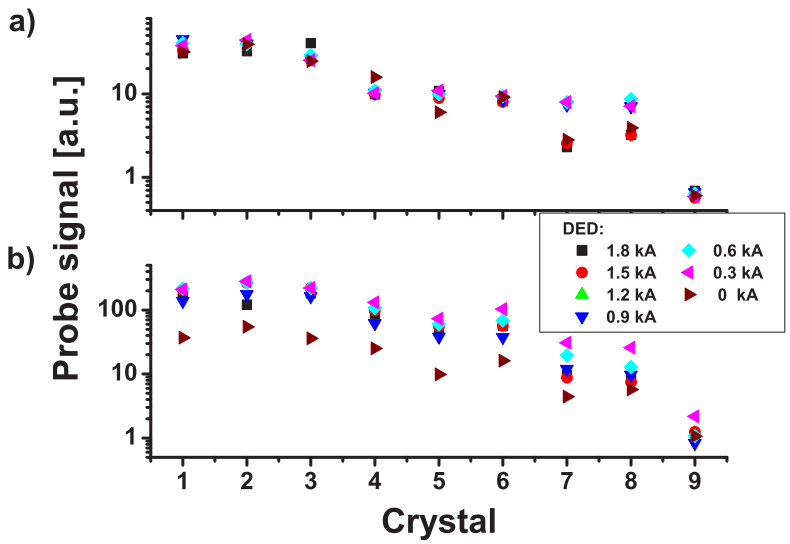

Figure 7.3: *Probe measurements before and during the DED. Signals from all nine crystals are shown. With increase of the crystal number electrons with higher energies are mainly detected. a) Signals correspond to an insertion time of 2 s (before the DED). b) Insertion time of the probe is 3 s (during the DED).*

per MeV range. Fig. 7.4 shows energy resolved electron numbers detected by the probe during 40 ms, before and during the DED. Similar as in Fig. 7.3, Fig. 7.4 a) demonstrates that the radial transport of electrons is the same for all considered discharges before the DED current is switched on. As soon as the external ergodic field is applied, the radial transport increases depending on electron energies. During the DED current, the probe was inserted during the stationary phase of neutron signals, as shown in Fig. 7.1 and 7.2, except of $I_{DED} = 0.3$ kA, where the probe signals were affected by the initial set of tearing modes. Therefore, the possible uncertainties in the measured trends between $I_{DED} = 0.3$ kA and other DED currents are ascribed to this effect.

Applying the method described in Sec. 3.2.2, spectra of runaway electrons are analyzed at $t = 2$ s and $t = 3$ s (with and without the DED). The spectrum of runaway electrons is described by a decreasing function, where a high energy part of the spectrum increases in time for the reference discharge and decreases for the DED ones, as shown in Fig. 7.5. The number of electrons detected by the probe is proportional to the electrons flux, approximated by the Fick's law $\Gamma = -D_r \nabla n$. As it follows from Sec. 5.2, the

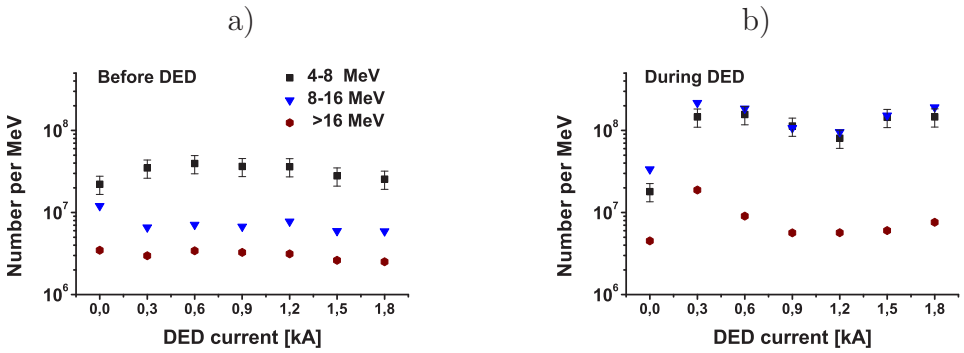

Figure 7.4: *Measurements of runaway electrons before and during the DED. Averaged number of electrons lost from the plasma per 1 MeV in three energy ranges (4-8 MeV; 8-16 MeV and 16-30 MeV) are shown at times: a) 2.14-2.18 s (before the DED is switched on); b) 3.14-3.18 s (during the DED).*

diffusion coefficient is constant at $t = 2$ s and $t = 3$ s. Therefore, an increase of $\nabla n(E > 20MeV)/\nabla n(E \simeq 4MeV)$ is expected. As soon as, the DED is applied, the distribution function reduces stronger at high energies, independently of I_{DED}.

7.4 Discussion

The spectral measurements in Fig. 7.5 show that during the DED phase, the relative number of high energy runaway electrons leaving the plasma is smaller than compared to the spectrum before the DED. The analysis of the number of electrons in the different energy ranges, in Fig. 7.4 b), demonstrates an increase of the loss of electrons with energies less than 16 MeV during the DED, while the transport of electrons with higher energies changes slightly. As a result, the relative number of high energy electrons decreases in the electron spectrum during the DED. The number of runaways at the high energy end of the spectrum is a balance between the continuous loss and the acceleration from lower energy runaways. Since the lower energy part is diminished by the DED, the higher energy part decreases as well, but with some time delay as was also shown by the synchrotron measurements in [36].

The probe measurements demonstrate that electrons with energies larger than 16 MeV are almost not affected by the DED. The influnce of the stochastic field on runaway electrons with different energies has also been discussed

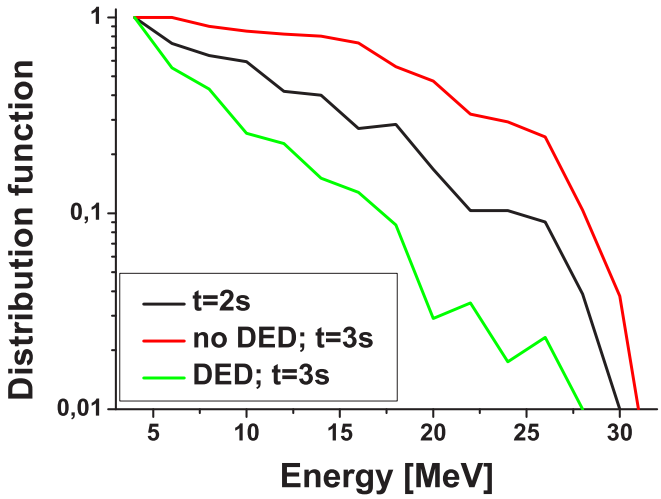

Figure 7.5: *Spectra of runaway electrons at $t = 2$ s and $t = 3$ s. At $t = 3$ s the spectrum evolution is shown for the reference discharge (without DED) and during the DED. The spectrum does not vary with I_{DED}.*

in [16, 37, 62, 74, 75, 103]. For the quantitative analysis of the dynamics of runaway electrons the Hamiltonian guiding centre equations for relativistic particles by generalizing the method proposed in [2] have been derived. These Hamiltonian equations of runaway electrons are integrated using the mapping approach [1]. Depending on the runaway energy, the orbits of the runaway electrons can be substantially different from the path of the magnetic field lines. The mapping procedure has been applied for the constructing Poincaré plots of the runaway dynamics [37, 103]. However, in the analysis, the perturbation field is taken as a vacuum field, i.e. no shielding currents of the plasma are taken into account. In the case of the low relativistic electrons, the deviation of Poincaré plots for the magnetic field and relativistic electrons is small, when the energy grows it starts to deviate strongly. Poincaré plots for electrons with energies of 1.3 MeV, 10 MeV and 30 MeV under the influence of the DED field are shown in Fig. 7.6 (published in [37]). The abscissa is the poloidal angle and the ordinate is the minor radius. The angle $\theta/2\pi = 0$ and 1 ($\theta/2\pi = 0.5$) corresponds to the low field side (high field side) of the torus. As seen from Fig. 7.6, the degree of ergodization decreases strongly with the runaway energy. The structure created by runaway electrons with energies of

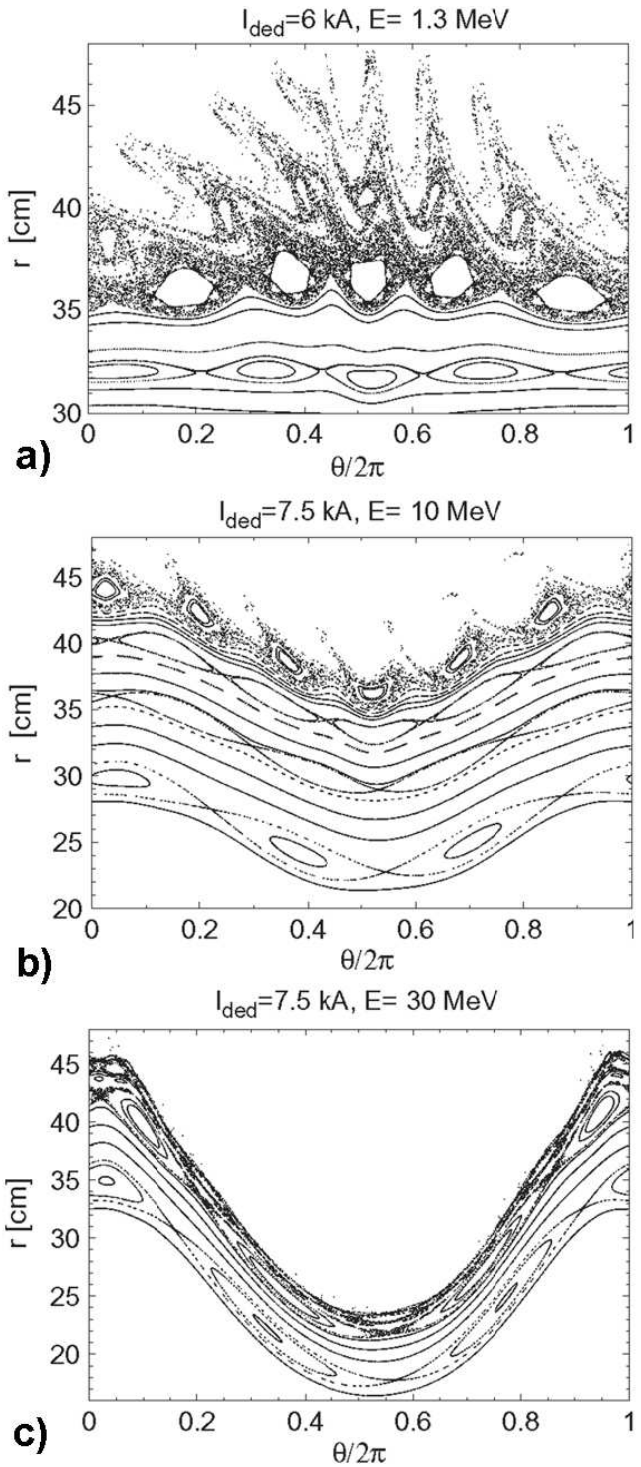

Figure 7.6: *Poincaré plots for the orbits of a) 1 MeV, b) 10 MeV and c) 30 MeV relativistic electrons, which are published also in [37]. With increasing energy, the orbits are strongly shifted to the low field side and the ergodization of the magnetic field lines has less influence on the orbits. The Poincaré plot of the magnetic field lines is identical to the low energy case of the electrons and corresponds practically to a); the last intact flux surface is at about 30 cm.*

1 MeV are very similar to the structure of the field lines. The finger structures [3] presented for 1 MeV electrons, in Fig. 7.6 a) vanishes at the kinetic energy of 10 MeV. Orbits of runaways with the energy of 30 MeV are regular or belong to islands, as shown in Fig. 7.6 c). The decrease of the chaotic behavior of runaways with increasing of their energy occurs: a) due to the drift effects, the structures of runaways are shifted outside, so that with increasing energy the distance to the DED coils grows, accompanied by a reduction of the perturbation level; b) due to the displacement of the orbits from the magnetic structure, the particle orbits average more and more over the island structure and reduce their effects [37].

From the analysis of Poincaré plots in Fig. 7.6 follows that with increasing runaway energies their loss from the plasma due to the DED should reduce. In the model by Myra and Catto [80, 81] ($D_r = \Upsilon \pi q R c (\delta B/B)^2$, where Υ is a drift modification factor) it was found that due to the orbit shift the influence of the magnetic perturbation on the diffusion coefficient can be substantially reduced. Since runaway electrons with higher energies possess a stronger orbit shift, it is expected that they can be less sensitive to magnetic perturbation.

In [103] the reduction of the runaway number in the plasma depending on their energy was analyzed during the DED phase. In the model the loss of runaway electrons from the plasma occurs mainly to the egodization of the magnetic field lines. If N_0 is the number of test particles on an unperturbed drift surface, uniformly distributed along the poloidal angle. N(t) is the number of particles left in the plasma at the time t after the DED is switched on. According to [103] N(t) is approximated as $N(t) = N_0(N_1 + exp(-\lambda t))$, where λ is the decay parameter, $N(t)/N_0$ is called the escape rate and N_1 is the offset of about $5 - 10\%$ for all escape rates. In [103], it was found that λ depends on the electron energy as $\lambda \sim -(E - E_c)$, where the critical energy $E_c \approx 20$ MeV with the DED operation in the 3/1 mode. Thus, electrons with energies higher than 20 MeV are not affected by the DED and confined in the plasma. The relative number of electrons left the plasma with energies between 4 MeV and 8 MeV equals $\frac{(N)_{loss}(4MeV)}{(N)_{loss}(8MeV)} \simeq \frac{1-e^{-\lambda_4 t}}{1-e^{-\lambda_8 t}} \sim \frac{\lambda_4}{\lambda_8} \approx 1.5$ in [103], where it is assumed that before the DED the number of electrons with energies between 4 MeV and 8 MeV is the same. A slight difference between $(N)_{loss}(4MeV)$ and $(N)_{loss}(8MeV)$, which is coming from the theory in [103] and the same number of electrons with energies between 4 MeV and 8 MeV detected by the probe

can be ascribed to the more complex electron distribution in the plasma, as it is predicted in the theory and to the observational accuracy. Nevertheless, the main conclusion that electrons with energies higher than 20 MeV are almost not affected by the DED is also confirmed from the probe measurements shown in Fig. 7.4 b).

Chapter 8

Plasma disruptions

8.1 Introduction

Disruptions are defined as the sudden loss of the plasma confinement including the plasma current [6, 54, 100]. In general one can observe three phases during the disruption: The pre-disruption phase (lasting up to several hundred milliseconds), the energy quench with a duration of a fraction of milliseconds and the current quench lasting some tens of milliseconds [87]. During the pre-disruptive phase one often observed growing MHD phenomena indicating that some limit of the plasma stability is reached. At the time of the energy quench, the plasma temperature drops instantaneously to a level of a few eV only. During the current quench the magnetic energy of the plasma current is dissipated leading to a temperature of the plasma of 5 eV to 10 eV typically. The reason for the disruption is most likely the loss of electrical current at the critical radii.

The first type of disruptions is connected with a current loss in the plasma core, i.e. at $q \leq 1$). This disruption occurs when high Z-material is accumulated in the core; it is mostly connected with a loss of sawtooth.

The second type of disruptions results most likely from a loss of current near the $q = 2$ surface. This is the "normal" disruption. There are several phenomena which provoke the loss of current at $q = 2$ and the disruption is named after these phenomena.

- There is the q-limit disruption, when I_p is ramped up or B_t is ramped down such that the $q = 2$ surface hits a limiting wall material such as a

limiter.

- There is edge cooling by gas fueling at insufficient heating of the plasma (density limit disruption [102]). One instability occurring under these conditions are so called MARFE [54, 73], where a cool and dense plasma "condensates" at the high field side of the torus or near the divertor X-point.

- Strong plasma shifts (e.g. Vertical Displacement events) lead to an intersection of the $q = 2$ surface with the wall resulting in a disruption [11, 54].

- Low Z-impurities can also reduce the temperature at the plasma edge leading to a disruption.

- Finally MHD-phenomena can suppress the current at $q = 2$ or $q = 3/2$ which then induces also the disruption [54, 96].

Massive gas injection by a "disruption mitigation valve, DMV", is a method which is recently investigated to stop a plasma discharge on purpose when a disruption seems unavoidable [14, 31, 38, 92]. By the DMV one can try to mitigate some effects which are highly undesirable during the tokamak operation. Similar as the high density limit it leads to a quick cooling of the $q = 2$ surface. When the limit of stability is reached, MHD-instabilities are practically always observed [101]. Therefore, disruptions are accompanied by MHD activities even if no explicit pre-cursor is observed.

The sudden loss of the plasma energy and of the plasma current have a strong impact on plasma facing components and on the vessel:

- In the energy quench (or thermal) quench the plasma energy is instantaneously deposited to those parts of the device which are hit during the disruption. Since one cannot control in many cases the plasma position in this phase, it may be that the energy is not deposited to the divertor or limiter which is normally laid out to handle high heat fluxes but to other-weaker-components. Since the energy loss is sudden, the plasma column at first expands and then shrinks, leading to the first lowering and then an enhancement of the plasma inductivity. The lowering results in a negative voltage spike, typically observed during the energy

quench [54]. The high level of MHD-activities seems consistent with a full ergodization of the plasma column.

- The energy stored in the magnetic field by the plasma current is normally higher than the thermal energy. This energy, however, cannot be released as suddenly as the thermal one, because of the substantial inductivity of the discharge. The dissipation time last from 10 ms to 100 ms, depending on detailed conditions.

- There are several indications that the plasma current is redistributed such that the ergodization is reduced and intact magnetic surfaces are re-established. This allows the acceleration of electrons by the high voltage of the decaying plasma; the runaway electrons reach energies up to 30 MeV and for ITER even energies up to 50 MeV are predicted [87]. The high energy allows the electrons to penetrate e.g. carbon facing materials and to provoke damage deep inside the material. Depending on conditions, up to 50% of the plasma current can be transformed into the runaway current [43, 85].

- Another problem in the decaying plasma are Halo-currents [87, 97]; these are electrical currents which partially flow along magnetic field lines but also partially in the vessel if those field lines intersect the walls. Up to 50% of the plasma current can be converted to Halo currents. Since the electrical current in the vessel component can flow obliquely to the magnetic field, strong forces act on the vessel.

- Finally a substantial electric current can be directly connected into structural elements, in particular if the loop voltage is very high due to a fast current termination.

In present, the main efforts are made to study properties of the runaway beam (production mechanisms, a distribution function, a thermal load in wall materials, a radial transport etc.) [23, 39, 66, 85, 90, 94] and possible mechanisms of mitigation of their production [31, 55, 106]. In this chapter, properties of the electron beam are studied during the plasma disruptions caused by the noble gas injection, as Ar, Kr, Xe. Such parameters, like an energy distribution of runaway electrons coming from the plasma, their thermal load in the

material, an absolute number and temporal evolution during thermal and current quenches are measured by the new probe, described in Sec. 3.2.2. During the present campaign, the number of discharges made with different gases is not enough to draw any conclusion about the mitigation efficiency of different gases. More detailed information about mitigation characteristics of different gases can be found in [15].

8.2 Experimental set-up

The experiments were performed in the TEXTOR tokamak with the following plasma parameters: plasma current, $I_p = 300$ kA, toroidal magnetic field, $B_t = 2.4$ T, the averaged electron density (1 s$\leq t \leq$2 s) $n_e = 2 \cdot 10^{19}\ m^{-3}$. The major radius of the TEXTOR tokamak is $R = 1.75$ m and the minor radius is $a = 46\ cm$ defined by the carbon limiter.

In order to initiate the disruption with runaway electrons, massive gas injection of noble gases was applied. The massive gas injection is carried out by a special "disruption mitigation valve" (DMV) [14, 38, 92]. About 10^{22} Argon atoms can be injected into the plasma by the DMV used in these experiments. The working gas pressure is about $1 - 20$ bar.

Measurements of runaway electrons were implemented by the scanning probe and a set of neutron detectors. Neutron detectors, which can detect runaways with energies higher than 10 MeV (defined by the photo-nuclear reaction (γ, n) threshold), have different sensitivities. Depending on the electron flux coming from the plasma the most sensitive ones were saturated. In this campaign, signals only from one neutron detector was used to check the self consistency of runaway measurements by different diagnostics.

The absolutely calibrated probe is used to study runaway electrons at the plasma edge. During these experiments, the probe was inserted at 47 cm minor radial position (in the equatorial plane from the low field side), as shown in Fig. 3.1, at 0.8 s before the disruption and it was kept at this position during 200 ms after the thermal quench. Thus, the probe provides direct measurements of runaways, which just left the plasma. Parameters, as the absolute number of runaways coming to the probe, their energy distribution can be provided by the probe. Additionally, energy load in the tungsten materials

was also measured by two thermocouples installed inside the probe, as shown in Fig. 3.7.

8.3 Runaways during the thermal and current quenches

In the previous chapters runaway electrons were produced during the stationary low density plasma discharges. Nevertheless, with the increasing densities the number of runaways reduces substantially. However it was still a question whether runaway electrons, produced during the stationary part of the discharge influence on the further production of runaways during the current quench.

Fig. 8.1 displays characteristic signals during the disruption. Subfigure 8.1 a) presents the magnetic activity (measured by Mirnov coils), the time traces of the electron temperature (ECE-signal) [102] and the first spike of the runaway probe of the first crystal with a better time resolution than that of subfigure 8.1 b). There from top to bottom are the time traces of the neutron signal, of the loop voltage, of the plasma current and of the probe crystals 1 and 9. At $t = 2$ s, argon gas was injected into the plasma by the DMV operating at 1 bar. After a few milliseconds the disruption starts with the increase of the loop voltage, a strong MHD-spike, the first runaway spike, a sudden drop of the electron temperature and the start of the current quench. This phase is the thermal quench. The first runaway spike is attributed to the runaways born in the high loop voltage phase at the start of the discharge which are lost when the plasma becomes ergodic.

Higher runaway signals are observed during the current decay phase starting 20 ms after the injection of Ar. In disruptions with runaway generation one observes typically a plateau in the current. This is the time when a substantial fraction of the current is carried by the runaway current. It is interesting to note that during the current quench runaway electrons are coming from the plasma as a set of bursts. Unfortunately, there is no information how these bursts are related to the possible magnetic fluctuations in the plasma, because Mirnov coils which are usually used to study the poloidal magnetic turbulence did not work as soon as the first strong modes appear due to the gas injection.

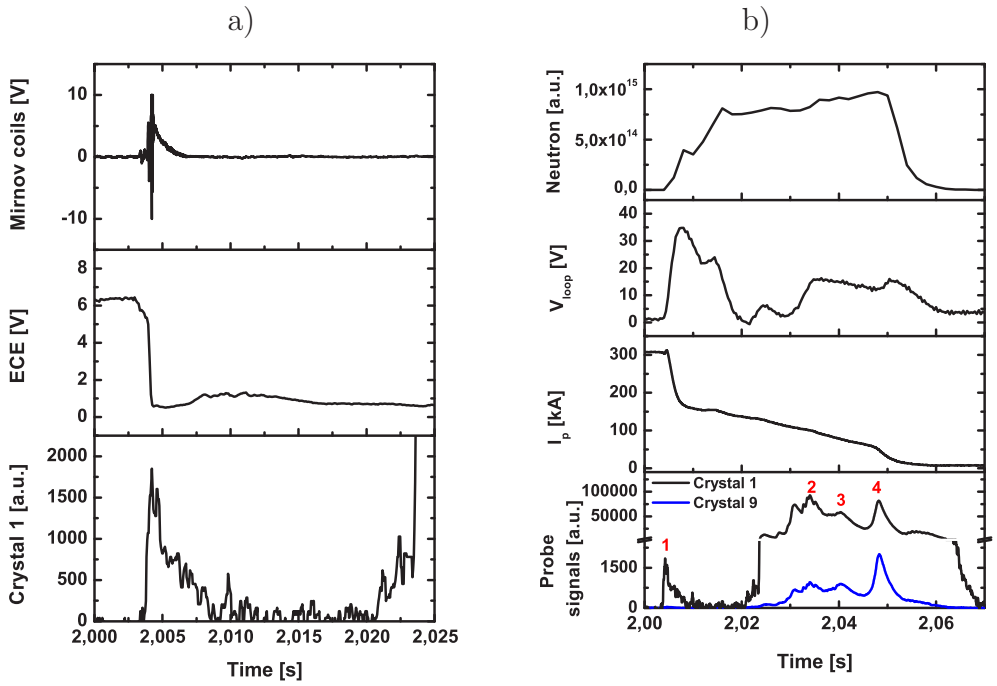

Figure 8.1: *The disruption is provoked by the Ar gas injection with a working pressure 1 bar at 2 s. As a result strong MHD-instabilities appear. a) Above signal from the Mirnov coils demonstrates the time when the strong modes show up. In the middle, information about the electron temperature can be obtained from the ECE signal. The cooling of the plasma starts at about $t = 2.003$ s. Bottom signal from the first crystal of the probe, shows a lost of runaways due to presence of the MHD activities. b) From the top to the bottom of the figure neutron signal, loop voltage, plasma current and probe signals from crystal 1 and crystal 9 during the current and thermal quenches. During the current quench electron are coming from the plasma as a set of bursts (e.g. peaks 2, 3 and 4).*

With increasing number of the crystal in the probe, electrons with higher energies produce mainly the signal. The comparison of signals from the first and the ninth crystals at $t = 2.034$ s (peak 2) and $t = 2.048$ s (peak 4) points out that with time during the current quench the population of the high energy electrons increases in the runaway flux coming to the probe.

In order to analyze spectra of runaways produced during the time of current and thermal quenches the method described in Sec. 3.2.2 is applied. The analysis of the runaway spectrum during the current quench is performed for different kind of gasses (Ar, Xe, Kr). In Fig. 8.2 disruptions provoked by gases Ar (1 bar), Xe (2 bar) and Kr (2 bar) are shown. The plasma current and the

signal of crystal 1 of the probe as functions of time are displayed in Fig. 8.2 a). Fig. 8.2 b) shows the spectra of Ar (top), Kr and Xe (bottom) at different times. It can be seen that the shortening of the current decay time causes a reduction of the electron number detected by the probe. Although, in the present measurements the current decay time depends directly on the atomic number of the noble gas, in the present thesis this effect is beyond of the scope of the analysis.

For the Ar gas the time developing of the runaway spectrum is shown.

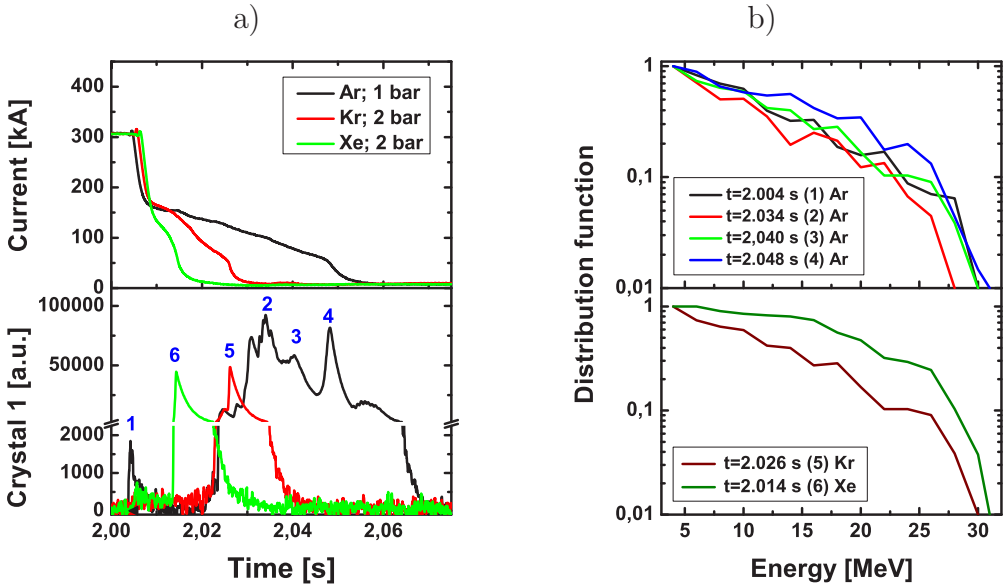

Figure 8.2: *Analysis of runaway spectra is performed for disruptions provoked by the noble gas injection. Three different gases are used Ar (1 bar), Xe (2 bar) and Kr (2 bar). a) Above the plasma currents for disruptions provoked by the three different gases are shown. Bottom, corresponding signals from the first crystal of the probe are presented. b) Runaway spectra are analyzed for 5 electron bursts during the current quench. The first peak is produced due the loss of runaways during the time of thermal quench. These electrons are mainly produced in the plasma before the gas injection occurs.*

The coming runaway beam to the probe has a decreasing distribution function up to the cut-off energy (in logarithmic scale). The spectrum of the first runaway spike at the onset of the thermal quench shows the cut-off energy of about 27 MeV.

During the current quench, after the Ar gas injection, spectra of runaway electrons are analyzed for a few electron bursts (peak 2, 3 and 4). The high

energy part of the spectrum and the cut-off energy grows in time during the current quench. In case of Kr and Xe gases, the spectrum of runaway electrons does not change much and is almost the same as it is for the Ar gas at time $t \geq 2.040$ s.

The high energy part of the runaway spectrum grows for the electron bursts later in time. This growth is observed for all disruptions discharges, with a few electron bursts during the current quench.

In [90], 1D numerical simulations were performed in order to analyze the spectrum of runaway electrons produced due the avalanche process, which play the main role during the current quench. The spectrum was simulated for electrons which are confined in the plasma. It was shown that runaways have an exponential distribution. In the present measurements of runaway electrons at the plasma edge, the distribution function has a weaker dependence on the electron energy than the exponential one. The difference between the prediction and experimental results can be explained by a few reasons: i) In the 1D simulation [90], radial transport of runaway electrons is not included. Additionally such loss mechanism like synchrotron radiation or cyclotron instabilities affect the maximum energy of runaways and their confinement time. In [50] it was shown that the presence of the diffusive loss can cause a substantial reduction of the production rate of the avalanching process. ii) With increasing energy of runaway electrons their orbit shift increases proportionally [74, 75]. At the same time the growth of the runaway energies leads to an increase of their confinement time. Both these effects are important for the radial transport of runaways and also on the spectrum of the detected electrons by the probe at the plasma edge.

8.4 Internal modes

During these experiments there were a few discharges, where magnetic instabilities appear in the plasma prior to the disruption. The enhanced MHD causes a sudden loss of runaway electrons and later the plasma disruption. In Fig. 8.3 two discharge with strong internal modes are shown. In the first one, Fig. 8.3 a), electrons are lost from the plasma about 0.35 s before the disruptions. As soon as the disruption occurs, no further electrons are detected

during the thermal quench. It is important to note that the disruption occurs in Fig. 8.3 due to the strong MHD-activities and the gas injection is not used. Therefore, it is possible to conclude that due the strong modes (probably tearing modes), which appears during this discharge, runaways are fully depopulated in the plasma at $t = 1.51$ s before the disruption occurs.

Another discharge with internal modes, in Fig. 8.3 b), demonstrates the loss of runaway electrons at $t = 1.612$ s. However, in this case electrons are not lost completely from the plasma. Due to the further development of MHD-instabilities which is started at $t = 1.666$ s, relatively slow cooling of the plasma (in comparison to Fig. 8.2) and a subsequent reduction of the plasma current occurs. At the starting phase of the plasma cooling, strong magnetic fluctuations lead to the loss of the rest part of runaway electrons.

Analysis of both cases shows that internal fluctuations appeared in the plasma lead finally to the full depopulation of the runaway electrons in the plasma. Therefore, it is expected that during major disruptions in Fig. 8.1 and Fig. 8.2, runaway electrons produced before the gas injection completely leave the plasma during the time of the current quench.

A spectrum of runaway electrons detected by the probe at $t = 1.666$ s (also at $t = 1.612$ s) is shown in Fig. 8.4). These electrons have a decreasing distribution function up to the cut-off energy of about 27 MeV (in logarithmic scale). In the presence of strong MHD-instabilities, all runaway electrons are leaving the plasma. Since independently on the energy of runaways, they were detected by the probe simultaneously, it is expected that runaway electrons in the plasma have the same distribution function as it was measured by the probe in Fig. 8.4) at the plasma edge.

8.5 Thermal load of runaways

A negative aspect why runaway electrons are so undesirable especially in the big tokamaks is their thermal load deposition deep in the plasma facing materials and in the cooling limiter (ITER tokamak). In recent studies it was shown that about 50% of plasma current can be converted into the runaway current [85]. In the ORMAK tokamak, the tungsten rod limiter was melted

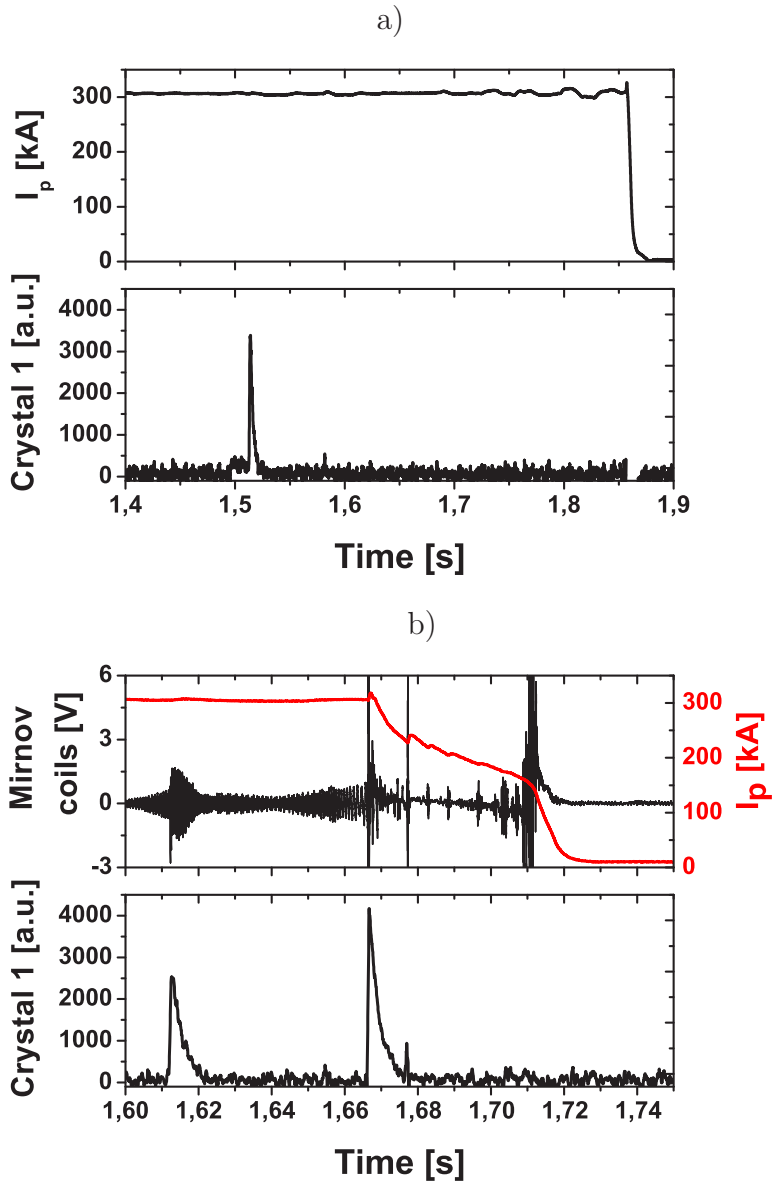

Figure 8.3: *Loss of runaway electrons in presence of strong MHD-instabilities. a) Runaway electrons leave the plasma at* $t = 1.51$ *s this is before the disruption occurs. (Top - plasma current, bottom - signal from the first crystal.). b) The first modes appearing in the plasma at* $t = 1.612$ *s do not lead to the full depopulation of runaway electrons. At* $t = 1.666$ *s, a repeated set of MHD-activities occurs which lead to the cooling of the plasma and finally to the rapid current quench at* $t = 1.710$ *s. At the final phase of these activities the rest part of runaways leaving the plasma. (Top- plasma current and signal from Mirnov coils, bottom - signal from the first crystal.)*

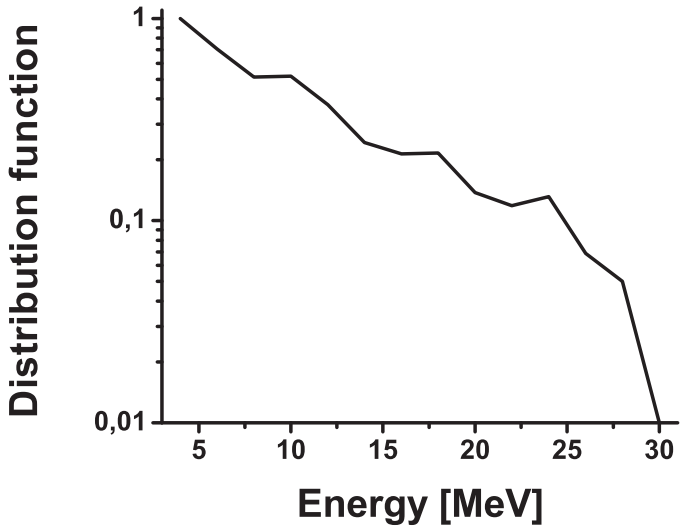

Figure 8.4: *Spectrum of runaway electrons detected by the probe at* $t = 1.666$ *s (also at* $t = 1.612$ *s) in Fig. 8.3 b).*

after having been exposed to about ten discharges with runaway electrons [63].

The present probe is equipped by two thermocouples, which allow to measure a temperature from the tungsten top filter in front and back sides of the probe, as shown in Fig. 3.7. The temporal resolution of the thermocouples is 0.3 s.

Typical measurements of the temperature of the tungsten filter from the front and back side of the probe are shown in Fig. 8.5. The disruption provoked by the Ar gas injection (1 bar) is accompanied by the production of runaway electrons during the current quench. The number of runaways left from the plasma during the thermal quench is about two orders of magnitude less than during the current quench.

Temperature measurements show that for the thermocouple of the front side the temperature grows as soon as electrons pass through the probe. The second one demonstrates an increase of the temperature with some time delay. This delay is defined by the time which is necessary that the thermal front can reach the back side of the tungsten. In the discharge (Xe, 2-bar) with relatively low number of runaways an increase of the temperature was not observed, as shown in Fig. 8.6. Additionally, temperature trends from the both thermocou-

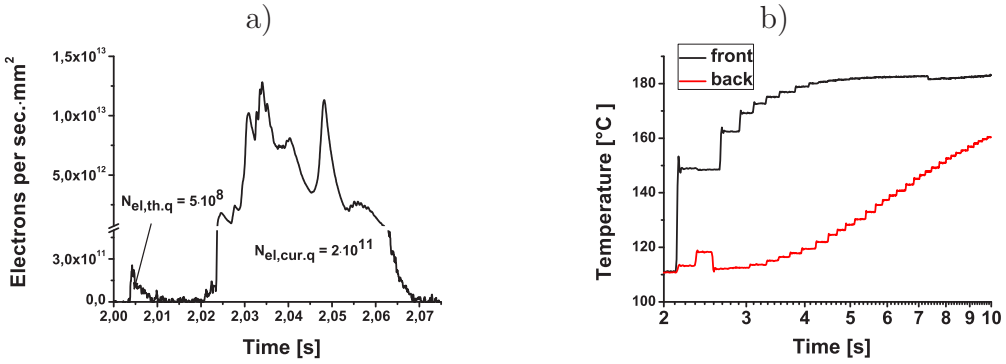

Figure 8.5: *Temperature measurements are performed for disruptions provoked by the Ar gas injection (1 bar). a) Normalized electron numbers per second and mm^2 are shown during the thermal and current quench time interval. Electrons with energies higher than 4 MeV are measured by the first crystal. b) The temperature is measured in front and the back side of the probe from the tungsten filter.*

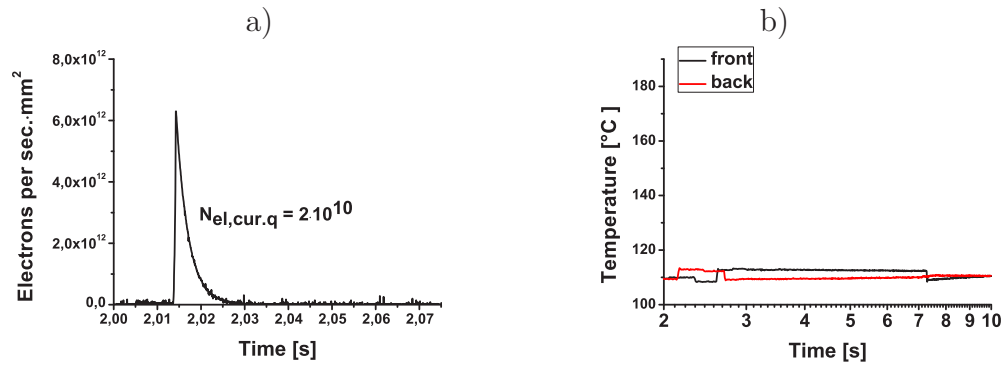

Figure 8.6: *Temperature measurements are performed for disruptions provoked by the Xe gas injection (2 bar). a) Normalized electron numbers per second and mm^2 are shown during the thermal and current quench time interval. Electrons with energies higher than 4 MeV are measured by the first crystal. b) The temperature is measured in front and the back side of the probe from the tungsten filter. In contrast to Fig. 8.5 b) almost no increase of the temperature is observed for both thermocouples.*

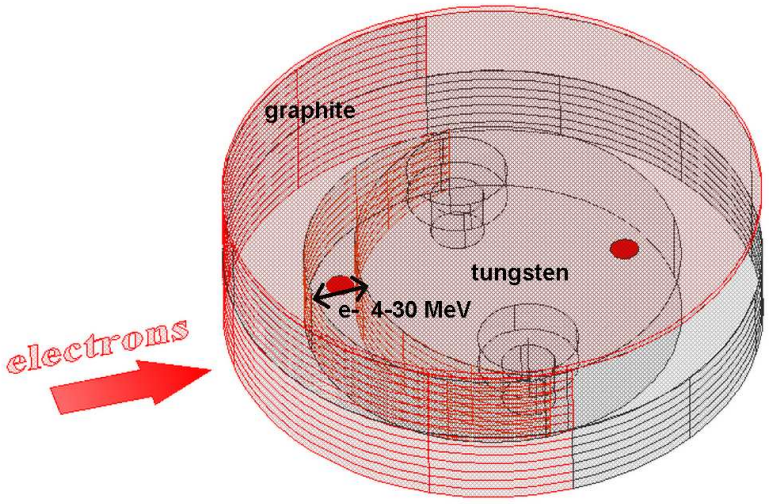

Figure 8.7: *Thermal load of runaway electrons in the probe. Electrons with energies $W_r \leq 3$ MeV stop in the graphite. Runaway electrons with energy $W_r \geq 4$ MeV pass through the graphite mantel and they are absorbed in the tungsten. High relativistic electrons $W_r \approx 30$ MeV can penetrate deep into the tungsten up to 4 mm (Geant4 simulation [42] and SLAC(EGS: Basic Simulation Tool) [93]). Absorption areas of runaway electrons in graphite and tungsten are shown in red. Two red spots (circle) show the position of the thermocouples.*

ples, in Fig. 8.5 b), demonstrate that the increase of the temperature occurs mainly due to the hot electrons.

The total number of electrons detected by the probe is about $2{\cdot}10^{11}$ $[\frac{electrons}{mm^2}]$. From the spectrum measurements in Fig. 8.3 b) this electrons have an average energy (E_{av}) of about 15 MeV. Estimations performed by means of the Geant4 code [42] show that electrons with energies of about 30 MeV can penetrate about 4 mm tungsten. The front cross section of the tungsten is $S_W = 168\ mm^2$. Hence, the total number of electrons with energies between 4 and 30 MeV incident on the tungsten is $N_W = 3.4 \cdot 10^{13}$. These electrons lose their kinetic energy in 4 mm of tungsten, as shown in Fig. 8.7. If radiation losses of runaway electrons in the material are neglected, the thermal load of these electrons in the tungsten equals their total kinetic energy $Q_{kin} = N_W \cdot E_{av} \approx 80$ J. The front part of the tungsten, where almost all runaways lose their energy has a mass of $m_{fr,W} \approx 17$ g. Consequently, the temperature increase of the front part of tungsten equals $\triangle T = Q_{kin}/m_{fr,W} \cdot c_W \approx 35°$C, where c_W is the heat capacity of tungsten.

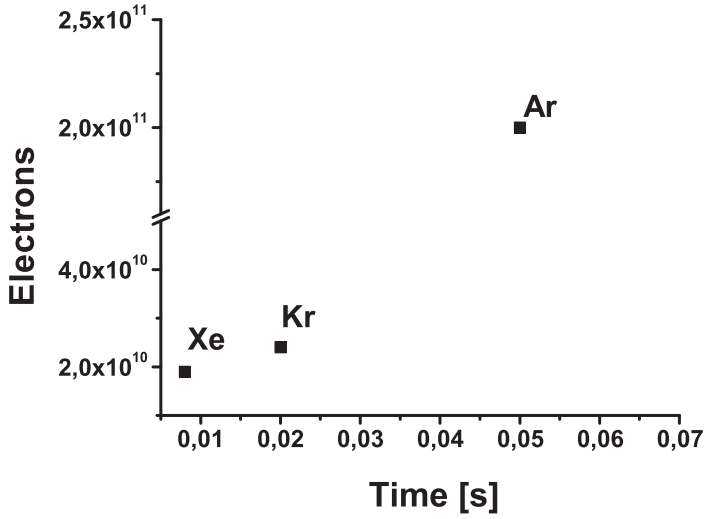

Figure 8.8: *Electron numbers detected by the probe during the current quench for the disruption discharges, which are shown in Fig. 8.2 a)*

This value fits the measured one of about 37°C.

Runaway electrons with energies between 4 and 30 MeV can pass through the graphite mantel (5 mm) and heat the tungsten. However, this energy is enough to heat only the front layer of the tungsten (about 4 mm) and cannot explain the further increase of the temperature of the full tungsten filters with mass of $m_W \approx 70$ g on 50°C after 10 s. In this case the required energy is about $Q_{th} = m_W c_W \cdot 50 \approx 472$ J. This energy can come from the graphite mantel, Fig. 8.7, which can get energy not only from the high energetic runaway electrons, but also from electrons with energies 10 eV$\ll T_e \leq$3 MeV. Thermal electrons are neglected, because in the discharges with the lower number of runaways, in Fig. 8.6, almost no temperature increase occurred.

The active graphite cross section is about $S_C \approx 450\ mm^2$. The energy load from the runaways with energies higher than 4 MeV is $Q_{h.rel} \approx 100$ J. Therefore, the rest required energy $Q_{l,rel} \approx 400$ J has to come from electrons with energies 10 eV$\ll T_e \leq$3 MeV. Assuming that these electrons have an average energy $< E > \approx 0.2$ MeV, their total number can be estimated, as $N_{l,rel} = Q_{l,rel}/e < E > \approx 10^{16}$. It corresponds to about $5 \cdot 10^{14}$ $[\frac{electrons}{s \cdot mm^2}]$, which is about 100 times more than the value for electrons with energies higher than 4 MeV (about of $4 \cdot 10^{12}$ $[\frac{electrons}{s \cdot mm^2}]$).

Up to the 50% of the plasma current can be replaced by the runaway current. In ITER the planned plasma current is about 15-20 MA. The typical value of current quench time is predicted to be about 100-200 ms in ITER [87]. The number of runaways detected by the probe has to increase with the runaway current. Additionally, the runaway number increases with the current decay time, which is also shown in Fig. 8.8. Therefore, the estimation of the minimum number of runaway electrons (with energies between 4 and 30 MeV) per mm^2 coming to the plasma phasing materials during the current quench in ITER is about $2 \cdot 10^{13}$ $[\frac{electrons}{mm^2}]$, which corresponds to the thermal load of $q \approx 50$ J/mm^2. In tungsten these electrons are absorbed in the layer of 4 mm and cause an increase of the temperature on about 5000°C. It is enough to melt the tungsten facing material. Thus, runaway electrons present a serious problem for ITER and a development of a proper mitigation mechanism is an extremely important issue.

Chapter 9

Summary and Outlook

A new probe has been developed to measure high energy runaway electrons (in the MeV range) in tokamaks. The probe is mounted on a quickly movable holder which allows three radial insertions into the plasma during a discharge. The basic element of the probe are YSO crystals which transform the energy of runaway electrons into visible light which is guided via optical fibres to photomultipliers.

In order to obtain the energy distribution of the runaways, the crystals are covered with layers of stainless steel (or tungsten in the two earlier test versions) of different thicknesses. These layers absorb runaways up to some minimum energy which depends on the layer thickness; in this way they serve as energy filters. The final probe design has 9 crystals which can provide energy resolution of electrons with energies between 4 and 30 MeV. In order to protect the probe from thermal electrons and from ambient light, it is covered by a graphite shield of 5 mm in thickness. Additionally, the third generation of the probe is equipped with two thermocouples, which allow measurements of the thermal load from runaway electrons in tungsten. The probe can measure runaways with the high temporal resolution at the plasma edge during low density plasma discharges as well as during disruptions.

The probe is tested and absolutely calibrated at the linear accelerator ELBE in Rossendorf. The measurements are in good agreement with the Monte Carlo simulations by the Geant4 code.

The probe was used at the TEXTOR tokamak which can produce runaways and is equipped with specific runaway diagnostics. The probe provides the

spectrum of runaway electrons for the first time.

The thesis discusses the runaway transport in the presence of internally and externally applied magnetic perturbations. It was found that an increase of runaway losses from the plasma with the decreasing toroidal magnetic field is accompanied with a growth of the magnetic fluctuation in the plasma. The diffusion coefficient for runaways was derived as a function of B_t and a quantitative value of the magnetic fluctuations has not yet been derived otherwise. The magnetic shielding picture could be confirmed which predicts that the runaway loss occurs predominantly for low energy runaways (few MeV only) and considerably less for the high energy ones.

In case of the externally applied magnetic perturbations by means of the dynamic ergodic divertor (DED) runaway electrons with different energies demonstrate a different sensitivity to the DED. Again, highly relativistic electrons are less sensitive to the stochastic magnetic field than the low energy ones. The enhanced loss of low energetic runaways leads to a depopulation of high relativistic ones.

Measurements of runaway electrons during the plasma disruptions were carried out by the new probe. Important parameters, such as the runaway flux, the energy distribution, the temporal evolution and the thermal load in materials were studied. Additionally, some predictions about the possible damages for the ITER tokamak were made. The probe shows two distinct losses of runaways during the thermal quench (runaways are produced at the start up of the discharge) and during the current quench (runaway are produced during the current quench phase). During the disruption experimental campaign a few discharges with a strong MHD- activities occurred, which cause a sudden loss of runaways from the plasma. These electrons were mainly produced at the start up of the discharge.

As an outlook, the present work is going to be carried on in the following directions:

- Study of anomalous transport by means of the present and the new 2D probes, which will provide information about the diffusion coefficient and the magnetic perturbation at the plasma edge. In the combination with synchrotron radiation measurements the radial profile of these parameters are going to be obtained.

- Study of the behavior of runaways in the presence of the internal or exter-

nally applied magnetic fluctuations. This property of runaway electrons can be used as one of the mitigation mechanism of the runaway electron production during the plasma disruption.

- Detailed study of the possible damage of ITER like materials due to the runaway electrons is going to be performed by a new probe with several layers.

Appendix A

Geant4 code

The analysis of the electron spectrum measured by the probe bases on the 3D Monte Carlo Geant4 code simulations [4, 42]. The code is the successor of the Geant series of software toolkits developed by CERN, and the first to use Object oriented programming (in C++). Geant4 is a toolkit for the simulation of the passage of particles through matter. Its application areas include high energy, nuclear and accelerator physics, as well as studies in medical and space science. In the code a broad variety of the detector simulation can be done: geometry, tracking, detector response, run, event and track management, visualization and user interface.
The abundant set of physical processes can be included in the simulations:

- Particle Decay
- Electromagnetic Interactions
  - Particle Transport
  - Gamma Incident
  - Charged Particles
  - Electron and Positron Incident
  - Charged Hadron Incident
  - Muon Incident
  - Electron/Positron/Gamma Incident
  - Low Energy Extensions

  - Optical Photons
  - Shower Parameterizations

- Hadronic Interactions

Geant4 is widely used in areas of physics such as:

* High energy physics (ATLAS, CMS LHCb at LHC. CERN etc.)

* Space and Radiation (European Space Agency, QinetiQ, GLAST)

* Medical (Geant4: Application for Tomographic Emission, European Medical User Organization, Medical Physics in Japan, North American Medical User Organization)

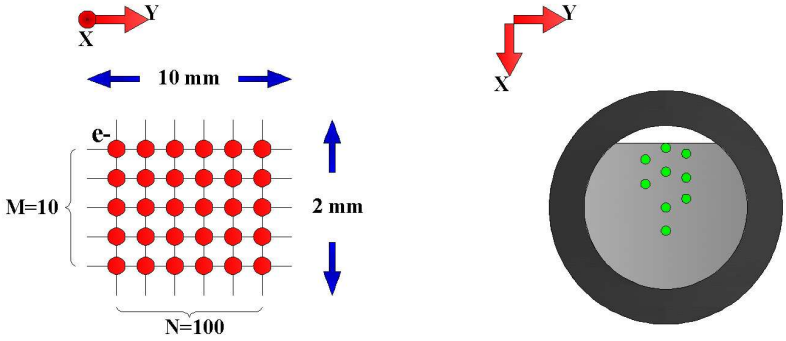

Figure A.1: *Electron sources in the simulations. The grid contains 1000 of electron sources, each of them produces 1000 of electrons. The size of the grid is* 10×10 *mm, the division of the grid is* $N \times M = 100 \times 10$*. In addition, the energy distribution of electrons can be defined.*

In the present work the absorption energy of electrons in the crystal has been simulated by Geant4 code. The design of the third probe is shown in Fig. 3.7. The probe has 5 mm graphite mantel and depending on the crystal number the following thickness of stainless steel is used from the incidence direction of electrons: crystal 1 - 0 mm; 2 - 1 mm; 3 - 2 mm; 4 - 2.5 mm; 5 - 3.5 mm; 6 - 4.6 mm; 7 - 5.5 mm; 8 - 7 mm and 9 - 9.5 mm.

In the present simulation the electron bunch was uniformly distributed in front of the probe with a grid of particles as shown in Fig. A.1. The grid size is 10×2 mm with the total number of electrons sources (red points) 100×10.

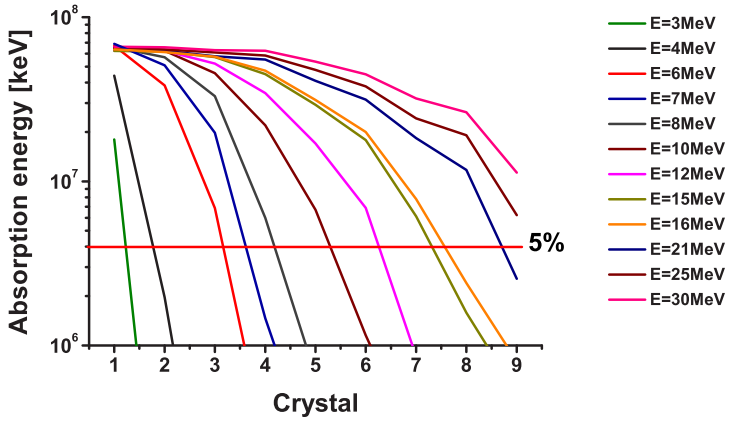

Figure A.2: *Absorption energies in the crystals of the probe. The mono-energetic electron beams are simulated, with a number of particles of* 10^6*. The minimum energy of the electron, which can be detected by the crystal is defined as the cut-off of the absorbed energy of* 5% *of the maximum one.*

Each source produces 1000 of electrons. Additionally, the energy distribution of electrons can be defined. The grid is placed just in front of the probe.

Fig. A.2 shows the absorbed energy in each crystal for mono-energetic electron beams. The correctness of the simulation was tested separately in Sec. 3.2.2.

Depending on the electron energy the absorbed energy reduces with the number of crystals. It is assumed the crystals cannot detect electrons, where the absorbed energy is less than 5% of the maximum value. This method posses an error bar in the energy definition of the order of about 20% and can be applied up to energies of electrons of about 16 MeV, due to an increase of radiation losses for the higher energy electrons, as shown in Fig. 3.8 b). Thus, e.g. crystal 1 can detect electrons with energies higher than about 3-4 MeV, crystal 5 - 8 MeV and crystal 8 - 16 MeV.

Appendix B

Analysis of the diffusion coeffcient

An analysis of the diffusion coefficient from the synchrotron radiation was described in [20, 22]. In the present appendix the main points of this method are presented.

The diffusive processes are described by the diffusion equation

$$\frac{\partial n}{\partial t} = -\nabla \cdot \Gamma + S, \tag{B.1}$$

where n is the particle density, $\Gamma = -D\nabla n$ is the particle flux (Fick's law) and S is a source density. The analysis of the diffusion coefficient is performed during the steady state, i.e. $\frac{\partial n}{\partial t} = 0$ and the diffusion coefficient is approximated, as

$$D(r) = \left(\frac{1}{r} \int_0^r r' dr' S(r') \right) / \left(-\frac{\partial n}{\partial r}(r) \right). \tag{B.2}$$

Under the assumption of a mono-energetic distribution of runaways

$$\frac{\partial n}{\partial r} \sim I_0 \frac{\partial i(r)}{\partial r}, \tag{B.3}$$

where the measured intensity (proportional to the emitted synchrotron power) $I = I_0 i(r)$, I_0 is the profile maximum and $i(r)$ defines the profile shape.

In [20, 22] the total source was given by

$$\int_0^a S(r)dV_r \sim \dot{\tilde{I}}(a)|_{t=t_0}/\tilde{I}(a)|_{t\to\infty}, \tag{B.4}$$

where V_r is the volume within a surface of radius r, a is the minor radius, ∞ denotes steady state, $\tilde{I}(a)$ is the intensity time trace and $\dot{\tilde{I}}(a)|_{t=t_0}$ is a derivative of $\tilde{I}(a)$ at the start time of the rising signal.

Three different assumption on the source profile are proposed in [20, 22] leading to the upper, lower and intermediate level of the diffusion coefficient.

The upper limit is approximated by the source profile, which is given by a δ function

$$S_{up}(r) = \frac{s\delta(r)}{r},\ \epsilon < r < a, \tag{B.5}$$

where $\epsilon > 0$ is small. The diffusion level equals

$$D_{r,up} = -\frac{k\left(\frac{\dot{\tilde{I}}(a)_{|t=t_0}}{\tilde{I}(a)_{|t\to\infty}}\right)}{r\left(\frac{\partial i(r)}{\partial r}\right)}, \tag{B.6}$$

where k is a constant depending on the chosen parametrization of the measured intensity profile $i(r)$, for a triangle profile k equals $a^2/6$.

In the lower limit case the source profile is constant

$$S_{low}(r) = \frac{2s}{a^2},\ r < a, \tag{B.7}$$

and the diffusion level

$$D_{r,low}(r) = \left(\frac{r}{a}\right)^2 D_{r,up}(r). \tag{B.8}$$

Assuming that the runaway distribution has a given width at the critical energy, and that this profile broadens during the acceleration due to diffusion with a constant D_r a more precise solution is found for the source profile. With a Gaussian birth rate distribution and in a view of that the creation zone of

runaways is approximately $d_r = 7$ cm [58], the source profile is

$$S_{it}(r) = sCexp\left(-\left(\frac{r}{\sigma_1}\right)^2\right), \tag{B.9}$$

where C is a normalization constant and $\sigma_1 = [d_r^2/\ln 2]^{1/2}$. The diffusion coefficients is defined by

$$D_{r,n}(r) = \frac{[1 - exp(-(r/\sigma_n)^2)]}{[1 - exp(-(a/\sigma_n)^2)]} D_{r,up}(r), \tag{B.10}$$

where σ_n is the width calculated from $D_{r,n-1}$ after $\triangle t$. In [20, 22], the iteration converges at a width of $\sigma \approx 23$ cm.

Bibliography

[1] S.S. Abdullaev, K.H. Finken and K.H. Spatschek, Phys. Plasmas **6**, 153 (1999)

[2] S.S. Abdullaev and K.H. Finken, Phys. Plasmas **9**, 4193 (2002)

[3] S.S. Abdullaev, A. Wingen and K.H. Spatschek, Phys. Plasmas **13**, 042509 (2006)

[4] J. Allison, K. Amako, J. Apostolakis, H. Araujo, et.al., Nucl. Science **53**, 270 (2006)

[5] F. Anderson, P. Helander and L.-G. Eriksson, Phys. Plasmas **8**, 5221 (2001)

[6] L.A. Artsimovich, Nucl. Fusion **12**, 215 (1972)

[7] M. Balcerzyk, M. Moszynski, M. Kapusta, D. Wolski, J. Pawelke, C.L. Melcher, IEEE Trans. Act. Nucl. Sci. **47**, 1319 (2000)

[8] M. Bakhtiari, Y. Kawano, H. Tamai, Y. Miura, R. Yoshino, and Y. Nishida, Nucl. Fusion **42**, 1197 (2002)

[9] M. Bakhtiari, G.J. Kramer, M. Tekechi, H. Tamai, Y. Miura, Y. Kusama, and Y. Yamada, Phys. Rev. Lett. **94**, 215003 (2005)

[10] M. Bakhtiari, G.J. Kramer, and D.G. Whyte, Phys. Plasmas **12**, 102503 (2005)

[11] P. Barabaschi, "Heat loads on baffles during a downward VDE", ITER Report #*S* 73 MD 7797-03-21 W01 1997

[12] N.T. Besedin and I.M. Pankratov, Nucl. Fusion **26**, 807 (1986)

[13] R.J. Bickerton, Plasma Phys. Control. Fusion **39**, 339 (1997)

[14] S.A. Bozhenkov, K.H. Finken, M. Lehnen, and R.C. Wolf, Rev. Scient. Instrum. **78** 033503 (2007)

[15] S.A. Bozhenkov, M. Lehnen, K.H. Finken, M.W. Jakubowski, et.al., Plasma Phys. Control. Fusion **50**, 105007 (2008)

[16] P.J. Catto, J.R. Myra and A.J. Wootton, Phys. Plasmas **1**, 684 (1994)

[17] H. Dreicer, Phys. Rev. **115**, 238 (1959)

[18] I. Entrop, R. Jaspers, N. J. Lopes Cardozo and K. H. Finken, Plasma Phys. Control. Fusion **41**, 377 (1999)

[19] A.G. Elfimov and R.M.O. Galvao, Plasma Phys. Control. Fusion **45**, L63 (2003)

[20] I. Entrop, Ph.D Thesis, Eindhoven University of Technology, The Netherlands (1999)

[21] I. Entrop, N. J. Lopes Cardozo, R. Jaspers, and K. H. Finken, Phys. Rev. Lett. **84**, 3606 (2000)

[22] I. Entrop, R. Jaspers, N. J. Lopes Cardozo and K. H. Finken, Plasma Phys. Control. Fusion **41**, 377 (1999)

[23] L.-G. Eriksson, P. Helander, F. Andersson, D. Anderson and M. Lisak, Phys. Rev. Lett. **92**, 205004 (2004)

[24] ESTAR: Stopping Power and Range Tables for Electrons, National Institute of Standards and Technology (NIST), http://physics.nist.gov/PhysRefData/Star/Text/ESTAR.html.

[25] B. Esposito, R.M. Solis, P. vanBelle, O.N. Jarvis, F.B. Marcus, G. Sadler, R. Sanchez, B. Fischer, P. Froissard, J.M. Adams, E. Cecil, N. Watkins, Plas. Phys. Contr. Fusion **38**, 2035 (1996).

[26] B. Esposito, J.R. Martin-Solis, R.M. Poli, J.A. Mier, R. Sanchez, L. Panaccione, Phys. Plasmas **10**, 2350 (2003)

[27] J. Faure, Y. Glinec, A. Pukhov, S. Kiselev, S. Gordienko, E. Lefebvre, J.-P. Rousseau, F. Burgy and V. Malka, Nature **431**, 541 (2004)

[28] I. Fernández-Goméz, J.R. Martín-Solís, R. Sánchez, Phys. Plasmas **14**, 072503 (2007)

[29] K.H. Finken, J.G. Watkins, D. Rusbuldt, W.J. Corbett, K.H. Dippel, D.M. Goebel, R.A. Moyer, Nucl. Fusion **30**, 859 (1990)

[30] K.H. Finken and G.H. Wolf, Fusion Eng. Des. **37**, 337 (1997)

[31] K.H. Finken, G. Mank, A. Krämer-Flecken, R. Jaspers, Nucl. Fusion **41**, 1651 (2001)

[32] K.H. Finken, A. Kraemer-Flecken, M. Lehnen, A. Savtchkov, J. Nucl. Mater. **313-316**, 1247 (2003)

[33] K.H. Finken, S.S. Abdullaev, W. Biel, M.F.M. de Bock, Plasma Phys. Control. Fusion **46**, B143 (2004)

[34] K.H. Finken, R. Jaspers, A. Krämer-Flecken, A. Savtchkov, M. Lehnen, G. Waidmann, Fusion Science and Engineering. **47**, 266 (2005)

[35] K.H. Finken, S.S. Abdullaev, M. Jakubowski, R. Jaspers, M. Lehnen, O. Zimmermann, Nucl. Fusion **46**, S139 (2006)

[36] K.H. Finken, B. Unterberg, Y. Xu, S.S. Abdullaev, M. Jakubowski, et.al., Nucl. Fusion **47**, 91 (2007)

[37] K.H. Finken, B. Unterberg, Y. Xu, S.S. Abdullaev, M. Jakubowski, et.al., Nucl. Fusion **47**, 522 (2007)

[38] K.H. Finken, M. Lehnen, S.A. Bozhenkov, Nucl. Fusion **48**, 115001 (2008)

[39] T. Fülöp, G. Pokol, P. Helander and M. Lisak, Phys. Plas. **13**, 062506 (2006)

[40] G. Fussmann, Nucl. Fusion **19**, 327 (1979)

[41] A.A. Galeev and R.Z. Sagdeev, Transport phenomena in rarefied plasma in toroidal magnetic traps ZhETF **53** 338-359 (in Russian)

[42] Geant4 software developed by Members of the Geant4 Collaboration ($http://cern.ch/geant4$).

[43] R.D. Gill, Nucl. Fusion **33**, 1613 (1993)

[44] R.D. Gill, B. Alper, M. de Baar, T.C. Hender, M.F. Johnson, V. Riccardo and contributors to the EFDA-JET Workprogramme, Nucl. Fusion **42**, 1039 (2002)

[45] R.H. Cohen, Phys. Fluids **19**, 239 (1976)

[46] J.W. Connor and R.J. Hastie, Nucl. Fusion **15**, 415 (1975)

[47] A.V. Gurevich, Sov. Phys. JETP **12**, 904 (1961)

[48] A.V. Gurevich, G.A. Milikh and R. Roussel-Dupre R, Phys. Lett. A **165**, 463 (1992)

[49] A.V. Gurevich and R. N. Sudan, Phys. Rev. Lett. **72**, 645 (1994)

[50] P. Helander, L.-G. Eriksson, F. Andersson, Phys. Plasmas **7**, 4106 (2000)

[51] P. Helander, L.-G. Eriksson, and F. Andersson, Plasma Phys. Control. Fusion **44**, B247 (2002)

[52] E.M. Hollmann, T.C. Jernigan, M. Groth, D.G. Whyte, D.S. Gray, M.E. Austin, B.D. Bray, D.P. Brennan, N.H. Brooks, T.E. Evans, D.A. Humphreys, C.J. Lasnier, R.A. Moyer, A.G. MacLean, P.B. Parks, V. Rozhansky, D.L. Rudakov, E.J. Strait and W.P. West, Nucl. Fusion **45**, 1046 (2005)

[53] B. Hidding, K.-U. Amthor, B. Liesfeld, H. Schwoerer, S. Karsch, M. Geissler, L. Veisz, K. Schmid, J. G. Gallacher, S. P. Jamison, D. Jaroszynski, G. Pretzler, and R. Sauerbrey, Phys. Rev. Lett. **96**, 105004 (2006)

[54] 1999 ITER physics basis, Nucl. Fusion **39**, 2137 (1999)

[55] S.C. Jardin, G.L. Schmidt, E.D. Fredrickson, et.al., Nucl. Fusion **40**, 923 (2000)

[56] O.N. Jarvis, G. Sadler, J.L. Thompson, Controlled Fusion and Plasma Heating (Proc. 15th Eur.Conf. Dubrovnik, 1988), Vol. 12B, Part I, European Physical Society 334 (1988)

[57] R. Jaspers, K.H. Finken, G. Mank, F. Hoenen, J.A. Boedo, N.J.L. Cardozo and F.C. Schuller, Nucl. Fusion **33**, 1775 (1993)

[58] R. Jaspers, Ph.D Thesis, Eindhoven University of Technology, The Netherlands (1995)

[59] R. Jaspers, N. J. Lopes Cardozo, A. J. H. Donné, H. L. M. Widdershoven and K. H. Finken, Rev. Scient. Instrum. **72**, 466 (2001)

[60] R. Jayakumar, H. H. Fleischmann, and S. J. Zweben, Phys. Lett. A **172**, 447 (1993)

[61] B.B. Kadomtsev, *Tokamak plasma: A complex physical system, IOP Publishing Ltd, 1992*

[62] H. Kawashima, K. Nagashima, H. Tamai, Y. Miura, et.al., Plasma Fusion Res. **70***, 868 (1994)*

[63] H. Knoepfel and D.A. Spong, Nucl. Fusion **19***, 785 (1979)*

[64] M.D. Kruskal and I.B. Bernstein, PPPL Report MATT-Q-20, p174 (1962)

[65] T. Kudyakov, K.H. Finken, M. Jakubowski, M. Lehnen, Y. Xu, O. Willi, Rev. Scient. Instrum. **79** *10F126 (2008)*

[66] T. Kudyakov, K.H. Finken, M.W. Jakubowski, M. Lehnen, Y. Xu, B. Schweer, T. Toncian, G. Van Wassenhove, O. Willi and the TEXTOR team, Nucl. Fusion **48***, 122002 (2008)*

[67] R.M. Kulsrud, Y.G. Sun, N.K. Winsor, H.A. Fallon, Phys. Rev. Lett. **31***, 690 (1973)*

[68] B. Kurzan, K. -H. Steuer, and G. Fussmann, Phys. Rev. Lett. **75***, 4626 (1995)*

[69] O.J. Kwon, P.H. Diamond, F. Wagner, G. Fussmann, ASDEX and NI teams, Nucl. Fusion **28***, 1931 (1988)*

[70] L. Laurent and J.M. Rax, Europhys. Lett. **11**, *219 (1990)*

[71] M. Lehnen, S. Bozhenkov, M.W. Jakubowski, R. Jaspers, V.V. Plyusnin, V. Riccardo, JET EFDA Contributors and the TEXTOR team, in Proceeding of the 18th Inter. Conf. on Plasma Surf. Inter. in Contr. Fus. Dev. (PSI), Toledo, Spain, (2008)

[72] M. Lehnen, S.A. Bozhenkov, S.S. Abdullaev and M. W. Jakubowski, Phys. Rev. Lett. **100** *255003 (2008)*

[73] B. Lipschultz, B. Labombard, E.S. Marmar, M.M. Pickrell, et.al., Nucl. Fusion **24** *977 (1984)*

[74] Machiel de Rover, Niek J. Lopes Cardozo and Attila Montvai. Cato, Phys. Fluids **3**, *4468 (1996)*

[75] Machiel de Rover, Niek J. Lopes Cardozo and Attila Montvai. Cato, Phys. Fluids **3**, *4478 (1996)*

[76] J.R. Martín -Solís, J.D. Alvarez, R. Sánchez, Phys. Plasmas **5**, *2370 (1998)*

[77] J.R. Martín -Solís, B. Esposito, R. Sánchez, J.D. Alvarez, Phys. Plasmas **6**, *238 (1999)*

[78] H.E. Mynick and J.A. Krommes, Phys. Rev. Lett. **43**, *1506 (1979); Phys. Fluids 23, 1229 (1980)*

[79] H.E. Mynick and J.D. Strachan, Phys. Fluids **24**, *695 (1981)*

[80] J.R. Myra and P.J. Catto, Phys. Fluids B **4**, *176 (1992)*

[81] J.R. Myra, P.J. Catto, H.E. Mynick, and R.E. Duvall, Phys. Fluids B **5**, *1160 (1993)*

[82] I.M. Pankratov, R. Jaspers, K.H. Finken, I. Entrop, G. Mank, Nucl. Fusion **2**, *279 (1998)*

[83] V.V. Parail and O.P. Pogutse, Nucl. Fusion **18**, *303 (1978)*

[84] V.V. Parail and O.P. Pogutse, Rev. Plasma Phys. **11**, *1 (1986)*

[85] V.V. Plyusnin, V. Riccardo, R. Jaspers, B. Alper, et.al., Nucl. Fusion **46**, *277 (2006)*

[86] G. Pokol, T. Fülöp and M. Lisak, Plasma Phys. Control. Fusion **50**, *045003 (2008)*

[87] S. Putvinski, P. Barabaschi, N. Fujisawa, N. Putvinskaya, M. N. Rosenbluth and J. Wesley, Plasma Phys. Control. Fusion **39**, *B157 (1997)*

[88] A.B. Rechester and M.N. Rosenbluth, Phys. Rev. Lett. **40**, *38 (1978)*

[89] V Riccardo and JET EFDA contributors, Plasma Phys. Control. Fusion **45**, *A269 (2003)*

[90] M.N. Rosenbluth and S.V. Putvinski, Nucl. Fusion **37**, *1355 (1997)*

[91] A.J. Russo, Nucl. Fusion **31**, *117 (1991)*

[92] A. Savtchkov, K.H. Finken, G. Mank, Rev. Scient. Instrum. **73** *3490 (2002)*

[93] SLAC National Accelerator Laboratory, Menlo Park, CA. (EGS: Basic Simulation Tool):
http : //www2.slac.stanford.edu/vvc/egs/basicsimtool.html

[94] H. Smith, P. Helander, L.-G. Eriksson, D. Anderson, M. Lisak and F. Andersson, Phys. Plas. **13**, *102502 (2006)*

[95] Yu.A. Sokolov, JETP Lett. **29**, *218 (1979)*

[96] E.J. Strait, T.A. Casper, M.S. Chu, J.R. Ferron, et.al., Phys. Plasmas **4**, *1783 (1997)*

[97] E.J. Strait, L.L. Lao, J.L. Luxon and E.E. Reis, Nucl. Fusion **31**, *527 (1991)*

[98] TEXTOR tokamak:
http : //www.fz − juelich.de/ief/ief − 4//textor_en/

[99] E.P. Velikhov and S.V Putvinski, Fusion energy. Status and purpose in the lon-term outlook. Report, Energy Center of the World Federation of Scientists, 1999

[100] J. Wesson, Tokamaks, Clarendon Press - Oxford, 1997

[101] J.A. Wesson, R.D. Gill, M. Hugon, F.C. Schúller, J.A. Snipes et.al., Nucl. Fusion **29**, *641 (1989)*

[102] G. Waidmann, Y. Cao, B. Kardon, Plasma Phys. Control. Fusion **31**, *323 (1989)*

[103] A. Wingen, S.S. Abdullaev, K.H. Finken, M. Jakubowski and K.H. Spatschek, Nucl. Fusion **46**, *941 (2006)*

[104] D.G. Whyte, T.C. Jernigan, D.A. Humphreys, A.W. Hyatt, C.J. Lasnier, P.B. Parks, T.E. Evans, M.N. Rosenbluth, P.L. Taylor, A.G. Kellman, D.S. Gray, E.M. Hollmann, and S.K. Combs, Phys. Rev. Lett. **89**, *055001 (2002)*

[105] R. Yoshino, S. Tokuda and Y. Kawano, Nucl. Fusion **39**, *151 (1999)*

[106] R. Yoshino and S. Tokuda, Nucl. Fusion **40**, *1293 (2000)*

[107] YSO crystals produced by Proteus Inc., (http://www.proteus-pp.com).

Publications

Journals

1. T. Kudyakov, K.H. Finken, M.W. Jakubowski, M. Lehnen, Y. Xu, B. Schweer, T. Toncian, G. Van Wassenhove, O. Willi and the TEXTOR team *Spatially and temporally resolved measurements of runaway electrons in the TEXTOR tokamak.* Nucl. Fusion **48** 122002 (2008).

2. T. Kudyakov, K.H. Finken, M.W. Jakubowski, M. Lehnen, Y. Xu, O. Willi and the TEXTOR team *Spectral measurements of runaway electrons by a scanning probe in the TEXTOR tokamak.* Rev. Scient. Instrum. **79** 10F126 (2008).

3. T. Kudyakov, A. Jochmann, K. Zeil, S. Kraft, K.H. Finken, U. Schramm and O. Willi, *High energy electron crystal spectrometer.* Rev. Scient. Instrum. (2009).

Reports

1. FZ Jülich Scientific Report 2007, Association EURATOM - FZJ, *Nuclear Fusion - Diagnostics and Heating.* Forschungszentrum Juelich GmbH, Jülich, Germany (2007).

2. FZ Jülich Scientific Report 2007, Association EURATOM - FZJ, *Nuclear Fusion - Tokamak Physics.* Forschungszentrum Juelich GmbH, Jülich, Germany (2007).

Conferences

1. B. M. Hegelich, B. Albright, L. Yin, M. Schmitt, J. Fuchs, L. Romagnani, P. Antici, P. Audebert, T. Toncian, T. Kudyakov, O. Willi, C. Cecchetti, P. Wilson and M. Borghesi *Focusing and spectral control of laser-driven, picosecond ion beams.* 48th Annual Meeting of the Division of Plasma Physics, Philadelphia, Pennsylvania, USA (2006).

2. T. Kudyakov, K.H. Finken, M.W. Jakubowski, B. Schweer, T. Toncian, Y. Xu and O. Willi *Study of runaway electrons in the TEXTOR tokamak.* 385 Wilhelm and Else Heraeus Seminar , Bad Honnef , Germany (2007).

3. T. Kudyakov, K.H. Finken, M.W. Jakubowski, M. Lehnen, B. Schweer, T. Toncian, Y. Xu, G. Van Wassenhove, and O. Willi *Spatially and temporally resolved measurements of runaway electrons in the TEXTOR tokamak.* DPG tagungen 2008, Darmstadt, Germany (2008).

4. T. Kudyakov, K.H. Finken, M.W. Jakubowski, M. Lehnen, Y. Xu, O. Willi, and the TEXTOR team *Spectral measurements of runaway electrons by a scanning probe in the TEXTOR tokamak.* The 17^{th} HTPD conference, Albuquerque, New Mexico, USA (2008).

5. T. Kudyakov, K.H. Finken, M.W. Jakubowski, M. Lehnen, Y. Xu, S.A. Bozhenkov, O. Willi, G. van Wassenhove and the TEXTOR team *Measurements of runaway electrons in the TEXTOR tokamak.* The 35^{th} EPS conference, Crete, Greece (2008).

6. T. Kudyakov, K.H. Finken, O. Willi, M.W. Jakubowski, Y. Xu, S.A. Bozhenkov, M. Lehnen, and the TEXTOR team *Measurements of runaway electrons in the TEXTOR tokamak.* The 36^{th} EPS conference, Sofia, Bulgaria (2009).

Die hier vorgelegte Dissertation habe ich eigenständig und ohne unerlaubte Hilfe angefertigt. Die Dissertation wurde in der vorgelegten oder in ähnlicher Form noch bei keiner anderen Institution eingereicht. Ich habe bisher keine erfolglosen Promotionsversuche unternommen.

Düsseldorf, 03.06.2009

(Timur Kudyakov)